

On the Impingement of Droplets upon Moving Films



Antony James Mitchell
University of Nottingham,
University Park,
Nottingham
NG7 2RD
July 29, 2019

Abstract

Environmental and economic considerations are amongst the key challenges faced in the contemporary aviation industry. Increasing fuel, labour and parts prices, coupled with an ever-tightening legislative environment necessitate a programme of continuing improvement to engine design.

Aero-engines contain bearings housed within bearing chambers and oil is supplied to the bearing for lubrication and cooling purposes, creating a complex two phase environment. Windage and churning in bearing chambers are causes of parasitic losses to the engine, and the high temperatures are a major factor in oil degradation and the formation of carbon deposits. Both of these factors increase the financial and environmental burden to an airline operator. Therefore, it is desired to 'tune' the chamber to minimise these behaviours. A key element of bearing chamber design is the ability to understand and model droplet-film interactions.

A desirable method of modelling is the use Computational Fluid Dynamics (CFD), however these simulations are highly computationally expensive. Therefore, it is desirable to offer empirical correlations for some elements of the droplet-film interaction to reduce the computational costs.

In this thesis research is presented that leads to enhanced understanding and new correlations for droplet impingements on moving films. This represents a significant addition to knowledge as prior the vast majority of available data is for impingements on static films. The research outcomes were achieved by the use of high speed imaging and Laser Induced Fluorescence (LIF), including Brightness-Based Laser Induced Fluorescence (BB-LIF) applied across a range of droplet impingement conditions. Experimental data was then compared to correlations and understanding from static film studies.

This work focused on parameters to determine the impingement outcome, characteristics of secondary droplets were formed, and the morphology and development of the crown and cavity.

Secondary droplet production showed a good level of comparability to static film research, and four distinct mechanisms of droplet production were categorised. The crown and cavity dynamics after the impingement were compared to static film models, and modifications proposed to these models in order to better represent moving-film impingements.

In conclusion, it was found that static film knowledge could be applied to moving films, either directly or with modification to account for behaviours

unique to moving-film impingements. This is a useful addition to knowledge, and will help guide the development of the next generation of CFD modelling.

Acknowledgements

I would like to thank my supervisors, Dr. Kathy Simmons and Dr. David Hann for helping me develop my research skills across a variety of areas, and their unerring guidance and support.

I would also like to express gratitude towards Andrey Chedantsev, for sharing his expertise in the BB-LIF technique. And the staff of the Gas Turbine Transmissions Research Centre, and Rolls-Royce Plc, for their productive discussions.

Finally, I would like to acknowledge funding From the Engineering and Physical Sciences Research Council, and Rolls-Royce Plc, which allowed this project to take place.

Contents

1	Introduction	1
1.1	Rationale	1
1.2	Aims and Objectives	4
1.3	Structure of Thesis	4
2	Literature Review	7
2.1	Overview of Droplet Impingement	8
2.1.1	Impingement Outcomes	8
2.1.2	Dimensionless Parameters	13
2.2	Impingements on solid substrates and static films	16
2.2.1	Solid Substrates	16
2.2.2	Impingements upon Static films	20
2.3	Moving Substrates and Oblique Impingements	26
2.3.1	Oblique Impingement	27
2.3.2	Moving Substrates	28
2.3.3	Moving Films	30
2.4	Droplet Impingement Modelling	33
2.4.1	Secondary Droplets	33
2.4.2	Crown Morphology	37
2.4.3	Ligament Formation	40
2.4.4	Crater Development Modelling	42
2.4.5	Droplet Spreading and Mixing	47
2.5	Summary of Droplet Impingement Literature	49
2.6	Data Acquisition Methods	51
2.6.1	Visual Data Acquisition Methods	51
2.6.2	Laser Induced Florescence (LIF)	54
2.7	Droplet Generation Methods	58
2.8	Data Processing and Analysis	58
2.8.1	Image Post-processing and Enhancement	59
2.8.2	Spatial Calibration	60

2.8.3	Droplet Detection	60
3	Experimental Investigation	64
3.1	Experimental Apparatus	64
3.1.1	Test Rig Summary	64
3.1.2	Droplet Generation	66
3.1.3	Flow Calibration	66
3.1.4	Experimental Parameter Range	68
3.2	Channel Characterisation	68
3.2.1	Empirical data	69
3.3	Visual Data Acquisition	80
3.3.1	Camera Positioning	80
3.3.2	BB-LIF Dye Concentrations	81
3.3.3	High Speed Camera Set-up	82
3.4	Data Processing and Analysis	83
3.4.1	Preprocessing	83
3.4.2	Image Feature Detection	84
3.4.3	Secondary Droplet Production Mechanism	88
3.5	BB-LIF Image Processing	91
3.5.1	Conversion to Height Data	91
3.6	Conclusions on Data Analysis	96
4	Secondary Droplet Production	98
4.1	Impingement Outcomes	99
4.2	Mechanisms of Crown Splashing	107
4.3	Secondary Droplets	113
4.3.1	Number of Secondary Droplets	113
4.3.2	Secondary Droplet Properties	117
4.4	Concluding Remarks on Droplet production	120
5	Crown and Cavity Development	122
5.1	Comparison of BB-LIF and Side-View Data	123
5.2	Development of Cavity Shape	125
5.2.1	Cavity Dynamics	125
5.2.2	Cavity Development	128
5.2.3	Droplet Spreading	137
5.3	Crown Development	141
5.3.1	Crown Morphology	141
5.3.2	Crown Modelling	147
5.3.3	Conclusions of crown and cavity development	160



6 Conclusions	161
6.1 Summary of Main Findings	161
6.1.1 Secondary Droplet Production	162
6.1.2 Film Behaviour	165
6.2 Contributions to Knowledge	167
6.3 Future Work	168
References	170

List of Figures

1.1	Oil flow within a typical aero-engine from Klingsporn et al [1] . . .	2
1.2	Typical oil flow within a bearing chamber (cross section)	3
1.3	The combined Discrete Particle Modelling/Volume of fluid approach used to model droplet impingements [2]	4
2.1	Types of Solid-Substrate Impingement outcomes from Rioboo et al. [3]	9
2.2	Impingement outcomes observed by Worthington [4]	11
2.3	<i>Bubbling</i> observed by Worthington [4]	12
2.4	Prompt and Basket Splashing	13
2.5	Nondimensionalisation of droplet spreading for droplet impingements upon a solid surface from Stow and Hadfield [5]	17
2.6	A comparison of the approximation from Roisman et al. [6] and the numerical solution from Fukai et al. [7]	18
2.7	Graph showing the splashing parameter ($K_{Cossali}$) against the non dimensional film thickness from Cossali et al. [8]	20
2.8	A figure from Rioboo [9], showing boundaries between coalescence and crown formation (labelled as the <i>D-C Limit</i>), and crown formation/crown splash (labelled as the <i>C-S limit</i>).	21
2.9	A figure from Okawa [10], showing boundaries between Crown formation/Crown Splash for pure water, and water-glycerin mixtures	22
2.10	A figure from Okawa [10], showing occurrences of Sudden Ejection (SE) and no ejection (NE)	22
2.11	Comparison of Critical Weber We_c Number against Temperature from Wang et al. [11]	25
2.12	Examination of critical Weber Number for various fluids from Castillo et al. [12]	26
2.13	Graph from [13] Illustrating Transition region between coalescing and bouncing	28

2.14 Effect of angle upon impingement outcome from Leneweit et al. [14]	29
2.15 Impingement of droplet upon spinning wheel, from Mundo et al. [15]	29
2.16 Boundaries between spreading and splashing from Bird et al. [16]. Note the asymmetric splashing region	30
2.17 Images of droplet impingement upon horizontally moving film from Alghoul et al. [17]	31
2.18 Regime map observed by Castrejon et al. [18]	32
2.19 Correlation for number of secondary droplets from Okawa et al. [10]	34
2.20 Effect of angle against number of secondary droplets (normalised by predicted values, N_0 for a normal impingement) from Okawa et al. [19]	35
2.21 Corona properties against dimensionless time for droplets impinging on a solid surface, from Stow and Hadfield [5]	36
2.22 Secondary droplet diameters from Cossali et al. [20]	37
2.23 Comparison of theoretical model from Trujillio and Lee [21] against experimental data from Cossali et al. [8]	39
2.24 A figure from Krechetnikov & Homsy [22], illustrating different forms of crown.	40
2.25 Calculation of the inverse Bond number of the crown rim against time, from Zhang et al [23]	41
2.26 Comparison of the peak wavelength against predicted values from Rayleigh-Plateau (RP) instability and Rayleigh-Taylor (RT) instability from Zhang et al. [23]	42
2.27 A sketch of a crater establishing nomenclature of the cavity and crown	43
2.28 A figure from Bisighini et al. [24], comparing the model in Eqns. (2.19 - 2.20) to experimental data	44
2.29 Comparison of a VOF CFD model for impingements upon thin films with a CFD model from Berberovic et al. [25]	45
2.30 A figure from Hann et al. [26] comparing experimental data about droplet deformation from a droplet-film interaction to the model from Roisman et al. [6] (Eqn. (2.12))	47
2.31 Von Karman Vorticity predicted computationally at the droplet-film interface by Thoraval et al. [27]	48
2.32 Von Karman Vorticity observed at the droplet-film interface by Castrejon-Pita et al. [28]	48

2.33 Vorticity map from Agbaglah et al. [29], showing computational simulations, and experimental data from Zhang et al. [30], showing the transition to vorticity around $Ca = 0.2$	49
2.34 Illustration of a droplet impact made by Worthington [31] in 1876	51
2.35 Photograph of a droplet impact taken by Edgerton in 1936 [32] .	52
2.36 Still from the film obtained by Levin and Hobbs [33]	53
2.37 A long exposure image obtained by Yarin and Weiss [34] using a strobe light	53
2.38 Depth profile obtained using BB-LIF from Alekseenko et al. [35], numbered labels indicate features in the film referenced in the original literature.	55
2.39 Depth profile obtained using BB-LIF from Cherdantsev et al. [36]	56
2.40 Depth profile obtained using BB-LIF from Hann et al. [26]	57
2.41 Background removal process used by Vernon [37]	59
2.42 Lighting correction and background removal by Mathworks [38] .	60
2.43 Edge detection, thresholding and morphology used by Vernon . .	61
2.44 Circled detected using the <i>imfindcircles</i> function from MATLAB literature [39]	62
3.1 Diagram showing the Testing Rig	65
3.2 Photograph of the testing rig, showing the inclined channel, cameras and laser optics.	66
3.3 Photograph of the testing rig, showing the adjustment mechanism in detail	67
3.4 Schematic of the Channel elevation system	68
3.5 Photograph of the syringe height adjustment system	68
3.6 Photograph of the droplet generation system from preliminary testing.	69
3.7 Illustration of the confocal laser displacement technique from the original Minsky patent [40] (annotated)	70
3.8 Experimental apparatus for determination of film thickness	71
3.9 Photo of experimental apparatus for determination of film thickness	71
3.10 Surface profile taken from the Keyence LT-9030M confocal laser displacement sensor, showing a raw voltage signal, and the processed height readings, and the x-axis shows the measurement number.	72
3.11 Experimental measurements of film thickness for various flowrates and channel inclinations.	74

3.11 Experimental measurements of film thickness for various flowrates and channel inclinations. 75

3.12 Bulk film speeds, including error bars calculated using the 95 % confidence intervals shown in Tbls. (3.3 - 3.6). The legend indicates the channel inclination angle in degrees 76

3.13 Diagram of the Camera Positioning 80

3.14 Positioning of the cameras and laser optics 81

3.15 Diagram of the Camera Positioning 81

3.16 Spatial calibration 84

3.17 Histograms of droplet sizes produced from syringe for conventionally illuminated experiments 85

3.18 Histograms of droplet sizes produced from syringe for BB-LIF experiments 86

3.19 Mean droplet speeds for 2 mm and 3 mm impinging droplets 86

3.20 Calculation of the absorption coefficient 91

3.21 Steps of BB-LIF processing 92

3.22 Histogram of Film-height values, showing the thresholds used for feature detection 94

3.23 Detection of crown and crater using the Thresholding technique 95

3.24 Detection of Droplet material from thresholding of the High-Speed Camera images. 96

3.25 Histogram of intensity values from 3.24a 97

4.1 Impingement outcomes against δ and K_C calculated using Droplet Velocity (V_d) showing agreement with the static film boundaries of $K_{C(V_d)} = 700$ & $K_{C(V_d)} = 2100$ 100

4.2 Statistical analysis of impingement outcome probabilities 101

4.3 Crown Splashing occurrences separated by Impingement angle against $K_{C(V_d)}$. Showing similar behaviours for $10 < \alpha, 30$, and a much more gradual transition at a higher value of $K_{C(V_d)}$ when $\alpha = 40$ 103

4.4 Comparison of experimental data to other derivations of the splashing parameter 105

4.5 Prompt and Progressive crown splashing exhibited during a single impingement at $\delta = 0.87, We_d = 442, Re_f = 17283$ 108

4.6 Surface undulations on a ligament undergoing progressive splashing, at various times after impingement 109

4.7 Recessive Crown Splashing $\delta = 1.18, We_d = 58, Re_f = 17283$ 111

4.8 Interstitial Droplets formed during Recessive Crown Splashing at $\delta = 0.87, We_d = 177, Re_f = 17283$ 111



4.9 Number of secondary droplets against $K_{C(Vn)}$ showing agreement with the $K_{C(Vn)}^{1.8}$ relationship from Okawa et al. [19] at higher values. 114

4.10 $K_{C(Vn)}$ against δ chart for splashing on the upstream and downstream sides of the crown, showing that crown splashing is not observed on both sides until $K_{C(Vn)} = 4000$ 115

4.11 Probability of symmetric and asymmetric splashing across the range of $K_{C(Vn)}$ 116

4.12 Secondary droplet sizes against time of formation compared to the data from Cossali et al. [20] 117

4.13 Nondimensional size of secondary droplets against dimensionless time of formation separated by splashing type. The line of best fit is described by the equation shown. 118

4.14 Secondary droplet velocity against dimensionless time of formation separated by primary droplet diameter 119

5.1 Comparison of BB-LIF data to side-view images, Colour-bar showing height in mm for the lower (plan view) image 123

5.2 Sample 3D image from the BB-LIF data, showing erroneous readings within the crown due to internal reflections. Colour-bar showing height in mm 124

5.3 2 mm Droplet Impingements, $\delta = 0.75$. Colour-bar showing height in mm 127

5.4 3 mm Droplet Impingements, $\delta = 0.71$. Colour-bar showing height in mm 127

5.5 Side profile of cavity, exhibiting flattening as it approaches the base of the channel 128

5.6 2 mm Droplet XT diagrams when $\beta = We_d^{-0.13}/\sqrt{\delta}$. Colour-bar showing height in mm 130

5.7 3 mm Droplet XT diagrams when $\beta = We_d^{-0.13}/\sqrt{\delta}$. Colour-bar showing height in mm 131

5.8 Cavity width expansion coefficient (β) compared to droplet Weber number We_d 133

5.9 We_h against β . showing multiple datasets, and an unresolved dependence on primary droplet diameter (D) and film height (h_f) 134

5.10 We_d against $\beta \cdot \sqrt{\delta}$, showing collapse onto a single line for the values of β from moving film experiments 135

5.11 Droplet Spreading within the cavity against the model from Roisman et al. [6] for $D = 2\text{ mm}$ 138

5.12 Droplet Spreading within the cavity against the model from Roisman et al. [6] for $D = 3 \text{ mm}$ 139

5.13 Dye-trails indicating interfacial mixing between the droplet and film 140

5.14 Types of Crown Skew (*film flowing left to right*) 141

5.15 Diagram showing velocity components between the film and droplet 142

5.16 Upstream and Downstream splashing plotted against the ratio of droplet and film velocities 143

5.17 Probability of upstream and downstream splashing plotted against the ratio of droplet and film velocities 144

5.18 Maximum Crown width against Re_d 145

5.19 Comparison of crown heights at $Re_d = 5998$ and $Re_d = 9750$. . 146

5.20 Crown Schematic 148

5.21 Crown propagation against the model from Roisman et al. [41] . 150

5.22 Fitting for the a term from Eqn. (5.4) against We_d/δ 151

5.23 2 mm Impinging droplets against crown model 153

5.24 3 mm Impinging droplets against crown model 154

5.25 156

5.26 Development of crown in upstream and downstream directions, showing a typical result 156

5.27 Upstream and downstream crown development against width model 158

5.28 Upstream and downstream crown development against width model 159

List of Tables

2.1	Transition values of $K = We Oh^{-0.4}$	23
3.1	Calibration of the Flowmeter	69
3.2	Experimental Parameters	70
3.3	Key nondimensional film parameters at 10 °.	79
3.4	Key nondimensional film parameters at 20 °.	79
3.5	Key nondimensional film parameters at 30 °.	79
3.6	Key nondimensional film parameters at 40 °.	79
3.7	Impingement Outcome Classification	87
3.8	Droplet production mechanism criteria	89
4.1	Transition Equation Coefficients for Eqn. (4.2) when V_d is used in the calculation of $K_{Cossali}$	103
4.2	Transition Equation Coefficients for Eqn. (4.2)	104

<u>Latin</u>		
Symbol	Meaning	Units
a	Fitting Constant	
a_r	Deceleration of the crown's rim with time	m/s^2
b	Fitting Constant	
CPF	Cumulative probability function	
B_l	Lower bound for Keyence sensor	
B_u	Upper bound for Keyence sensor	
c	Fitting Constant	
D	Droplet diameter	mm
D_{sd}	Secondary droplet diameter	mm
DL	Digital Brightness Level from Infra-red Camera	
g	Acceleration due to gravity	m/s^2
h_c	Film thickness underneath cavity	mm
h_f	Film height	mm
\bar{q}	Volume flow rate along channel	l/m
\bar{Q}	Volume flow rate along channel	m^3/s
N	Number of secondary droplets	
r_0	Radius of the crown-rim	mm
R_{surf}	Surface micrometer reading from keyence sensor	μm
R_{base}	Base micrometer reading from keyence sensor	μm
t	Time	s
V_d	Droplet velocity	m/s
V_f	Film velocity	m/s
V_n	Droplet velocity normal to film	m/s
V_{sd}	Velocity of secondary droplet	m/s
V_{surf}	Voltage reading at surface from Keyence Sensor	V
V_{base}	Voltage reading at base from Keyence Sensor	V
V_t	Droplet velocity parallel to film	m/s
\bar{y}_{cr}	Crater depth	mm

<u>Greek</u>		
Symbol	Meaning	Units
α	Impingement Angle	°
α_0	Constant from Bisighini et al [24]	
α_{abs}	Absorption Coefficient	cm^{-1}
α_c	Circle diameter for Bisighini et al depth model [24] Eqns. (2.19,2.20)	
β_{Rois}	Expansion coefficient from Roisman et al [42]	
$\beta_{Hinsberg}$	Expansion coefficient from Van Hinsberg et al [43]	
β_{Hann}	Expansion coefficient from Hann et al [44]	
$\beta_{Mitchell}$	Expansion coefficient calculated from this study	
α_0	Constant from Bisighini et al [24]	
$\Delta_{max,deep}$	Maximum crater depth for equivalent deep pool impact	
ζ	Axial offset for crater model from Bisighini et al [24]	
μ	Dynamic Viscosity	$Pa \cdot s$
ν	Kinematic Viscosity	m^2/s
ρ	Fluid density	kg/m^3
σ	Surface Tension	N/m
σ_{est}	Standard Error of Estimate	
ψ	Circle Radius for crater model from [24]	
ψ_0	Experimentally Determined constant associated with original cavity radius	

Nondimensional Parameters

Symbol	Meaning
Bo^{-1}	Inverse Bond number $Bo^{-1} = (\sigma/\rho a_r)/r_0$
$K_{Cossali}$	Splashing parameter Cossali et al. [8]
$K_{C,(Vd)}$	$K_{Cossali}$ calculated using V_d
$K_{C,(Vn)}$	$K_{Cossali}$ calculated using V_n
K_{Gao}	Splashing parameter from Gao et al. [45]
K_{Mundo}	Splashing parameter from Mundo et al. [15]
$K_{Huang(thin)}$	Thin film Splashing parameter Huang & Zhang [46]
$K_{Huang(thick)}$	Thick Film Splashing parameter Huang & Zhang [46]
Oh	Ohnesorge Number $(Oh = \frac{\sqrt{We}}{Re})$
Re	Reynolds Number $(Re_d = \frac{\rho_d v_d d}{\mu_d})$
R_h	Hydraulic Diameter $(R_h = [h_f * width] / [(2 \times h_f) + width])$
ξ	Dimensionless Crown Size $(\frac{length}{D})$
ξ_l	Dimensionless Crown Length $(\frac{length}{D})$
$\xi_{l,d}$	Dimensionless Crown Length (downstream direction) $(\frac{length}{D})$
$\xi_{l,u}$	Dimensionless Crown Length (upstream direction) $(\frac{length}{D})$
ξ_w	Dimensionless Crown Width $(\frac{width}{D})$
$\xi_{w(max)}$	Maximum dimensionless Crown width $(\frac{width}{D})$
We	Weber Number $(We_d = \frac{\rho_d v_d^2 d}{\sigma_d})$
δ	Dimensionless film height $(\frac{h_f}{D})$
τ	Dimensionless Time $(\frac{tV}{D})$
τ_0	Dimensionless Delay Time $(\frac{tV}{D})$
τ_m	Dimensionless Time including film velocity $(\frac{t(V_{drop} \pm V_{film})}{D})$
τ_r	Dimensionless Time based on radius $(\frac{t(V_{drop} \pm V_{film})}{R})$
Ω	Dimensionless Cavity width $(\frac{width}{D})$
Ω_{drop}	Dimensionless width of droplet spread $(\frac{width}{D})$

Chapter 1

Introduction

The impingement of droplets is a field which has been studied for well over 100 years from initial investigations into the patterns left by falling droplets [31], early photographic investigations [32], to contemporary experiments using sophisticated visualisation and measurement techniques [44]. This complex, multi-phase situation presents itself across a variety of applications. Bearings, printers, fuel injection and spray painting all involve droplets impinging upon surfaces. As the commercial and legislative constraints tighten in our increasingly environmentally conscious world, the desire to maximise efficiencies is obvious.

1.1 Rationale

Jet propulsion is one of the leading propulsion technologies in both military and civilian aviation, with air passenger numbers in 2015 being four times greater than in 1980 [47]. Due to the environmental and climate issues exacerbated by increasing air travel, there are ever-tightening emissions regulations, and taxation. This in turn creates the need to reduce emissions, increase efficiency, and reduce maintenance costs. The design of aero-engines is continuously evolving and improving.

The bearings in an aero-engine are particularly important, as these hold a shaft rotating at high angular velocities in place to tight tolerances. Failure of a bearing may cause the entire engine to become inoperable, offering significant safety concerns and operational costs.

To avert these failures, a rigorous inspection and maintenance regime is imposed, this typically includes examination of the engine both by eye and with a borescope, and replacement of all engine fluids that have begun to degrade.

Replacing engine fluids, and their safe disposal is often costly and requires the aircraft to be ‘grounded’ whilst the procedure is ongoing, obviously meaning that it cannot be in commercial service. Alongside these safety concerns, it is desirable to reduce the parasitic losses associated with the bearings and bearing chambers. As the rapidly rotating shafts cause shearing forces on the air, and droplets or mist entrained within this air can cause these losses to become more significant, in turn increasing fuel consumption, emissions and operating expense.

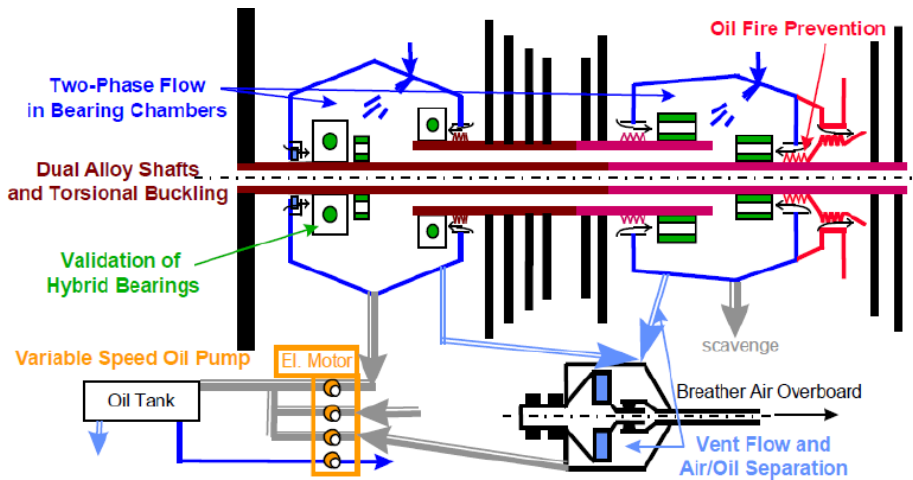


Figure 1.1: Oil flow within a typical aero-engine from Klingsporn et al [1]

Therefore, to reduce losses and increase the number of operational hours between maintenance activities, it is desirable to increase the life of engine oils and lubricants. This can be undertaken in two ways, the development of new lubricant compounds, or by redesigning the engine to reduce the rate of lubricant loss, and degradation.

A typical aero-engine oil system will include a storage tank, a pump to supply oil to the bearing and gear systems to provide lubrication and cooling. After passing through a bearing, the oil enters a surrounding chamber, commonly referred to as the bearing chamber. This area is sealed from the engine, and current understanding [48] is that the oil travels from the bearing in the form of droplets and ligaments of fluid to create a film on the chamber walls. This film then enters a scavenge duct, under shearing forces and gravity, finally before re-entering the oil system as shown in Fig. (1.2). Due to proximity of bearing chambers to compression systems and combustion equipment, the chamber walls are at a high temperature across all areas of the engine load cycle. These high temperatures are understood to be one of the principle causes of oil degradation, and the formation of secondary droplets or mist when the droplets

impinge upon the walls causes an increase in parasitic losses from the engine. Therefore, increasing knowledge of this environment is of paramount importance to aid bearing design.

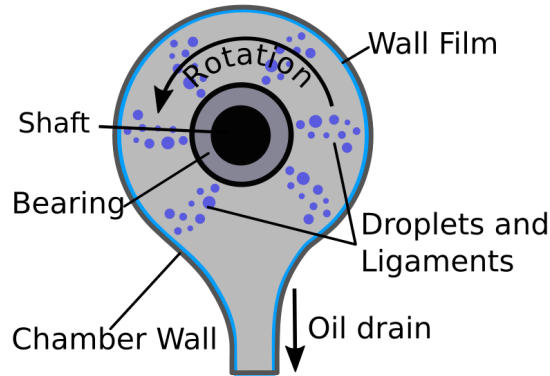


Figure 1.2: Typical oil flow within a bearing chamber (cross section)

Unfortunately, full scale testing rigs are prohibitively expensive, and even if available, would be almost impossible to access with instrumentation capable of gathering detailed information on oil behaviours and interactions within the bearing. Therefore, the majority of work has either consisted of intermediate scale testing rigs, working at room temperature and pressures, substituting water for oil, or through computational methods such as Computational Fluid Dynamics (CFD) or Smoothed Particle Hydrodynamics (SPH).

Although it is possible to compute individual droplets impinging upon chamber walls with extreme precision using these methods, such as in the work by Peduto [49], to do so on the scale of a complete bearing chamber would be highly computationally expensive. An approach proposed by Adeniyi et al. [2] to reduce the computational cost of simulations is to separate the impingement into two components; the production of droplets, and the heat and mass transfer to the wall-film. This is shown in the schematic in Fig. (1.3). This is undertaken by the use of experimentally derived correlations in lieu of complex simulations of every impingement within the bearing chamber. Although a review of the literature shows that many correlations exist for droplet impingements on static films, few of these have been shown to be also on moving films. Furthermore, in some cases, such as the splashing parameter discussed in section 2.1.2, there is a lack of consensus, with many correlations and forms of nondimensionalisation being proposed by various authors throughout the literature. All of which makes clear the pressing need for more study into this field.

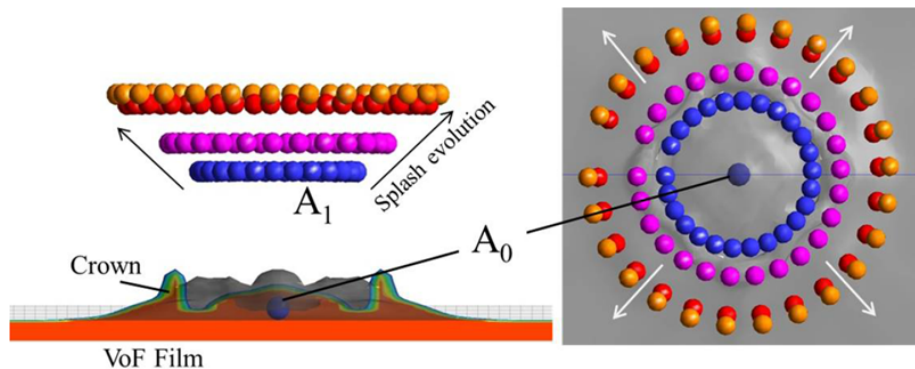


Figure 1.3: The combined Discrete Particle Modelling/Volume of fluid approach used to model droplet impingements [2]

1.2 Aims and Objectives

This work aims to understand the differences between static and moving film impingements, and to establish to what extent static film correlations can be applied to moving film impingements. Further, the thesis aims to establish changes and improvements to more accurately represent moving film scenarios. In droplet production, crown formation, and cavity expansion. This will be undertaken using a multi-faceted approach:

- Experimental investigations into the production of secondary droplets and mist following a moving-film impact, including the conditions under which secondary droplets are produced, alongside the size, velocity, quantity, and separation mechanics of these droplets. This new data for moving films is compared to static film literature to understand the effects of this differing target parameters. This work is presented within chapter 4.
- Cavity dynamics, including cavity development and droplet spreading within the cavity. Crown dynamics, including crown asymmetry, maximum diameter, and development are also investigated. These parameters are compared to existing static film correlations and physical understanding from static film and solid substrate experiments. This work is presented in Chapter 5.

1.3 Structure of Thesis

- Chapter 2 provides a full review of prior literature that underpins the work presented within this thesis. There have been numerous studies into both

normal and oblique impacts onto static films and solid substrates, classifying impingement outcomes based on several nondimensional groups. A summary of this work is presented within the first part of this chapter. The second part of chapter 2 includes a review of experimental techniques, data acquisition methods, and data analysis methodologies relevant to the current investigation.

- Chapter 3 presents an overview of the experimental testing rig used to gather data for this work. A description of the rig and details regarding droplet generation are given in section 3.1. Information relating to characterisation of the inclined channel is supplied in Section 3.2. Section 3.3 focuses on the methods of data acquisition, outlining details of the cameras, illumination, laser systems and the brightness-based laser induced fluorescence (BB-LIF) technique. Analysis of the data is covered in section 3.4 (for conventional lighting) and 3.5 (for BB-LIF)
- Chapter 4 is the first results chapter. This focuses on secondary droplet production. The transition between different impingement outcomes are compared to static film understanding, and a robust statistical method novel to the field is applied for determining these transitions. Crown splashing is examined in detail, and high-quality images are presented, of the different types of splashing. New correlations are developed to describe the number of secondary droplets, to characterise behaviours unique to moving-film impingements. Finally, the size and velocity of secondary droplets is investigated and correlations for each are derived. Some of this work has been submitted for journal publication, and preliminary studies on the splashing threshold have been presented at the 2015 American Society of Mechanical Engineers International Mechanical Engineering Congress & Exposition [50].
- Chapter 5 forms the second results chapter, and focuses on the morphology and development of the crown and cavity. Both the shape and development with time are explored and comparison is made to models derived for impingements on static films. Modifications to these models are proposed. Using the laser induced fluorescence, it was possible to determine the movement of the droplet fluid within the cavity. Preliminary work for this chapter was presented at the 2017 American Society of Mechanical Engineers Turbomachinery Technical Conference & Exposition [51]
- The implications and applications to bearing chamber modelling of this work are discussed in chapter 6. Furthermore, the contributions to knowl-

edge are given, and potential future works are also explored.

Chapter 2

Literature Review

As discussed in the introduction, there is a need for more research into droplet impingements, specifically relating to moving films, droplet generation and heat transfer, to assist in bearing-chamber design. Whilst contemporary computational methods can simulate an entire bearing chamber, the computational expense of these simulations makes widespread implementation of these techniques prohibitive.

One common method to reduce computational expense is to include empirically derived correlations, which allows simplification of each individual impingement. This chapter aims to summarise the current understanding regarding experimental investigations and correlations, and to identify fields in which an experimental programme will provide assistance into computational simulations.

The topics covered within this chapter are:

- An overview of impingement outcomes and key dimensionless groups. (Section 2.1)
- A summary of droplet impingements of solid surfaces, static films, and moving films. (Section 2.2)
- A compilation of empirically derived models and correlations from static films for comparison to moving film experiments. (Section 2.4)
- Methods of data acquisition, including high speed cinematography, and Laser Induced Fluorescence (LIF). (Section 2.6)
- The challenges of image analysis, and methods to overcome these. (Section 2.8)

2.1 Overview of Droplet Impingement

Most research into the impingement of droplets has been conducted for impacts upon a solid substrate or stationary films, and these situations differ from a moving film. However, this research gives an insight into impingement dynamics and provides a useful comparison to understand the differences between static and moving films. This review of literature will first examine the types of outcomes observed during droplet impingements on solids and static liquid films, alongside the key dimensionless parameters. Secondly literature relating to the effect of solid surfaces, static films, oblique impingements and moving films will be considered. Finally, attempts at modelling key characteristics of the droplet impingements on static films will be summarised for comparison with the moving film experiments in later chapters.

2.1.1 Impingement Outcomes

Perhaps the most immediately apparent result of a droplet impingement is the impingement outcome. This is where the droplet may hit a surface or film and leave barely a ripple, or produce vast plumes of droplets and towering crown-like structures. The impingement outcomes for solid surfaces are first discussed, as the fluid behaviours can be considered more basic, before moving onto static film impingements.

Solid Substrates

To discuss droplet impingements and their outcomes, it is first necessary to understand the commonly used terminology to differentiate between different types of impingement outcomes. As previous authors have shown that the behaviour of droplet material for static film impingements has significant similarities with models from solid substrates [44]. Therefore, it was deemed prudent to review aspects of solid-substrate literature relating to movement of the droplet material. This included the production of droplets and ligaments, and spreading of droplet fluid on the surface.

Rioboo et al. [3] investigated droplet impacts onto solid surfaces, and provides comprehensive descriptions of six different types of impingement event observed upon solid surfaces. These are: *Deposition*, *Prompt Splash*, *Corona Splash*, *Receding Breakup*, *Partial Rebound*, and *Rebound*. Alongside a description below, Fig. (2.1) shows images of these outcome regimes, from Rioboo et al. [3]

- *Deposition* was described as when the drop deforms, staying attached to the surface, with no material being ejected in the form of droplets.
- *Prompt Splash* was described as when secondary droplets are formed at the point of contact in the initial stages of droplet spreading.
- *Corona Splash* (called *Crown Splash* by others) is when droplets are formed from the rim of fluid that forms around the impingement site
- *Receding breakup* is related to wettability of the substrate, as the droplet material retracts after an impingement, small droplets of fluid are left on the surface away from the main body of the droplet
- *Partial Rebound* and *Rebound* is when either all, or some of the droplet material contracts energetically after spreading, causing all or some of the fluid to be ejected upwards, forming a secondary droplet from a central jet

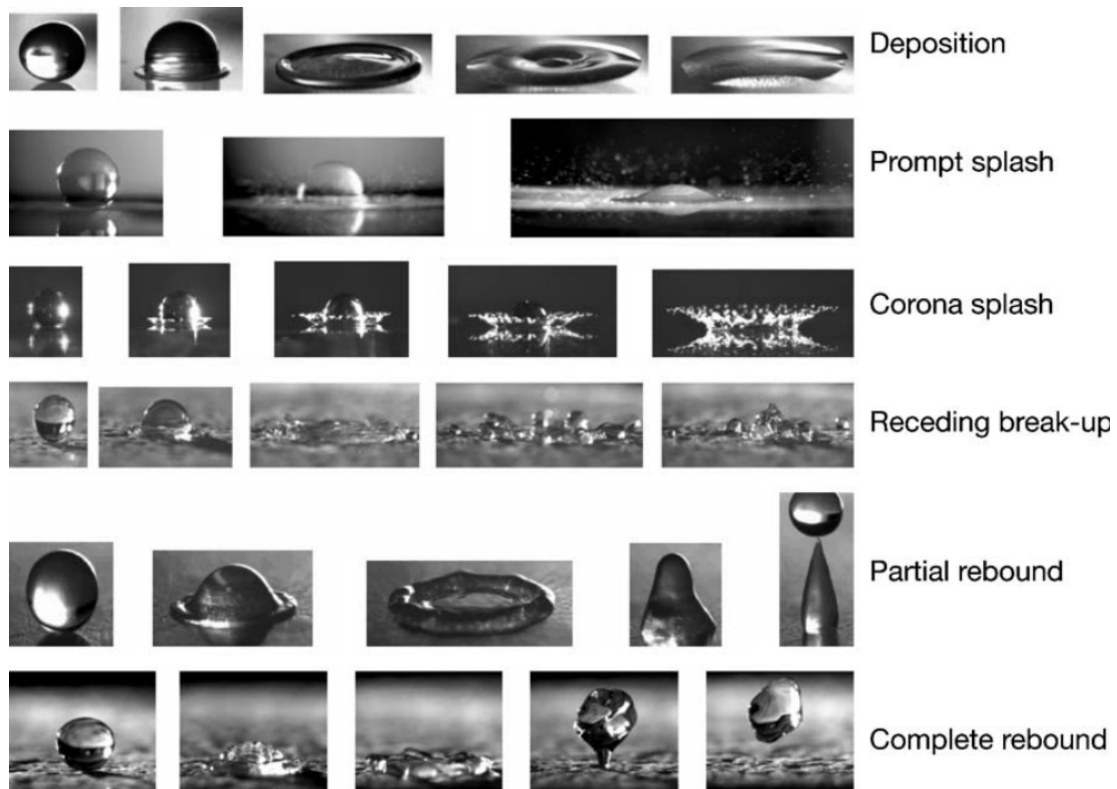


Figure 2.1: Types of Solid-Substrate Impingement outcomes from Rioboo et al. [3]

Static Films

Whilst there are a great number of parameters and behaviours which can be investigated for droplet impingements upon static films, the most readily apparent of these is the impingement outcome. In many respects impingement outcomes on static films have similarities to solid substrates. One of the first works to classify these outcomes was performed by Worthington [4]. Since then, various authors [4, 10, 8, 52, 53] have built upon this early work, and there are several commonly agreed upon impingement outcome regimes, these are;

- **Floating** - the droplet floats on a cushion of air above the surface of the film, typically this requires a very low droplet Weber number (We_d)
- **Coalescence** - The droplet joins with the film, causing little disturbance to the surface, with no material being ejected.
- **Crown Formation** - The droplet-impact results in formation of a corona or crown. This is a curtain of fluid that may have ligaments forming off it. This crown propagates outwards from the impingement site before collapsing and rejoining the film. The crown formation is typically accompanied by the formation of a crater or cavity within the film around the impingement site.
- **Crown Splashing** - Similar to crown formation, however secondary droplets are formed from the crown.
- **Jet Formation** - The droplet-impact produces a crater at the impingement site, upon the collapse of this crater, a jet of fluid emerges from the centre of the crater, propagating approximately vertically upwards in the case of impact with a static film
- **Jet Breakup** Similar to jet formation, however a secondary droplet or droplets are formed from the jet breaking up due to Rayleigh instability.

Examples of these behaviours are shown in Fig. (2.2).

The first of these to be classified was the *Jet Formation* by Worthington [4] in 1908. An example of this is shown in Fig. (2.2c). In instances where the jet produced a secondary droplet, such as in Fig. (2.2d). It should be noted that in the original work Worthington referred to this a *breaking off* however, the contemporary terminology is *Jet Breakup*.

Cossali et al. [8], differentiated between *Crown Formation* and *Crown Splashing*; in the latter case there is production of secondary droplets. If droplets were formed from the crown the impingement was categorised as a *splashing event*. Throughout the course of this work, the following definitions will be used, *Crown*

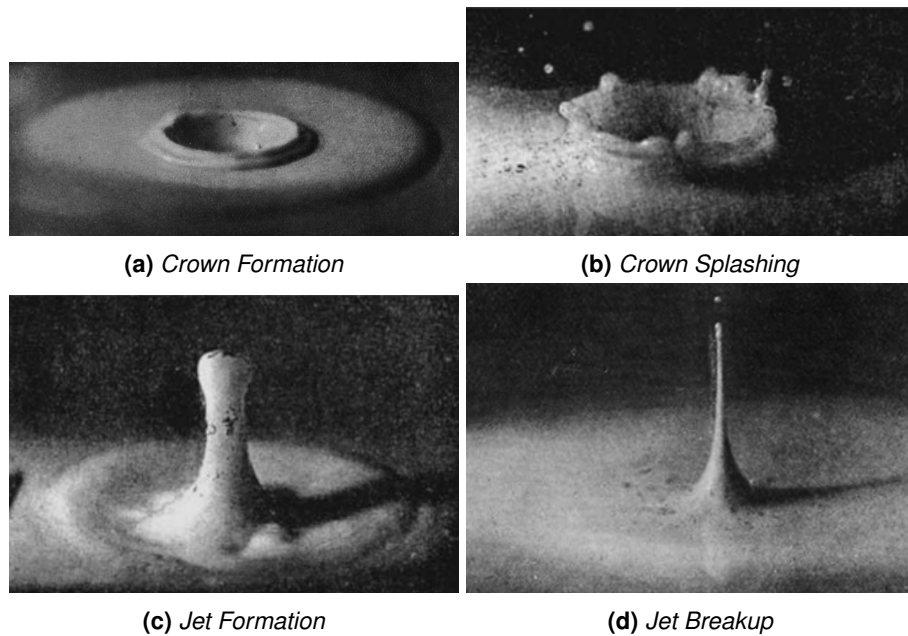


Figure 2.2: Impingement outcomes observed by Worthington [4]

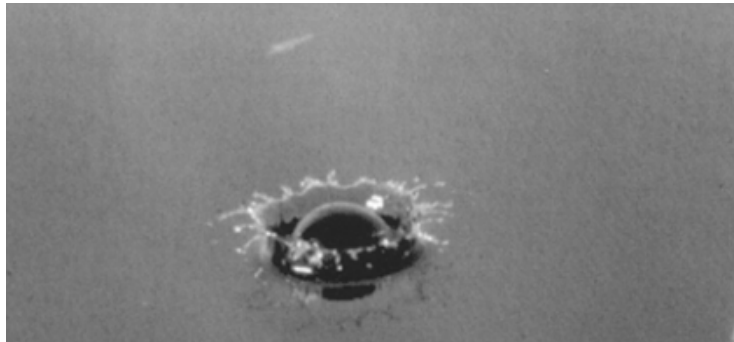
Formation will indicate where a crown is formed, but no secondary droplets, and *Crown Splashing* will denote an event where the crown forms secondary droplets from its rim.

A particular type of crown splashing shown in Fig. (2.3) is described by Worthington [4] as *bubble building*, where the crown begins to close in upon itself, forming a hemispherical bubble above the cavity. This behaviour has also been observed by more recent authors (for example [54]) and has been described as *bubbling*.



Figure 2.3: *Bubbling* observed by Worthington [4]

Cossali et al. [8], remarked that prompt splashing occurred at low values of Oh . Furthermore, it is found that *prompt splashing* needs less energy, and therefore a lower We_d to occur compared to crown splashing. A visually similar phenomenon is observed for solid sphere-film impingements, this was described as *basket splashing*, and is evident in Fig. (2.4b).



(a) *Prompt Splashing* observed by Cossali et al. [8]



(b) A photograph from Worthington [4], showing *Basket Splashing* caused by a solid sphere

Figure 2.4: Prompt and Basket Splashing

2.1.2 Dimensionless Parameters

Dimensionless parameters are commonly used throughout literature to define various aspects of the impinging droplet and their outcomes.

Film Thickness

For static film impingements, many authors [20, 44, 42] have used the dimensionless film thickness. There is strong consensus in this field, and the commonly agreed form is to relate the film height to the impinging droplet diameter, as shown in Eqn. (2.1).

$$\delta = \frac{h_f}{d} \quad (2.1)$$

Time-scale

Another commonly used parameter is the dimensionless time-scale τ_r . This is used to represent the time over which the impact takes place. One of the

earlier definitions of this is from of Stow and Hadfield [5], who proposed a form based on time, droplet velocity, and droplet radius as shown in Eqn. (2.2)

$$\tau_r = \frac{tV}{r} \quad (2.2)$$

More recent authors [41, 6, 24, 25, 44] have preferred to relate τ to the droplet diameter, as shown in Eqn. (2.3), this form will be used in this thesis.

$$\tau = \frac{tV}{d} \quad (2.3)$$

Impinging Droplet Characteristics

In the reviewed literature, several nondimensional groups are used to define the droplet characteristics, and help determine if an impact event will result in secondary droplet production. The most commonly used were the Weber Number (We), Reynolds Number (Re), and Ohnesorge Number (Oh). It is possible within moving film scenarios to calculate these parameters for both the impinging droplet, and the target film. Therefore, it was decided that for clarity to use the subscript f to represent when these parameters are calculated for the film. Conversely, lack of a subscript, or a d subscript indicates that these parameters are calculated for the droplet.

Frohn and Roth [55] also remark on the importance of the Froude Number (Fr) and the Laplace Number (La). The reviewed literature placed significant importance upon the Weber number in the determination of droplet outcomes [56, 8, 15]

However, within the literature it is more common to associate impact outcomes with two or more of the above parameters, in a form commonly referred to as the *splashing parameter* (K). Several of these relationships are detailed below. For clarity each expression is referred to by placing the name of the primary author in subscript.

Stow and Hadfield [5] proposed a nondimensional parameter as shown in Eqn. (2.4) for impingements on solid substrates. This is interesting as it is identical to the parameter used later to characterise static film impingements by Cossali et al. [8].

$$K_{stow} = We \cdot Oh^{-2/5} \quad (2.4)$$

Mundo et al. [15], also developed a splashing parameter to nondimensionalise the boundaries between impingement outcomes on solid surfaces. This is defined in Eqn. (2.5). It was found that above $K_{Mundo} = 57.7$, splashing outcomes are observed, where secondary droplets are ejected from the rim of fluid

forming around the droplet, whereas below this value, deposition is observed.

$$K_{Mundo} = Oh \cdot Re^{1.25} \quad (2.5)$$

Cossali et al. [8] defined $K_{Cossali}$ as Eqn. (2.6) for droplet film interactions. This parameter has been used subsequently by many authors, such as Alghoul [57], Rioboo et al. [9] Okawa et al. [10] and Marengo and Tropea [58]. However, more recently other impact parameters have been proposed.

$$K_{Cossali} = We \cdot Oh^{(-0.4)} \quad (2.6)$$

Another version of the K parameter was proposed by Hunag and Zhang [46] as in Eqn. (2.7) which for their thick-film experiments was found to better describe the transitions from bouncing to coalescence, coalescence to jetting, and coalescence to splashing for droplets of water and oil. And Eqn. (2.8) for thinner films ($\delta < 1.3$). Differentiation between thin and thick films is discussed in section 3.2.

$$K_{hunag(thick)} = We^{0.375} \cdot Re^{0.25} \quad (2.7)$$

$$K_{hunag(thin)} = (We \cdot Re)^{0.25} \quad (2.8)$$

One of the more recent proposals for splashing parameter is that of Gao et al. [45], for impingements upon moving films with thicknesses of 0.2 mm. This included characteristics of both the droplet and film in its calculation. The transition between coalescence and splashing was found at $K_{Gao} = 3378$.

$$K_{Gao} = We \cdot Re^{1/2} (1 + \delta V_f^2) (1 + \delta V_f)^{1/2} \quad (2.9)$$

Of these splashing parameters, it was observed that for droplet to film impingements, the use of $K_{Cossali}$ is by far the most prevalent, with many boundaries defined (see Section 2.2.2). It is anticipated that this form will be used primarily due to the wealth of static film literature.

2.2 Impingements on solid substrates and static films

Section 2.1.1 detailed the generic outcomes for impingement events, and the parameters typically used to predict expected outcomes. This section provides a full literature review for impingements on solid substrates and moving films, and outlines in more detail into droplet impingements on solid substrates, static films. However, for the interest of clarity, moving substrates are discussed in section 2.3.3, and empirically derived models are considered separately in section 2.4.

2.2.1 Solid Substrates

Although the focus of this work is on droplet impacts on moving films, there are certain parallels that can be drawn from impingements on solid substrates. Whilst the basic outcomes have been previously discussed, to provide background knowledge for the reader, this section consists of more detailed analysis of existing models and physical understanding for solid substrate impingements. This was undertaken as previous studies [44], have shown that the behaviour of droplets impinging on solid surfaces has parallels with the spreading of droplet material for static film impingements.

Droplet Spreading

The thickness and spread of the droplet has significant implications for heat transfer between the droplet and target surface, this section investigates methods used to characterise the deformation and spreading of the droplet after impingement.

Stow and Hadfield [5] produced an early work on the spreading of with droplets with diameters in the range of $2.2 < D < 4.4mm$ upon aluminium and steel plates. The spreading of the droplet was found to be suitably nondimensionalised by use of the dimensionless radius ($R_c^*s = r_c/R_{droplet}$) and the dimensionless time-scale ($\tau_r = tV/R_{droplet}$). This form of nondimensionalisation was shown to work across a variety of droplet radii and velocities as shown in Fig. (2.5).

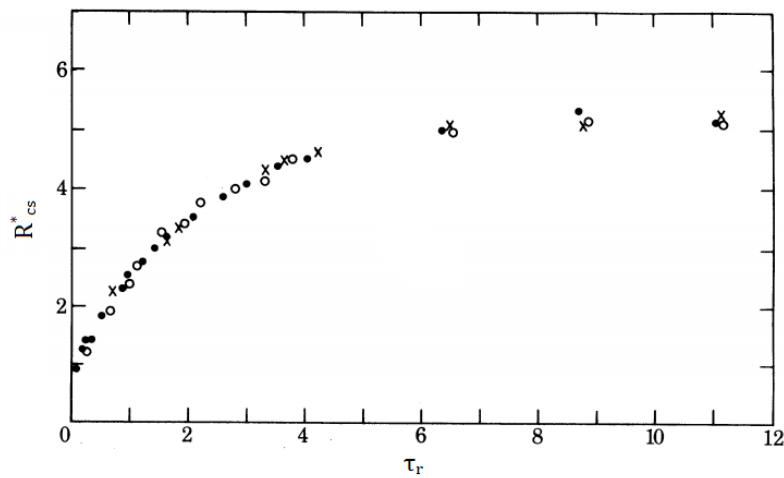


Figure 2.5: Nondimensionalisation of droplet spreading for droplet impingements upon a solid surface from Stow and Hadfield [5]

Scheller and Bousfield [59] investigated droplets of various fluids, with viscosities up to 300 mPa.s, and proposed the empirical relationship shown in Eqn. (2.10). This related the maximum spread of the droplet, to the characteristics of the impinging droplet for various fluids.

$$\frac{2R_{Max}}{D} = 0.61(Re^2 \cdot Oh)^{0.166} = \left(\frac{We}{Oh}\right)^{0.166} \quad (2.10)$$

where:

- $\frac{2r_{Max}}{D}$ is the spread factor
- Re is the droplet Reynolds number
- Oh is the droplet Ohnesorge Number
- We is the droplet Reynolds Number
- D is the droplet diameter
- R_{Max} is the maximum radius of the spread droplet on the wall

Another key aspect of droplet spreading is the thickness of the droplet, and the height that the droplet material tends to after impingement (the plateau height)

Roisman et al. [53] investigated the thickness of the plateau height lamella for droplets of water impinging with very high Reynolds numbers. It was found that the plateau height could be approximated by Eqn. (2.11).

$$h_p = D \cdot Re^{-0.5} \tag{2.11}$$

Roisman et al. [6], derived the relationship in Eqn. (2.12) for the thickness of the droplet fluid at various points along its radius for impingements on solid substrates. This was found to compare well to the numerically derived predictions from Fukai et al. [7] across a range of impingement conditions, and has potential applications to moving-film experiments.

$$h_L = \frac{\eta}{(\tau + \tau_i)^2} \exp \left[-\frac{6\eta r^2}{(\tau + \tau_i)^2} \right] \tag{2.12}$$

where:

- h_L is the height of the lamella
- η is a constant estimated as $\eta = 0.39$ by Roisman et al. [6]
- t is the time
- τ_i is the inverse of the initial gradient of the radial velocity estimated as $\tau_i = 0.25$ by Roisman et al. [6]
- r is the radial location

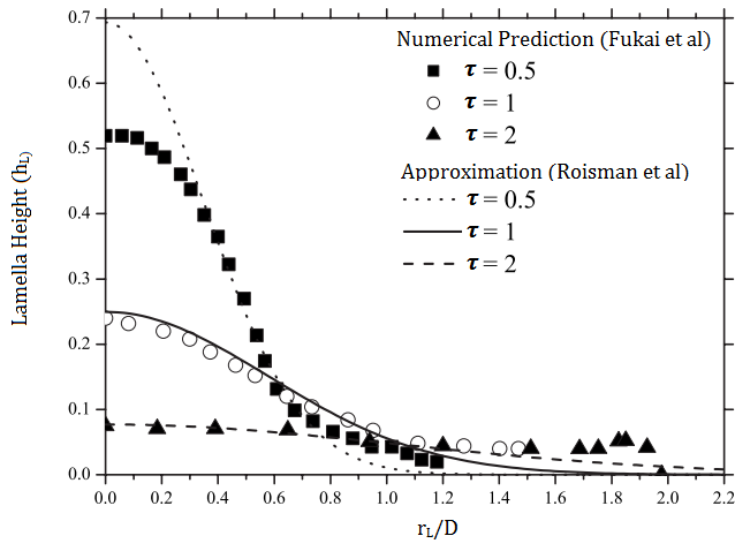


Figure 2.6: A comparison of the approximation from Roisman et al. [6] and the numerical solution from Fukai et al. [7]

This model has also been used by Hann et al. [44] to examine the droplet spreading for impingements upon static films, and there has been compared

moving film data to in the course of this study. This work is presented in section [5.2.3](#).

2.2.2 Impingements upon Static films

The majority of research into upon droplet-film impingements has been undertaken upon static films of varying thicknesses. This provides a useful reference point to compare moving film observations to understand the differences between two impingement scenarios. This includes the transitions between impingement outcomes and the effect of varying the target fluid properties. However, as little of this work has been verified for moving films, it is important to discover the extent to which static film findings can be applied to moving-film impacts.

Transitions within the $K_{Cossali}$ Domain

Cossali et al. [8] Investigated the impact of droplets onto wetted surfaces, with the intent to find the boundary between crown formation and crown splashing behaviours. Transition regimes for water showed a dependence on the dimensionless film thickness ($\delta = h_f/D$), and the transitions was reported at $K_{Cossali} = 2100 + 5880(\delta)^{1.44}$ for $\delta < 0.2$ for the transition between crown formation and crown splashing. This investigation used primary droplet diameters between 2 mm and 5.5 mm. This relationship is illustrated in Fig. (2.7).

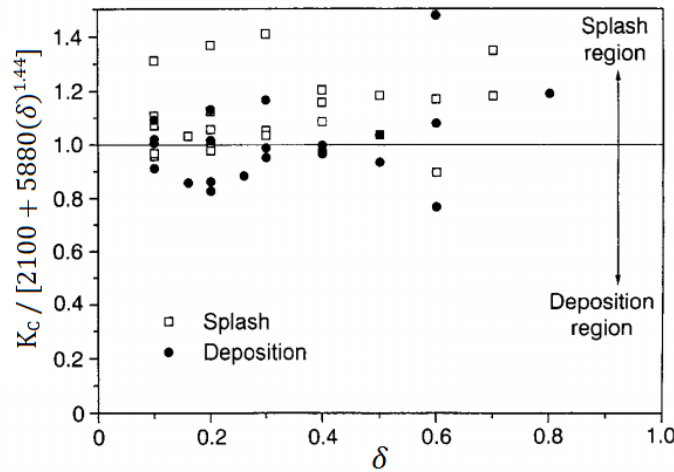


Figure 2.7: Graph showing the splashing parameter ($K_{Cossali}$) against the non dimensional film thickness from Cossali et al. [8]

Coghe et al. [60] also compared outcomes to $K_{Cossali}$ and found a transition between crown formation and crown splashing at $K_{Cossali} = 2074 + 870(\delta)^{0.23}$ for $0.1 > \delta > 1$. This boundary gave similar values to that of Cossali et al. [8] and the differences can be attributed to the experiments being performed at

higher values of δ .

Rioboo et al. [9] found limits between crown formation and crown splashing, at $K_{Cossali} = 2100$ for $0.06 < \delta < 0.15$, and between coalescence and crown formation at $K_{Cossali} = 400$ for $0.06 < \delta < 0.15$. These experiments used droplets of glycerol-water and hexadecane with diameters of $1.42 - 3.81 \text{ mm}$. This work also examined the conditions under which crown formation was observed without the creation of secondary droplets, as shown in Fig. (2.8). There was an increase in the *coalescence / crown formation* limit (marked as D-C in the figure), and a decrease in the *crown formation / crown splash* limit (marked as C-S in the figure) below $\delta = 0.06$, this resulted in a reduction of the K_C value range under which crown formation was observed, without also being accompanied by splashing. The authors therefore suggest that crown formation and splashing behaviours exhibit a dependence on dimensionless film thickness.

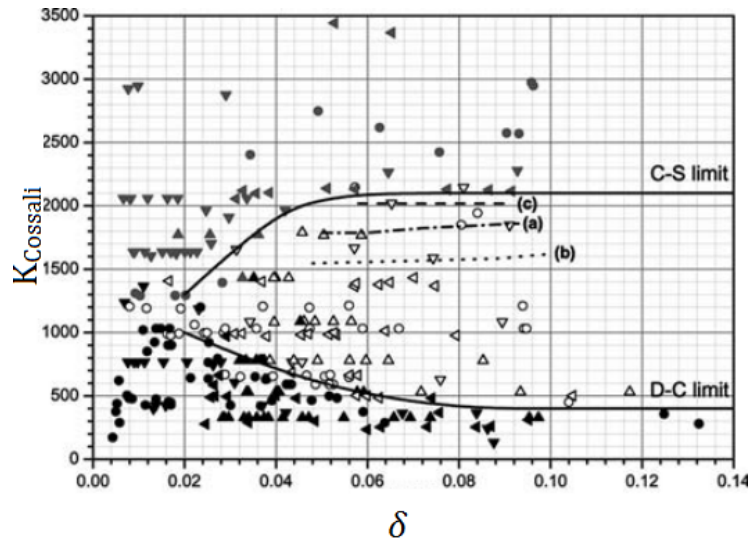


Figure 2.8: A figure from Rioboo [9], showing boundaries between coalescence and crown formation (labelled as the *D-C Limit*), and crown formation/crown splash (labelled as the *C-S limit*).

Wal et al. [61] investigated the boundary between splashing and non-splashing behaviour. From the experiments performed, a chart was produced detailing the effect of Re and Oh upon the type of splashing behaviour.

Okawa et al. [10], further investigated transition regimes, finding that the boundary between crown formation/crown splashing followed the boundary from Cossali for water-glycerine mixtures, however it remains constant for pure water. It is remarked that although the crown formation/crown splash limit is dependent on δ , it is not significantly influenced when liquids with low viscosity such as water are used. This is shown in Fig. (2.9).

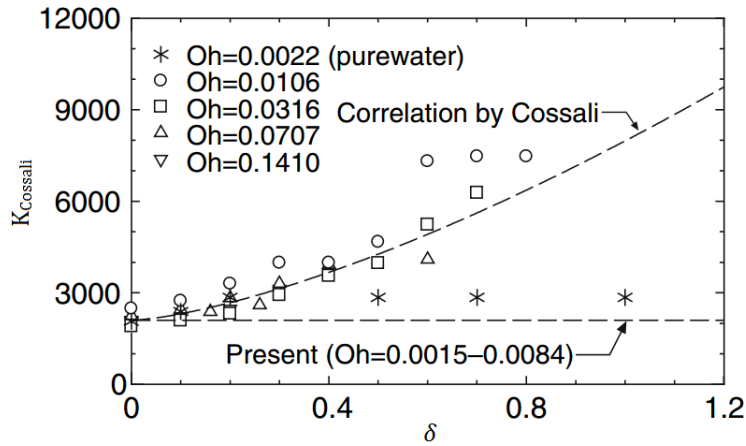


Figure 2.9: A figure from Okawa [10], showing boundaries between Crown formation/Crown Splash for pure water, and water-glycerin mixtures

Okawa also investigated a behaviour named *Sudden Ejection*. This was characterised by the creation of tiny secondary droplets with a trajectory typically normal to the film, but oblique trajectories were also observed. Fig. (2.10) shows that these droplets seem to form at conditions around the $K_{Cossali} = 2100$. Examining the images of this phenomenon, it appears evident that this ‘sudden ejection’ behaviour may in fact be a singular prompt droplet formed after the impingement, as the only occurrences are observed around the minimum threshold for splashing.

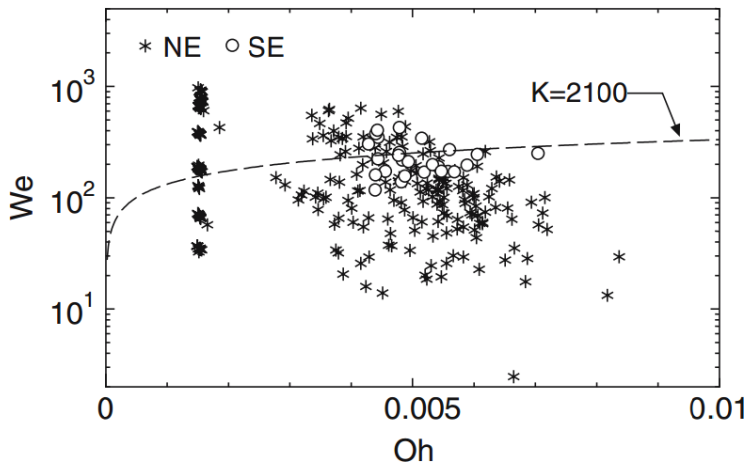


Figure 2.10: A figure from Okawa [10], showing occurrences of Sudden Ejection (SE) and no ejection (NE)

A summary of these transition lines for crown formation and splashing are presented in Table. (2.1).

It is evident that there are a wide variety of overlapping transitions points, and this study has scope to determine which of these are most applicable for moving film impingements.

Effect of Film Thickness

Examining the data in Table. (2.1), it is noticeable that some transition boundaries exhibit a dependence on the dimensionless film thickness (δ), and several studies have examined this field in more detail.

Macklin et al. [63] investigated the splashing of drops on shallow liquids, examining the effect of film thickness on the structure of droplet impacts. It is concluded that for thinner films there are interactions between the film and container base that reduce the jet height. However, on thicker films the jet height increases exponentially with film thickness towards a constant value. This implies that after a certain depth, an increase in thickness has no effect on the splash characteristics.

Macklin followed this research with a study [54] in which paper ethanol and glycerol were used to alter the Weber Number (We), Ohnesorge Number (Oh) and Reynolds Number (Re) of the droplets. It is discovered that the droplet fluid properties effect the ratio of cavity radius size to crown height. Furthermore, in the conclusion, Macklin defines deep splashing as where the bottom of the target liquid container does not affect the impingement behaviours, and shallow impingements as where the cavity is approximately cylindrical. In between these two regimes, the hemispherical nature of the cavity was found to be ‘flattened off’, due to wall effects.

Manzello and Yang [56] investigated the impingement of water droplets onto a pool of water, and a pool of methoxy-nonaflourobthane with pool depths between 2 mm and 25 mm. The experiments encompassed a range of pool depths, and found the critical Weber number for jet breakup is independent of

Table 2.1: Transition values of $K = We Oh^{-0.4}$

Behaviour boundary	K Value	Film Thickness	Source
No crown/crown	400	$0.06 < \delta < 0.015$	[9]
No crown/crown	700	$0.5 < \delta < 2$	[10]
Crown/crown splash	2100	$0.06 < \delta < 0.015$	[9]
Crown/crown splash	2100	$0.5 < \delta < 2$	[10]
Crown/crown splash	$2100 + 5880\delta^{1.44}$	$0.1 < \delta < 0.2$	[8]
Crown/crown splash	$2074 + 870\delta^{0.23}$	$0.1 < \delta < 1$	[62]

pool depth within the experimental regime investigated.

Wal et al. [64] examined the effect of film thickness on the splashing characteristics of droplets. Within the range of $0.1 \leq \delta \leq 1$ it was observed that there were two main types of splashing. *Prompt*, when the droplet initially hits the film, and *delayed*, when the crown begins to recede from its maximum size. Whereas in the range of $1 \leq \delta \leq 10$ the liquid film restricts splashing and splashing behaviours are only observed for the highest energy impingements. Furthermore, when $\delta \approx 10$, *Jet formation and breakup* is observed, whereas this is inhibited on thinner films.

It was noted by Rioboo et al. [9], and Wang & Chen [65], that jet formation is not observed for $\delta < 1$. This region was defined by Cossali et al. [8] as a *thin film*, where the bottom of the channel effects the impingement. Conversely, those impingements happening where $\delta \gg 1$ are defined as *deep pool*. Cossali et al. [8] have placed the transition between thin and thick films to be at $\delta = 2$.

Effect of Fluid Properties

As seen in the previous reviewed literature, the impingement outcomes of a droplet impact are defined by the Weber, Reynolds and Ohnesorge Numbers of the impinging droplet. However, many of the studies using these parameters have only considered the size and velocity of the impinging droplet, with fewer fully considering the effect of fluid parameters such as viscosity, surface tension, and density. As these properties change with temperature, and within an aero-engine bearing the oil changes temperature the effect of these properties on impingement outcomes were investigated. This section reviews the literature investigating cases where the properties of the liquids in the droplet and in the film vary, either through temperature differences, surfactants, or different liquids. However, for the purposes of this work, impingements between immiscible fluids are not considered particularly relevant and are not reviewed, as this is not a situation present in aeroengine oil systems.

Manzello and Yang [66], investigated the impingement of water droplets onto peanut oil. The oil was at a significantly higher temperature (220°C) than the boiling point of the impinging water. Therefore, as the droplet hits the pool of cooking oil it forms a crater similar to that found in previous studies with homogeneous fluids, before the crater closes in upon itself. The droplet then begins to sink under the surface of the oil, before heating up and ultimately producing a vapour explosion due to the evaporation of the entrained water droplet.

In the same year the authors published works involving miscible heterogeneous compounds [67]. This paper investigated the effect of pool temperature

on the critical Weber number for splashing. Droplets at ambient air temperature were observed impinging on a pool at $20\text{ }^{\circ}\text{C}$, $60\text{ }^{\circ}\text{C}$ and $94\text{ }^{\circ}\text{C}$. It was found that the critical Weber number decreased with an increase in temperature. It was also found that an increased temperature caused a decrease in crater depth. This was attributed to the heating element being located at the bottom, creating convective flow within the pool that inhibited crater development.

Manzello [68] compared impingement of water on molten and solid wax with impingement on water. It was found that the critical Weber number (We_c) was dependent on temperature, or the properties of the fluid affected by temperature. This result agrees with previous works by Manzello et al. [67], who were unable to determine a critical Weber number for more viscous fluid, indicating a viscosity dependence on breakup.

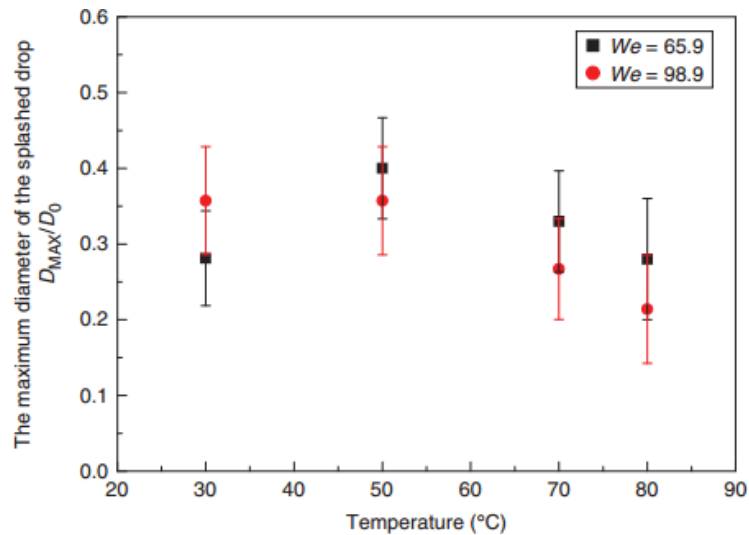


Figure 2.11: Comparison of Critical Weber We_c Number against Temperature from Wang et al. [11]

In 2009, Wang et al. [11], reported on droplets impinging onto hot liquid surfaces. In this paper, water droplets were observed impinging onto alcohol, kerosene and molten ghee (refined butter). Fig. (2.11) shows the relationship between the temperature and nondimensional secondary droplet size for kerosene at various temperatures. This paper only looks a secondary droplets formed by jet breakup, and does not examine the effect of temperature upon the properties of secondary droplets formed by crown splashing in a heterogeneous impingement scenario. It is remarked that these values are lower than in a H_2O -alcohol impact, and explained that since the fluids are miscible in a H_2O -alcohol impingement, the secondary droplet is likely contain alcohol from the pool. It is noted that the maximum size of the secondary droplet is at $50\text{ }^{\circ}\text{C}$,

it is postulated that this is due to the reduction of the dynamic viscosity and surface tension of alcohol above this temperature creating a tendency to form a larger number of small droplets.

Castillo et al. [12] examined the effect of fluid properties on the splashing boundary, obtaining the data shown in Fig. (2.12). From computational simulations (for $Oh < 0.06$) and for experimental investigations with water, alcohol and silicon oil of varying viscosities. This shows a large jump in the required We_d to produce a splash, when Oh_d increases above 0.05. Within this region, the Oh_d was primarily manipulated using silicon oil of varying viscosities. Therefore, this behaviour is attributed to the increased viscosity of the fluid dissipating more energy from the impinging droplet and inhibiting the jet breakup.

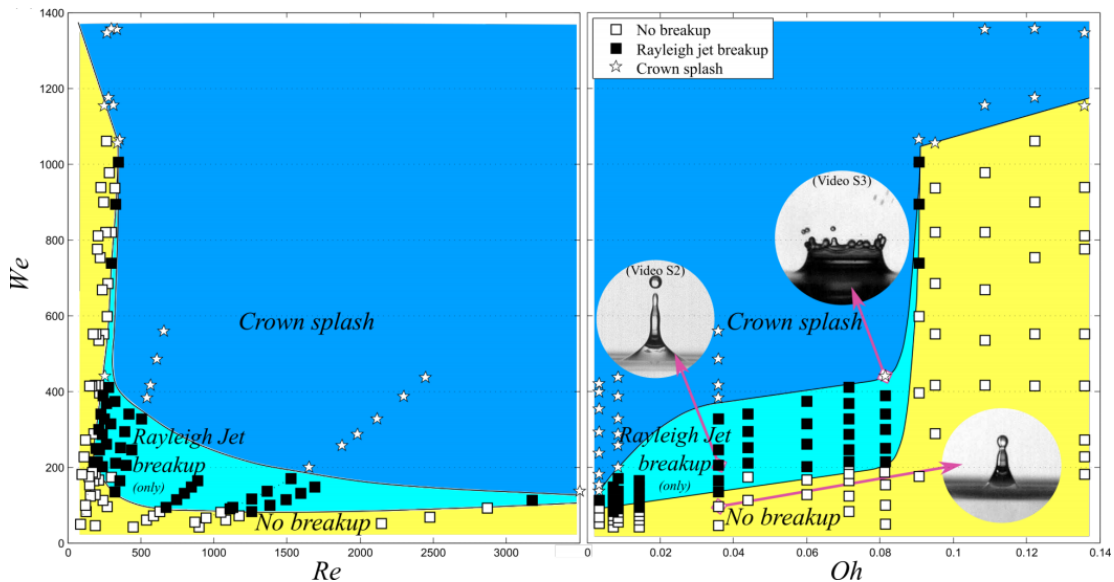


Figure 2.12: Examination of critical Weber Number for various fluids from Castillo et al. [12]

2.3 Moving Substrates and Oblique Impingements

Whilst little work has examined the impingement of droplets upon moving films, there have been a reasonable number of investigations where the velocity vector between the droplet and target has not been aligned perpendicular to the target surface. This includes oblique impingements onto solid surfaces and films, alongside normal impingements onto moving or rotating surfaces. This section summarises the work undertaken in these experimental cases, before finally examining work performed for droplet impingements upon moving films.

For the purposes of this study, *oblique impingement* shall refer to droplet

impinging non-normally upon a surface, whereas droplets impinging normally onto a moving surface will be referred to as *moving substrate impingement*

2.3.1 Oblique Impingement

One of the earliest investigations into oblique impingement was by Jayaratne and Mason [13]. This investigated the transition between coalescing and bouncing droplets for various impingement angles. Through experimental means it was possible to determine a transition line between the two behaviours, as a function of the velocity and the angle of the drop. Furthermore, it was found that the drop size affected this transition region, consistent with later investigations by other authors. Fig. (2.13) The critical velocity of splashing relevant to the impingement angle. This shows a series three self-similar curves for, one for each diameter of impinging droplet. These curves all show a peak at around 45° , indicating the region where it is bouncing behaviours are most easily observed.

Lenewit et al. [14] investigated the effect of angled impingements on the coalescence/bounce boundary for impingements onto static films. Bouncing behaviour was only observed for the impingement angle measured from vertical (α) in the region of $\alpha < 14^\circ$, and not for more highly inclined impingements as shown in Fig. (2.14). This agrees with the work of Jayratne et al. [13], and gives a useful minimum inclination under which bouncing behaviour is not anticipated.

Okawa et al. [19] investigate the effect of oblique impingement angles on impact outcomes. This work divided the droplet velocity into two components, the total velocity of the droplet (V_d) and the component normal to the films surface (V_n). It was found that between angles of $\alpha = 11^\circ$ and $\alpha = 75^\circ$ the droplet velocity (V_d) has significantly more effect upon the impact outcome than the normal velocity (V_n). It is also remarked that the angle caused the impact outcome to become asymmetrical. Furthermore, for impingement angles up to 50° from the normal there is a much larger volume of fluid in secondary droplets compared to the range of 50° to 70° , and that for angles greater than 70° no secondary droplets were produced.

Fang et al. [69] investigated the spreading of droplets impinging on an oblique solid surface, this work found that throughout the early stages of droplet spread, the length and width of the droplet spread remained comparable. However, as time increased, and the expansion was dominated by the droplets inertia, rather than pressure, the droplet material expanded more quickly in the direction parallel to the inclination (length), than in the perpendicular direction (width). Furthermore, the ratio of length to width increased with an increase in

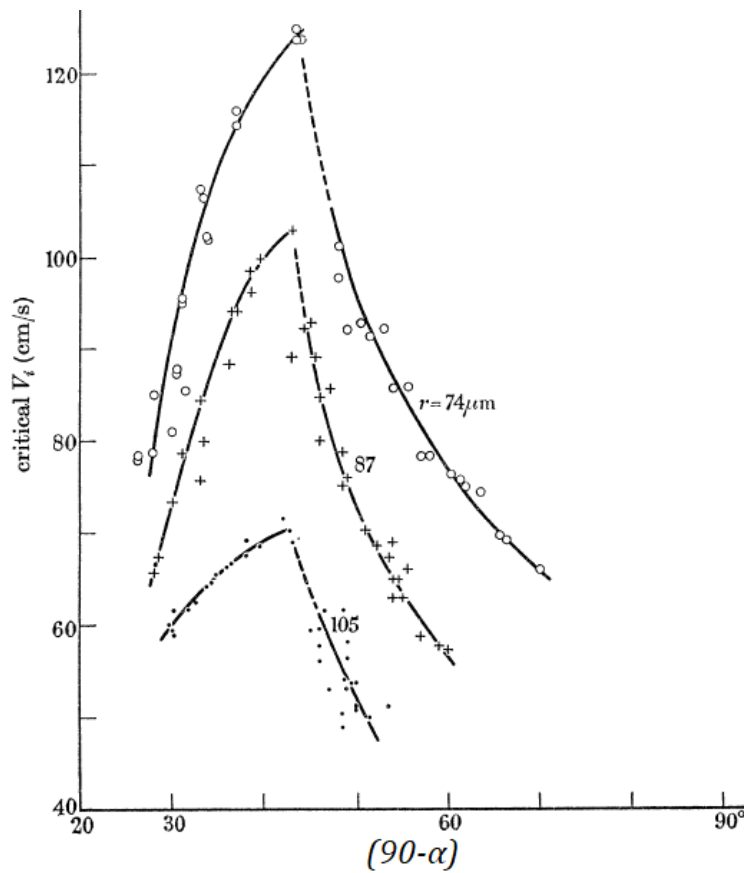


Figure 2.13: Graph from [13] Illustrating Transition region between coalescing and bouncing

plane angle.

2.3.2 Moving Substrates

Experimentation with moving substrate impingements began later than oblique impingement studies, with one of the first reported studies being in 1995, when Mundo et al. [15] investigated droplet impingements the edge of a rotating wheel with a diameter of 150mm. A sample image from this work is shown in Fig. (2.15).

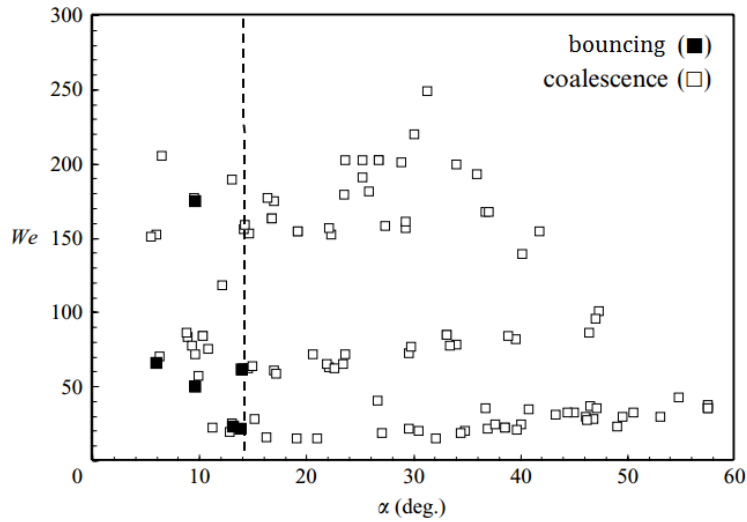


Figure 2.14: Effect of angle upon impingement outcome from Leneweit et al. [14]

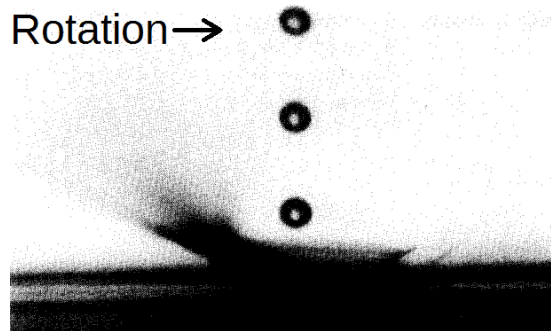


Figure 2.15: Impingement of droplet upon spinning wheel, from Mundo et al. [15]

This shows that the corona is enhanced on the upstream side by movement of the surface. This work also suggested using the normal and tangential velocities, to calculate the *effective angle* of the impingement. Furthermore, the differences in sizes of the droplets produced from the corona upstream and downstream of the impingement site were investigated, and there were only minor differences in droplet sizes between the upstream and downstream sides of the impingement. With the downstream side having a slightly smaller secondary droplet diameter when compared to the upstream side of the same impingement.

Bird et al. [16] examined the boundary between splashing and deposition for each side of a droplet impinging upon a rotating aluminium disk. This work found that with sufficient tangential velocity, it was possible to totally inhibit

splashing on the downstream side of the droplet. It was found that the boundary between symmetric and asymmetric splashing is related to the ratios of the Normal and tangential velocities as shown in Fig. (2.16). The work showed the splashing limit decreases with higher tangential velocity, as the crown is enhanced on one side due to the tangential velocity of the disk. Symmetrical splashing required a higher ratio of normal velocity to tangential velocity.

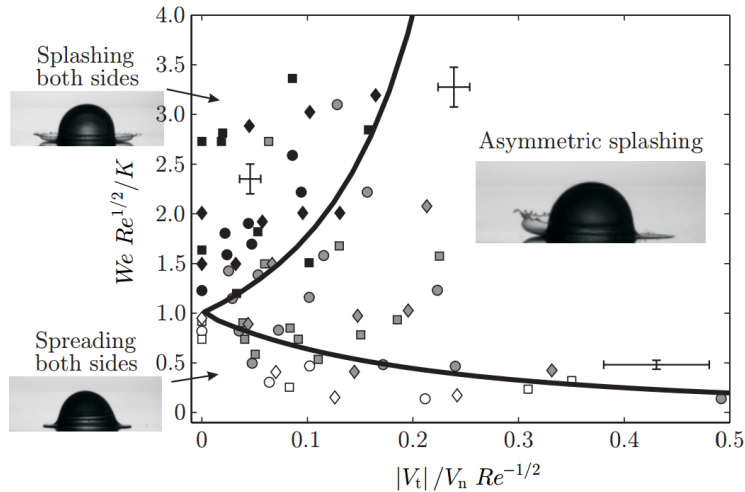


Figure 2.16: Boundaries between spreading and splashing from Bird et al. [16]. Note the asymmetric splashing region

Hao et al. [70] Investigated the impingement of a droplet on to a moving steel belt. This work was carried out in a vacuum chamber, to allow the investigation into effects of ambient pressure on the droplet impingement outcomes. This work found that the transition between coalescence and splashing was dependent on droplet speed, substrate speed, and the fluid properties. It was observed that as with previous studies the corona formed on the upstream side of the droplet was enhanced.

2.3.3 Moving Films

In 1999, Samenfink et al. [71] investigated droplet impacts onto films driven by a shearing airflow. It was found that the shearing airflow also had the effect of producing an oblique droplet impact. The authors produced probability density charts for secondary droplets at varying impingement angles, and remarked that the speed and size of secondary droplets are typically related to the speed and size of the initial droplet and the impingement angle. It is noted by Samenfink et al., that the experiments and correlations in this paper may be useful to develop a 2D CFD model, and it is implied that some initial development of

such a model has been undertaken.

Alghoul [57, 17] outlines in detail investigations into normal droplet impingement upon sub-critical moving films. It was found that the droplet impingement tended to create non-symmetrical shapes similar to those observed for oblique impingements. The crown was found to be more prominent on the upstream side, whereas jets formed inclined in the same direction as the film motion, shown in Fig. (2.17). Furthermore, it was noted that fewer secondary droplets were produced than expected for a comparable impingement on a static film, with the film movement being found to increase the boundary between coalescence and crown splashing. The transition between crown formation and crown splashing was found to show agreement with the $K_{Cossali} = 2100$ boundary from Okawa et al. [10].

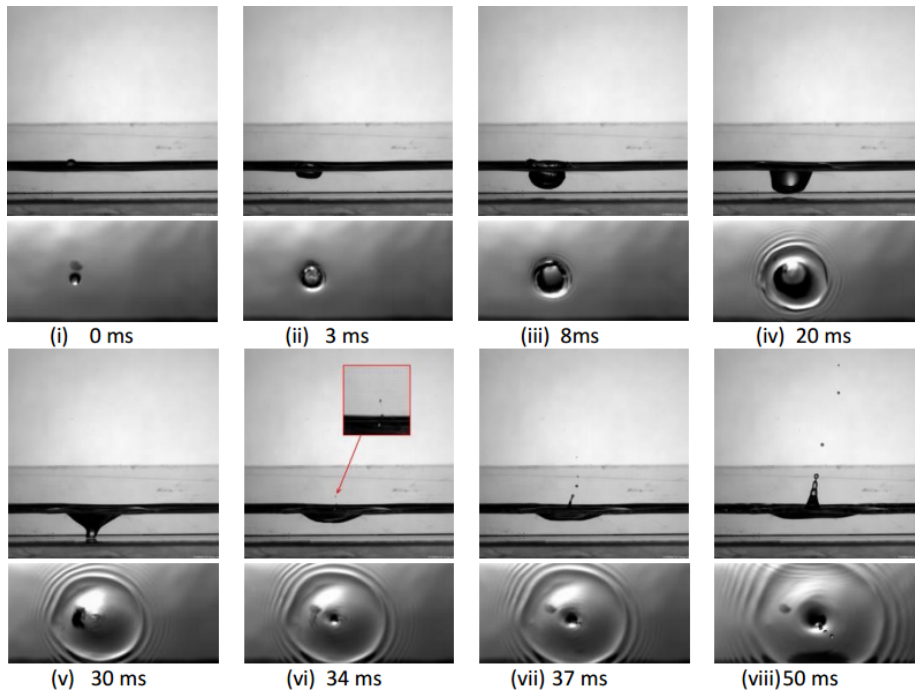


Figure 2.17: Images of droplet impingement upon horizontally moving film from Alghoul et al. [17]

Alghoul [57] includes side by side comparisons of impacts on a static and a moving film and analysis into the differences. It is noted that jet height in the case of impingement onto a static film is typically consistent with the work of Macklin and Hobbs [63]. However, in the case of a moving film, although the jet height increases with Weber number, the increase is at a significantly lower rate than for static films.

Alghoul et al. [72] also investigated oblique droplet impacts onto shear

driven films. In this paper it is noted that the droplets are deformed by the shearing airflow before impact. It is remarked that for lower levels of shear, the droplet remains roughly spherical, the transition between splashing and depositing regimes are consistent with those in published literature [10, 8]. However, for higher shearing airflow velocities, the deformation of the droplet leads to enhanced levels of splashing. With very high levels of shearing airflow, the droplet often deforms and typically breaks up before it can impinge upon the surface.

Gao et al. [45] investigated droplet impingements on moving films, and produced a splashing parameter form moving-film impingements (previously discussed in section 2.1.2) and postulated a model for crown diameter, discussed in section 2.4.4.

Casterjon et al. [18] investigated droplet impingements upon moving films inside a rotating drum, this work attempted to establish regimes for the impingement outcomes. These included a specific floating regime, dubbed *surfing*, a typical coalescence regime, and a form of partial bouncing called *lamella jetting* where there is mixing visible between the bouncing droplet and the film. This is an unusual behaviour only observed in this moving-film scenario, which may present itself for linear moving film experiments.

These regimes are shown in Fig. (2.18). It can be see that the boundary between splashing and coalescence seems only dependent on the properties of the impinging droplet, however as en coalescence and lamella jetting are observed at the same values of $WeRe^{1/2}$, the transition between these behaviours must be related to $(V_t/V_n)(1/\sqrt{Re_d})$.

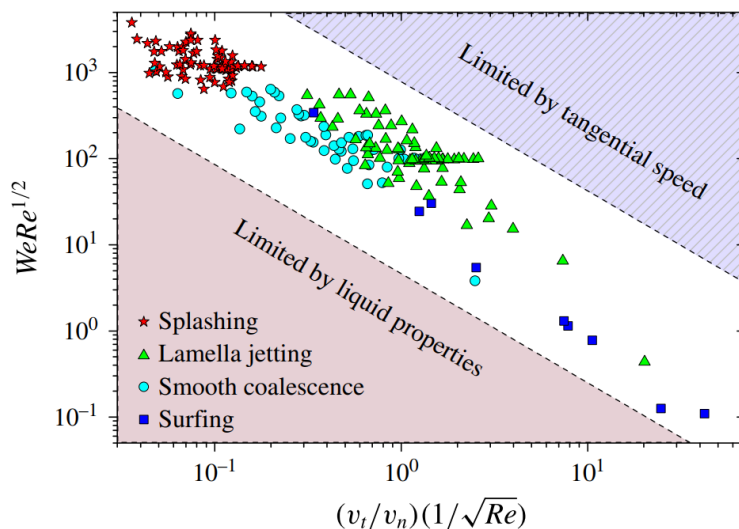


Figure 2.18: Regime map observed by Castrejon et al. [18]

To summarise, the transitions from static film experiments have not been fully validated for impingements on moving films. Some experiments have been performed for moving films which appear to suggest comparability with existing static film boundaries, yet the experimental ranges of these tests are often limited, and are therefore it cannot be conclusively determined that of static film understanding may be applied. Furthermore, behaviours have also been observed which are unique to moving film scenarios including lamella jetting [18] and the asymmetry within the crown and cavity after impingement [17]. This indicates significant scope for more work to determine if static film correlations are universally applicable. Therefore, the current experimental data is compared to $K_{Cossali}$, K_{Gao} , and K_{Huang} , including a robust statistical approach to determine the transition values in section 4.1.

2.4 Droplet Impingement Modelling

Alongside more general investigations into the splashing behaviours and regimes, many authors have attempted to relate post-impingement characteristics to the properties of the impinging droplet and substrate. The vast majority of this work is for impingements on static films, and this section details the key models which may prove applicable to moving film impingements for comparison and validation.

2.4.1 Secondary Droplets

This section examines the quantity and characteristics of the secondary droplets produced from crown splashing.

Number of Secondary Droplets

One important aspect relating to droplet-impact outcome is the number and size of secondary droplets produced by the splashing. Cossali et al. [73] determined the number of airborne drops with respect to time for a variety of impact parameters, however this work did not attempt to model the number of droplets produced. Zhang et al. [74] noted a dependence on δ on the number of secondary droplets produced, this was found to be related to the thickness and angle of the crown.

Okawa et al. [10] investigated the production of secondary droplets for a single water droplet impacting normally on a static water film and found that the number of secondary droplets (N_{sd}) could be predicted as a function of impact parameter (K) and nondimensional film thickness (δ) as follows:

$$N_{sd} = \max [4.97 \times 10^{-6}, 7.84 \times 10^{-6} \cdot \delta^{-0.3}] \cdot K^{1.8} \quad (2.13)$$

This correlation, shown against experimental data, in Fig. (2.19), was valid primarily for $\delta < 2$. When $\delta > 2$, N_{sd} the data exhibited a much higher level of scatter around the above expression.

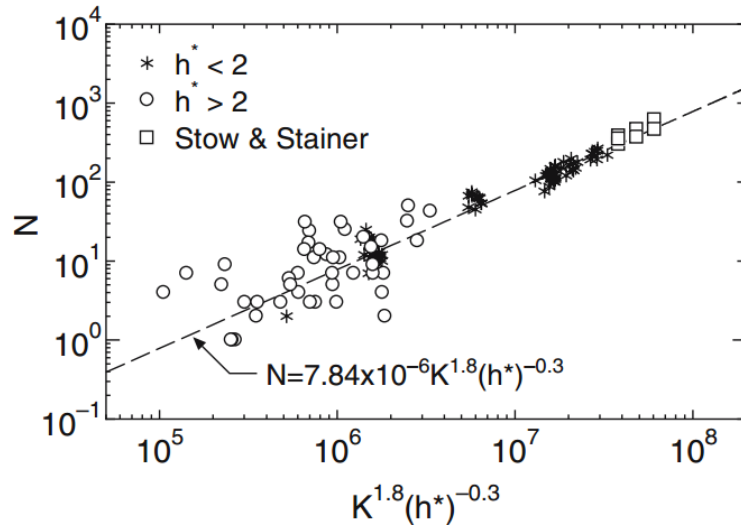


Figure 2.19: Correlation for number of secondary droplets from Okawa et al. [10]

Okawa et al. [19] investigated the impingement of droplets onto a static film with impingement angles, α , between 10° and 75° . This case is somewhat similar to near-normal impact on a moving film in that there is relative horizontal motion between the droplet and film and therefore similarities might be expected between the behaviours. Having plotted both, Okawa et al. concluded that for these non-normal impacts, using the total droplet velocity (V_d) (rather than the normal velocity (V_n)) in the calculation of $K_{Cossali}$ caused the transitions to correlate with those established for normal droplet impingement. Furthermore, it was found that the crown formation was asymmetrical in an oblique impact, with the crown tending to be larger in the same direction as the droplet was travelling.

It was also found that for values of α between 10° and 50° , the number of secondary droplets agreed with Eqn. (2.13) surprisingly well, despite the mass of secondary droplet material being lower than expected. This is illustrated in Fig. (2.20).

Peduto et al. [75] performed a study investigating aero-engine bearing chambers using a series of direct numerical simulations. This work states, based on CFD modelling of impingements in simulated bearing chambers, that

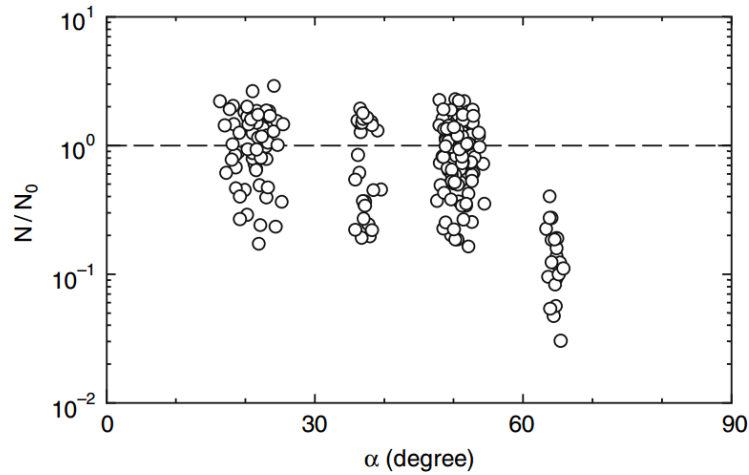


Figure 2.20: Effect of angle against number of secondary droplets (normalised by predicted values, N_0 for a normal impingement) from Okawa et al. [19]

at $\alpha > 60^\circ$ no splashing is expected. This is slightly lower than the threshold from Okawa et al. [19], whom observed no splashing when $\alpha < 70^\circ$, however this slight discrepancy can easily be attributed to the differences between a modelled bearing chamber, and a much more simplistic experimental case. Using a combined experimental and numerical modelling approach Peduto identified a relationship between the number of splashed droplets and the relevant nondimensional groups valid for the range $30^\circ < \alpha < 45^\circ$ as;

$$N = 1.208 \times 10^{-5} We Oh^{-0.25} Fr^{0.063} \frac{\delta^{-0.22}}{\Delta_{max,deep}} \alpha^2 - 51 \quad (2.14)$$

where $\Delta_{max,deep}$ is the crater depth that is found for deep water impacts and thus the term $\frac{\delta}{\Delta_{max,deep}}$ is a measure of the wall effect. Here, the droplet velocity (V_d) is used in the nondimensional groups.

Secondary Droplet properties

Stow and Hadfield [5] examined the radius and displacement of water-sheet (ie: the corona) for impingements on solid surfaces. This work found relationships between the time since impingement and the water-sheet thickness and velocity. These results are shown in shown in Fig. (2.21). This work is interesting as it produces curves in the same forms as those observed for the secondary droplet sizes and velocities in the work by Cossali et al. [20, 73].

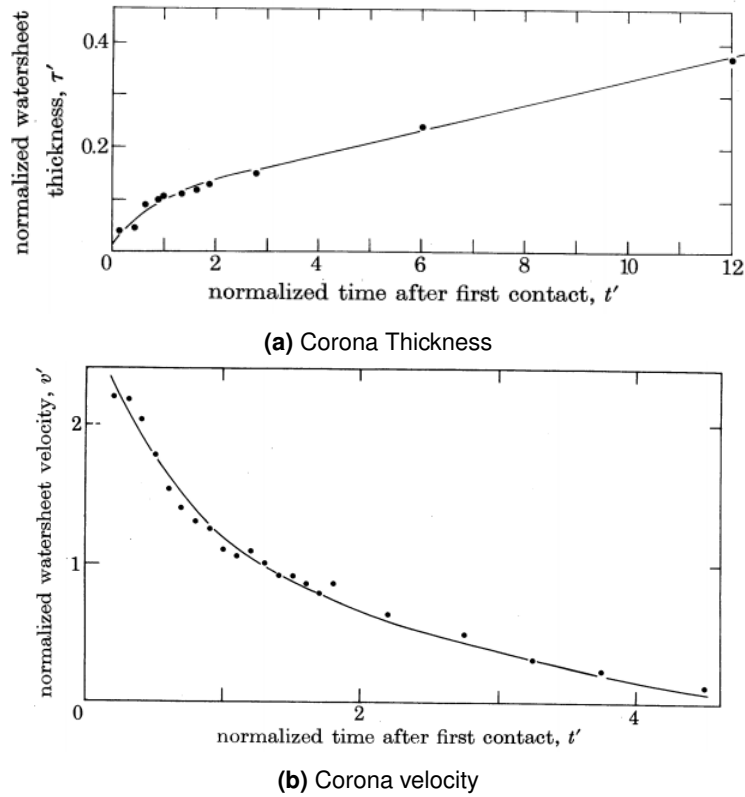


Figure 2.21: Corona properties against dimensionless time for droplets impinging on a solid surface, from Stow and Hadfield [5]

Cossali et al. [20] investigated the normalised secondary droplet size compared against the formation time, the results of this work are shown in Fig. (2.22). This shows that the secondary droplet diameter increases with time, consistent with the increase in crown thickness, and appears to be reasonably insensitive to the conditions of the impinging droplet.

This work was built upon by Cossali et al. [73], who discovered that the secondary droplet diameter could be related to the Weber number of the impinging droplet, in the form $D_{sd}/D = q\tau^m$, where q is a constant and m is related to the impinging droplet Weber number. This bears some similarities to the relationships explored later in this thesis.

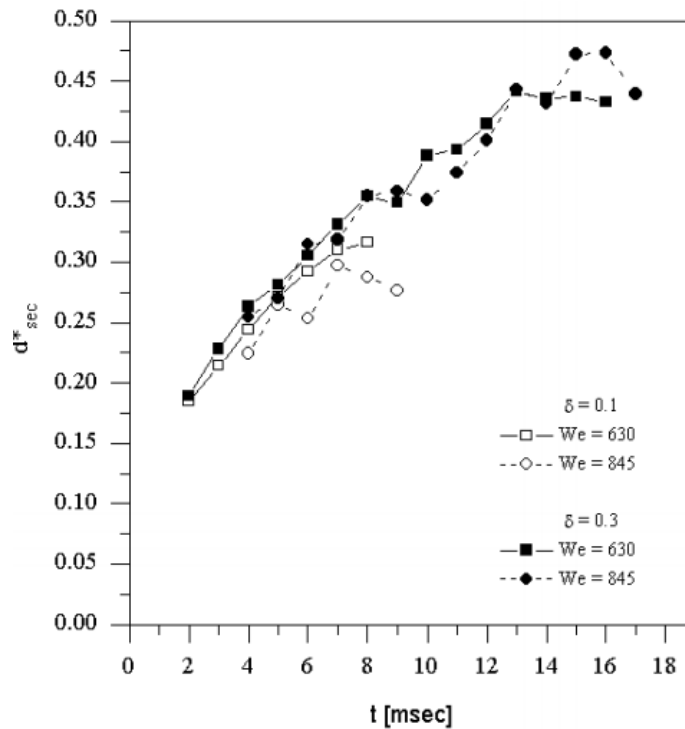


Figure 2.22: Secondary droplet diameters from Cossali et al. [20]

Within the reviewed literature, correlations and experimental data regarding secondary droplet quantities, sizes and velocities have been presented. This provides a level of understanding to which droplet production for moving film impingements can be compared. However, to the authors best knowledge, there have been no studies undertaken which consider the secondary droplet properties for impingements upon moving films. Therefore, the number of secondary droplets is compared to the relationship from Okawa et al. [19], and the properties of the secondary droplets compared to the work of Cossali et al. [73] in section 4.3.

2.4.2 Crown Morphology

This section details development models describing the size and growth of the crown, including its radius and number of ligaments and growth rate.

Crown Diameter

Yarin and Weiss [76] produced perhaps the first attempt to model crown development with time. Within this work it was suggested that the dimensionless

crown radius could be expressed in the form $R_c/D = 1.29(\tau - 1.28)^{1/2}$. The relationship was compared to experimental data from Levin and Hobbs [33], and it was observed that this relationship over-predicted compared to the experimental results. Cossali et al. [20] performed experiments which verified the square-root relationship between dimensionless crown diameter and dimensionless time.

Continuing from this, Weiss and Yarin [77] examined crown development for impingements on very thin static films. This work found that spreading of the crown could be determined in the form; $R_c/D = [C(\tau - \tau_0)]^{1/2}$, where C is a constant ($C = 24.7$), and τ_0 is the time delay between the droplet hitting the film, and the crown beginning to move ($\tau_0 = 0.020$). These parameters were determined based on curve fitting for their experimental data.

Trujillo and Lee [21] attempted to model crown formation of droplet impinging upon liquid films based on the concept of kinematic discontinuity. A relationship for the crown radius in the early stages is shown to depend on the ratio of film heights inside and outside of the cavity based on a series of ordinary differential equations. After the delay time (τ_0), the crown propagation becomes independent of upstream conditions, and is directly influenced by the film depth, due to the conservation of momentum within the crown. This relationship was compared to data from Cossali et al. [8] in Fig. (2.23) and showed to be an improvement over that derived by Weiss and Yarin [77] with a considerably reduced level of over-estimation.

Roisman et al. [41] suggested an analytically derived model for the crown radius for droplet impingements upon moving films. This is in the form:

$$R_c^* = \beta_{crown} \times \sqrt{(\tau + \tau_0)} \quad (2.15)$$

R_c^* is the dimensionless crown radius, τ is dimensionless time, h_f is the film thickness, the expansion term $\beta_{crown} = \left(\frac{3\delta}{2}\right)^{-1/4}$ and τ_0 is a dimensionless constant based on the film height, $\tau_0 = (1/\sqrt{24h_f}) - 1$. Examining this relationship, it is evident that it maintains the same square-root form as those derived by previous authors, and furthermore shows a dependence on film height, similar to that suggested by Trujillo and Lee [21]. Therefore, this form has significant scope for applications to moving-film impingements.

Gao et al. [45] investigated droplet impingements on moving films for a wide variety of conditions. It was found that upon impingement, the centre of the cavity moves downstream at the same speed as the film flow. The radius of the crown was well predicted by the analytical solution for static films from Roisman et al. [41] when β_{crown} and τ_0 were modified to represent their experimental conditions. However this was further developed into the form shown

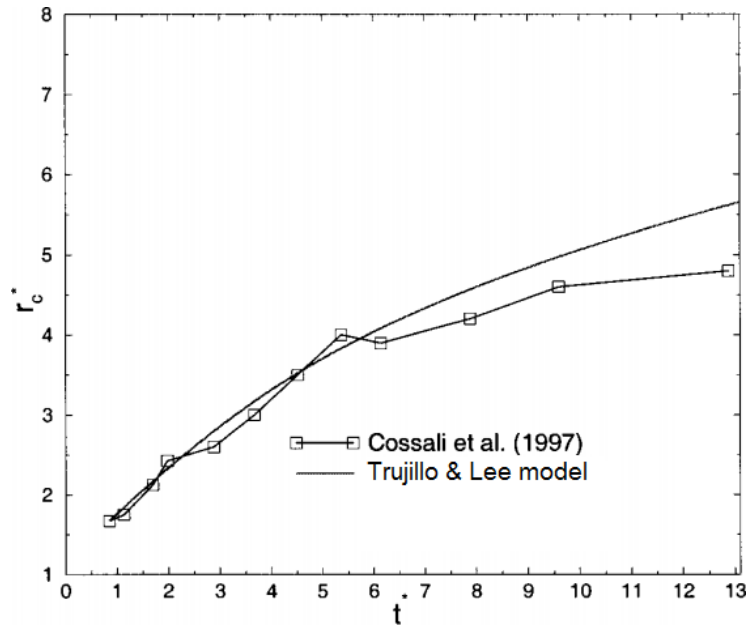


Figure 2.23: Comparison of theoretical model from Trujillo and Lee [21] against experimental data from Cossali et al. [8]

in Eqn. (2.16) to provide a higher level of accuracy in the early time stages of $0 \leq \tau \leq 6$;

$$R_c^* = \beta_{gao} \sqrt{\tau} + \frac{1}{\sqrt{6\delta}} - \left(\frac{1}{3\delta} - \frac{1}{\sqrt{6\delta}} \right)^{1/2} \tag{2.16}$$

$$\beta_{gao} = \left(\frac{2\lambda^2}{3\delta} \right)^{1/4}$$

$$\lambda = \frac{0.53}{Re_d^{-0.02} \times We_d^{0.03} \times \bar{U}_f^{-0.26} \times \delta^{0.12}}$$

where

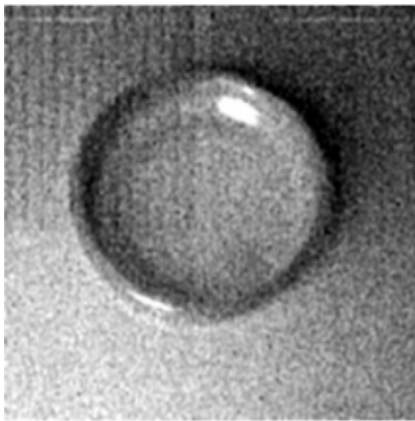
- R_c^* is the dimensionless crown radius ($\bar{r}_c = r_c/D$)
- τ is the dimensionless time ($\tau = tU/D$)
- \bar{U}_f is the velocity ratio (film velocity/droplet velocity)
- δ is the dimensionless film thickness (h_f/D)

From this we can see that there are two competing equations to describe crown evolution: the model from Roisman et al. [41], is analytically derived but has not been proven to be valid for impingements on moving films, and that from Gao et al. [45] which has been developed from moving-film experiments,

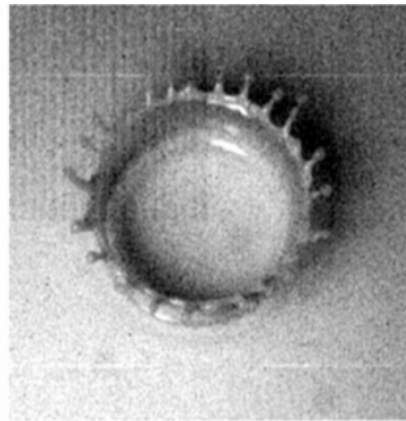
yet has not been proven valid for $\tau > 6$. These relationships are considered and compared to moving film experimental data in section 5.3.2.

2.4.3 Ligament Formation

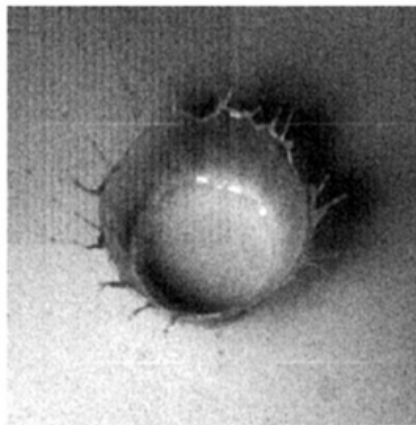
Krechetnikov & Homsy [22] argue that there are several regimes of crown splashing, *regular*, *frustration*, and *irregular*. *Regular* is where a single wavelength is observed around the crown. *Frustration* is where two or three differing wavelengths compete, and *Irregular* is where well-defined wavelengths are difficult to discern. Examples of these are shown in Fig. (2.24).



(a) Regular axisymmetric crown.



(b) Regular crown with spikes.



(c) Irregular crown.

Figure 2.24: A figure from Krechetnikov & Homsy [22], illustrating different forms of crown.

Krechetnikov & Homsy [22] also suggest that the breakup of the ejecta, i.e.;

the cause of prompt splashing, is due to the Richtmyer-Meshkov (RM) instability mechanism, which can be considered as a special case of Rayleigh-Taylor instability. The basic difference between Richtmyer-Meshkov and Rayleigh-Taylor (RT) instability is that Richtmyer-Meshkov is a result of a sudden acceleration at the interface, whereas Rayleigh-Taylor results from a constant acceleration. This allows the development of interfacial instability under Richtmyer-Meshkov conditions regardless of the direction of the acceleration relative to the interface. In the case of droplet-impingements, the fluid is destabilised as it accelerates into the surrounding air, and experiences compressibility effects. However, at later times; as the crown begins to move under its inertia and decelerate due to viscous losses, it is suggested that Rayleigh-Taylor instability begins to dominate the production of droplets and ligaments on the crown.

This is supported by Zhang et al. [23] who compared the inverse bond number of the crown, against time from the impingement. ($Bo^{-1} = \sqrt{(\sigma/\rho a_r)} \cdot r_0^{-2}$), where: a_r is the acceleration seen at the rim, r_0 is the radius of the crown's rim. When the inverse Bond number is greater than one, it is stated that the effect of acceleration can be considered unimportant relative to the capillary effects. When we consider Fig. (2.25), it is evident that at early times, when prompt splashing is observed, the inverse bond number is less than one, and indicates a dependence on the acceleration of the crown rim. Conversely, at later times, the inverse Bond number is larger than one, indicating that late-time breakup is dominated by capillary effects. This supports the suggestion from Krechetnikov & Homey [22] that there are two differing instability mechanisms for crown breakup.

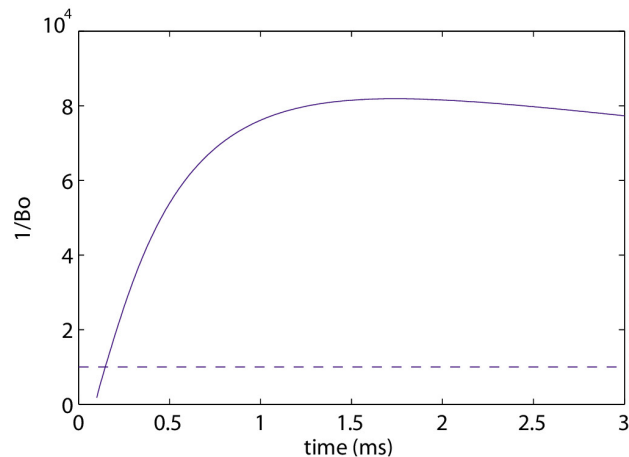


Figure 2.25: Calculation of the inverse Bond number of the crown rim against time, from Zhang et al [23]

Zhang et al. [23], showed that the wavelength of the bulges in the crown rim at later times were predicted accurately by models of Rayleigh-Plateau instabilities. Furthermore, using Fig. (2.26) it was possible to show that the predicted wavelength of Rayleigh-Taylor instability is significantly greater than what was experimentally observed, thus disputing the conclusions of Krechetnikov & Homsy [22] and Bremond et al. [78], that Rayleigh-Taylor instability was responsible for the formation of ligaments on the crown at late time-scales.

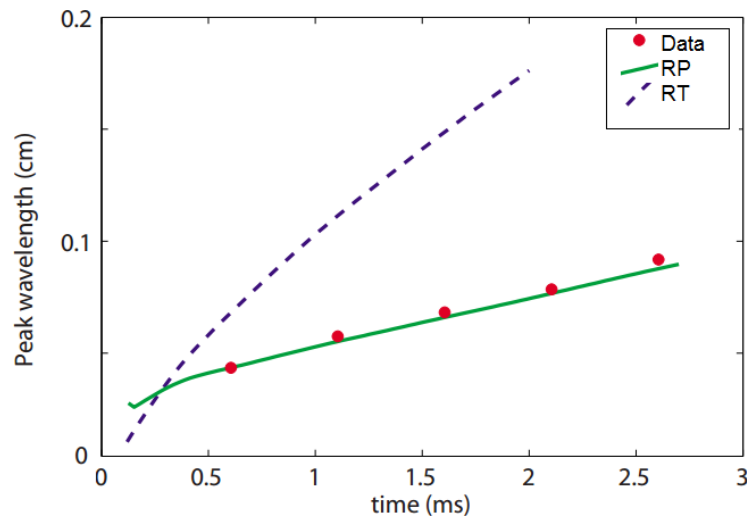


Figure 2.26: Comparison of the peak wavelength against predicted values from Rayleigh-Plateau (RP) instability and Rayleigh-Taylor (RT) instability from Zhang et al. [23]

From the literature, it seems apparent that crown splashing may be the result of differing instability mechanisms, depending upon the time at which droplets are produced. This is examined later in section 4.2, where a qualitative analysis into the formation of droplets is discussed, and related back to these mechanisms.

2.4.4 Crater Development Modelling

This section outlines attempts in literature to model properties of subsurface craters, this includes the width, length diameter and depth of the craters, for both deep pool, and thin films. Of these scenarios, deep pool has had the most investigation, with thin and moving films being investigated the least.

Crater Depth

Although the above surface phenomena of droplet impacts have been well studied, there have been fewer attempts to model the behaviour of the craters formed during impacts. In this section the nomenclature shown in Fig. (2.27) will be used to differentiate between directions of the crater and cavity spread relative to the flow.

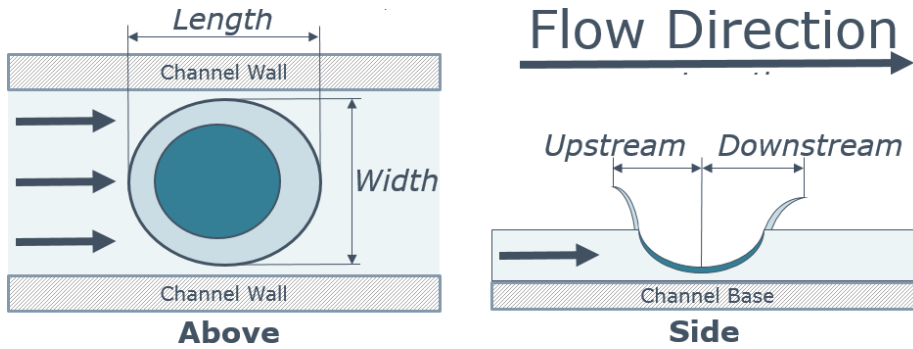


Figure 2.27: A sketch of a crater establishing nomenclature of the cavity and crown

One early model is that created by Engel [79]. This paper took experimental data and used it to develop a model to determine the variation of crater depth with time. When compared to experimental data, the model has a strong correlation with the experimental data initially. However, at later time periods, a distinct deviation between the data and the predicted depths is observed.

More recent attempts have used dimensionless parameters to characterise crater development. Those commonly used are the dimensionless time ($\tau = tU/D$), by [80, 25, 24] dimensionless crater width ($\Omega = width/D$) [25, 24] and dimensionless crater depth ($\Delta = y_{cr}/D$) [25, 24, 54].

Berberovic et al. [25] derived the asymptotic solution in Eqn. (2.17) for droplet impingement on deep pools. This defines a curve in dimensionless time which crater growth tends towards, at high values of We_d . However, as this model, does not account for surface tension or viscosity parameters, and therefore is of limited use for lower energy impingements.

$$\bar{y}_{cr} = 2^{-4/5}(5\tau - 6)^{2/5}, \tau > 2 \tag{2.17}$$

where:

- y_{cr} is the crater penetration depth (mm)
- τ is the dimensionless time (tU/D)

Berberovic et al. [25] also determined that for the initial stages of crater propagation the crater was roughly hemispherical, and the dimensionless depth (Δ) can be expressed as Eqn. (2.18).

$$\Delta \propto 0.44\tau \tag{2.18}$$

Following on from Berberovic et al. [25], Bisighini et al. [24] developed a model for crater depth for deep film impingements based on a series of ordinary differential equations, which adapted to various droplet parameters. This technique is relatively computationally inexpensive compared to previously used CFD techniques used by Berberovic. The model centred around Eqns. (2.19, 2.20), and was shown in the paper to adapt to various conditions and show a good fit with experimental depth data as shown in Fig. (2.28).

$$\ddot{\alpha}_c = \frac{3\dot{\alpha}_c^2}{2\alpha_c} - \frac{2}{\alpha_c^2 We} - \frac{1}{Fr} \frac{\zeta}{\alpha_c} + \frac{7}{4} \frac{\zeta^2}{\alpha_c} \tag{2.19}$$

$$\ddot{\zeta} = -\frac{3\dot{\alpha}_c \dot{\zeta}}{\alpha_c} - \frac{9}{2} \frac{\zeta^2}{\alpha_c} - \frac{2}{Fr} \tag{2.20}$$

$$\Delta = \alpha + \zeta \tag{2.21}$$

where:

- α_c is the diameter
- ζ is the offset
- We is the Weber number of the droplet
- Fr is the Froude number of the droplet

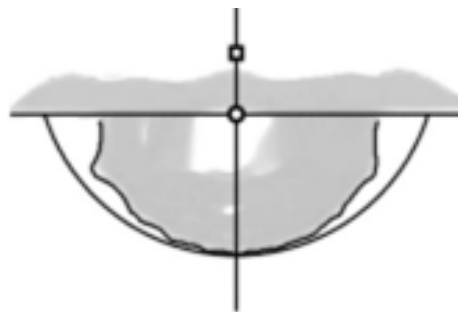


Figure 2.28: A figure from Bisighini et al. [24], comparing the model in Eqns. (2.19 - 2.20) to experimental data

Within the field of thin-film modelling, accurate models for depth are somewhat harder to find. Although it has been shown [26] that the early stages of

cavity propagation are like those for thicker films, the rate of expansion of cavity depth begins to decrease as the cavity approaches the wall. This is not accounted for in existing deep-film models.

Crater Width

Berberovic et al. [25] attempted to model thin film impacts upon thin films, using Volume of Fluid (VOF) CFD. A comparison between the experimental results, and CFD simulations is shown in Fig. (2.29) for $\delta = 2$. Unfortunately, no correlations were derived from these experiments.

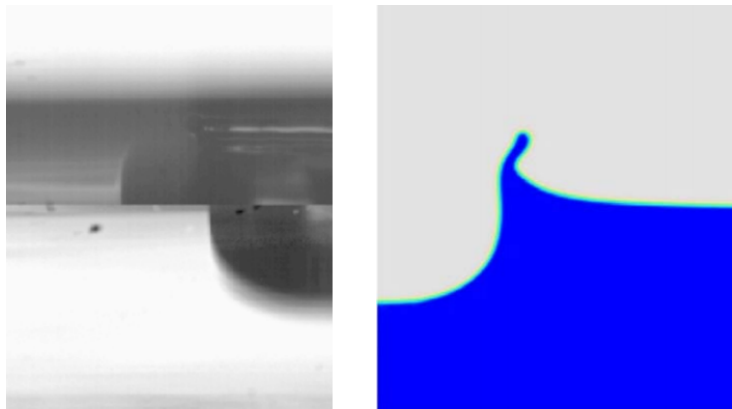


Figure 2.29: Comparison of a VOF CFD model for impingements upon thin films with a CFD model from Berberovic et al. [25]

Bisighini et al. [24] developed a model for crater width which is defined in Eqn. (2.22). This could define the dimensionless crater width (Ω), that is, the width divided by droplet diameter, at a given point in dimensionless time. This method relied on the constant α_0 , which was found by fitting to their data using the least mean square method. This accurately predicted for their experimental conditions, but may not hold valid outside of their examined experimental range.

$$\Omega = 2\sqrt{(\alpha_0 + 0.17\tau)^2 - (0.27\tau - \alpha_0)^2} \tag{2.22}$$

where:

- α_0 is constant (found as 0.77 using the least mean squares method)
- τ is the dimensionless time (tU/D)

Roisman et al. [42] produced a model that related the dimensionless cavity width as a function of We_d , Fr_d , τ , and δ . This model is shown to adapt to a wide variety of droplet and film conditions with a high level of accuracy. The model of Roisman et al. [42] is shown by Eqn. (2.23)

$$\Omega = \sqrt{\beta(\tau - \tau_0) - f(\tau - \tau_0)} \quad (2.23)$$

where:

$$f(\tau - \tau_0) = \left(\frac{2\delta}{\Omega_{max} \cdot We_d} + \frac{4}{We_d} + \frac{\delta^2}{Fr_D} \right) (\tau - \tau_0)^2 / \delta,$$

$$\Omega_{max} = \frac{\beta}{2} \sqrt{\frac{\delta}{G}} - \frac{\delta}{G \cdot We_d},$$

$$G = \frac{4}{We_d} + \frac{\delta^2}{Fr_D}$$

Roisman et al. theorised that τ_0 and β were dependent on the dimensionless film height δ , as shown in Eqn. (2.24).

$$\tau_0 = 0.5\delta^{1.7}; \quad \beta_{Roisman} = 0.62\delta^{0.33} \quad (2.24)$$

Van Hinsberg et al. [43] also used this model and noting that there was a dependency of β on We_d proposed a modified approach for obtaining β as shown in Eqn. (2.25). For clarity, to differentiate in this work each β term, each has been subscripted with the name of the primary author of the paper from which it is derived.

$$\beta_{Hinsberg} = \left(\frac{22.3}{We_d} + 0.5 \right) \cdot \delta^{-0.33} \quad (2.25)$$

Furthermore, Hann et al. [26] investigated droplet impingements upon a static film of $\delta = 0.43$. This paper concludes that for the initial stages of impact, the crater depth propagates as per Eqn. (2.18) proposed by Berberovic et al. [25] before the decelerating as the cavity approaches the wall. This work then correlates with the width model from Roisman et al. [42], and proposes an improved derivation of β in the form:

$$\beta_{Hann} = 3.1 (We_d \cdot \delta)^{-0.37} \quad (2.26)$$

Considering the literature, it is evident that many models have been created to characterise the key parameters of droplet impinging onto static films. However, in some cases, such as Eqn. (2.23), there are multiple variations of the model that require further work. Furthermore, few of these models have been shown to be valid for impingements onto moving films. Therefore, in section 5.2.2, cavity dynamics for moving film impingements are investigated and compared to the existing model from Roisman et al. [42], with the aim of understanding which, if any of the forms of β can be used to characterise cavity

dynamics for moving film impingements.

2.4.5 Droplet Spreading and Mixing

The spreading and mixing of the droplet and film has significant implications for heat transfer. Hann et al. [26] looked at the thickness of the droplet material for impingements on static films using the BB-LIF technique. This technique (discussed in section 2.6.2) allowed the spread and thickness of the droplet material within a cavity to be measured. Fig. (2.30) shows experimental data of the droplet spreading, at various values of dimensionless time ($\tau = 1, 1.5, 2, 3,$ and 5) for $We_d = 283$. The experimental data is compared with the correlation from Roisman et al. [6] for droplet spreading on a solid surface. The experimental data points show a strong correlation with the dotted line of the model, especially for the later stages of the impingement ($\tau = 1.5 - 5$). This shows that post-impingement dynamics can be remarkably similar to pre-existing static film knowledge, and suggests that previous understanding and theory regarding heat transfer between droplets and solid walls may be applied to droplet-film impingements.

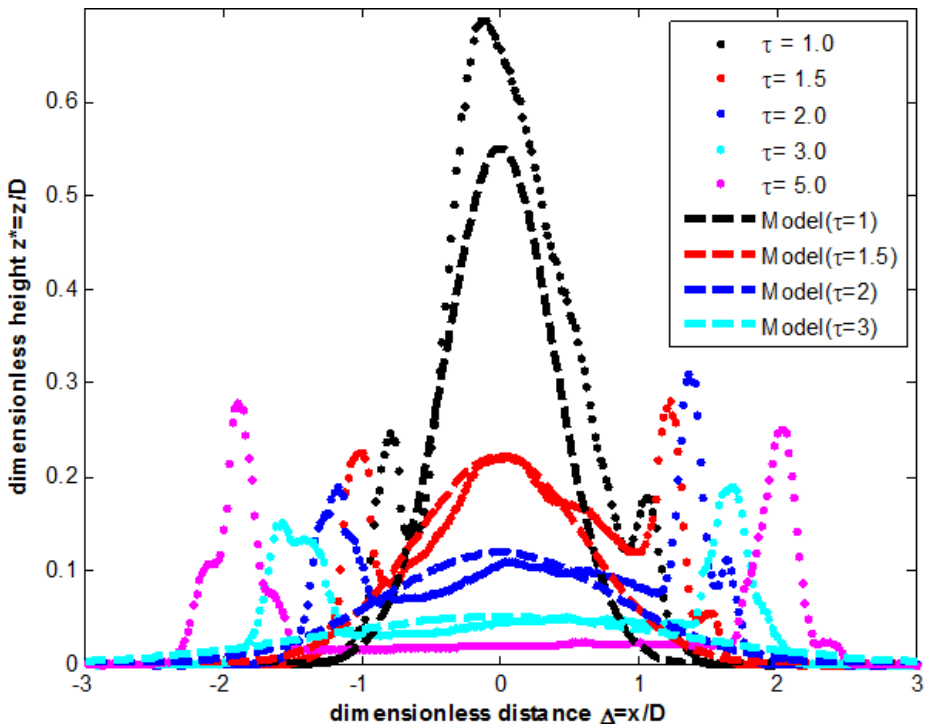


Figure 2.30: A figure from Hann et al. [26] comparing experimental data about droplet deformation from a droplet-film interaction to the model from Roisman et al. [6] (Eqn. (2.12))

Thoraval et al. [27] investigated droplet impingements on deep pools and showed that some splashing behaviours can be attributed to Von Karman vorticity within the advancing crown. Furthermore, computational simulations suggested that when Re_d is high, this vorticity could spread along the droplet-film interface, as shown in Fig. (2.31) and facilitate mixing between the droplet and film. This analysis is also supported by experimental work by Castrejon-Pita et al. [28], who observed vorticity at the droplet-film interface through shadow graph imaging, and by seeding the droplet with fluorescein dye. An example of this behaviour is shown in Fig. (2.32).



Figure 2.31: Von Karman Vorticity predicted computationally at the droplet-film interface by Thoraval et al. [27]

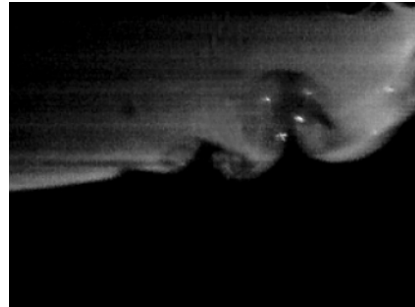


Figure 2.32: Von Karman Vorticity observed at the droplet-film interface by Castrejon-Pita et al. [28]

Agbaglah et al. [29] further investigated vorticity at the droplet-film interface using high-speed X-ray imaging. This work provided additional experimental corroboration of the findings of Thoraval et al. [27] Furthermore, regions of We_d and Re_d were proposed within which vorticity was observed, shown in Fig. (2.33). Agbaglah et al. also suggested that the initiation of vortex shedding is better predicted by the Capillary number of the droplet (Ca_d) as shown by the boundary on the black line, which represents $Ca_d = 0.2$, and gives a reasonable approximation of the transition to vorticity.

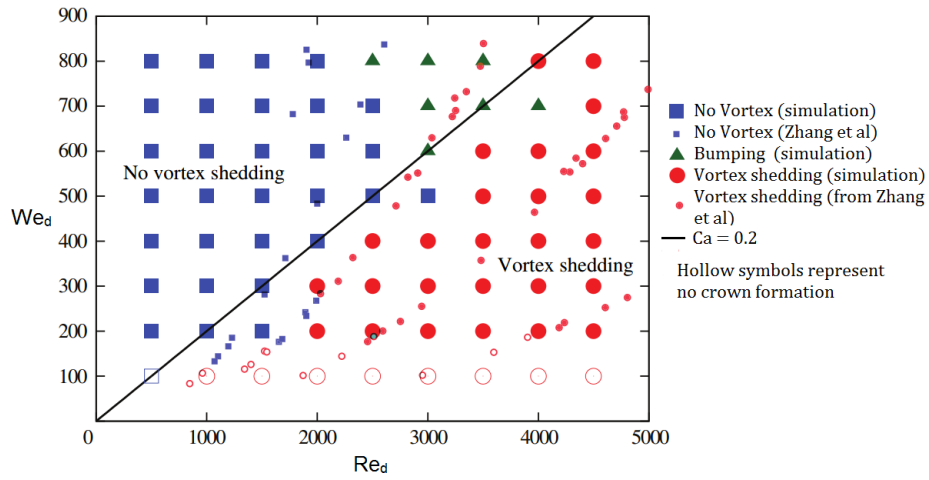


Figure 2.33: Vorticity map from Agbaglah et al. [29], showing computational simulations, and experimental data from Zhang et al. [30], showing the transition to vorticity around $Ca = 0.2$

Yang et al. [81] undertook computational modelling of droplet material spreading within the crater using Smooth Particle Hydrodynamics (SPH). Their study showed that when the cavity was at its largest size, the droplet material was spread as a thin layer within the cavity. This implies that whilst the model form Roisman et al. [6] provides accurate modelling of the spread within the cavity for early time-scales, once the cavity is in the self-similar inertial regime, spread of the droplet fluid may be dictated by the expansion of the cavity.

Whilst some attempts have been made to understand the spreading and mixing for static film impingements, it is not certain how these behaviours will be affected by impinging upon a moving film. Therefore, there is scope to establish the validity of these models for static film impingements. As a follow-up to the work of Hann et al. [44], section 5.2.3 describes a comparison of droplet spreading for an impingement upon a moving film, making comparisons to the relationship from Roisman et al [6]. Furthermore, a preliminary investigation is undertaken to determine if the BB-LIF technique can be used to visualise the mixing between the droplet and film.

2.5 Summary of Droplet Impingement Literature

As shown, there is a large variety of experimental and computational work within the field of droplet impingement. However, most of this work is focussed on either solid substrate or static film impingements, whilst the amount of experimental work for moving films is comparatively small. The need for the research presented in this thesis is therefore clearly established.

It has been shown that within the literature, there is little understanding of secondary droplets produced from impingements on static films, and no research considering secondary droplet properties for impingements on moving films. Furthermore, although asymmetry has been observed within the crown and crater, there is minimal understanding of the controlling factors for this behaviour, and no attempts have been made to model how this affects the development. Therefore, these topics will be considered in the course of this thesis.

The work presented in Chapter 4 examines the necessary conditions for droplet production, the physical mechanisms of droplet production, and the quantity, size and velocity of those droplets which are produced. Comparisons are made specifically to the observations and transition regimens and correlations from Cossali et al. [20, 8, 73], Hunag and Zhang [46], Okawa et al. [10, 19] Gao et al. [45], and breakup theories by Agbaglah et al. [29], Krechetnikov & Homsy [22], and Zhang et al. [23] as discussed in sections 2.1 - 2.4.1

Chapter 5 focuses on the cavity development, spread of droplet material within the cavity and, the development of the crown upstream, downstream and across the flow. Specific comparisons are made to the models produced by Gao et al. [45], Roisman et al. [41, 42, 6], Van Hinsberg et al. [43] and Hann et al. [44], as discussed in sections 2.4.2 - 2.4.5.

2.6 Data Acquisition Methods

This section briefly outlines the various methodologies of data acquisition used historically, from early experiments to more contemporary investigations. The primary focus of these sections is on the approaches and techniques valid for application to droplet-moving film experiments. The techniques and equipment used within literature are evaluated, and conclusions drawn regarding which methods are most appropriate to the current work.

2.6.1 Visual Data Acquisition Methods

The first use of optical techniques in the field of droplet impingement can be traced back over 100 years. Worthington [31] investigated droplet impingements using spark photography, where a bright spark was used to ‘burn’ the image at that split-second temporarily onto observers’ retina, to create a timeline of a droplet impact. Although by contemporary standards the methodology of Worthington may seem crude, the illustrations within the paper show many of the characteristics observed in later papers. (Discussed in Section 2.1.)

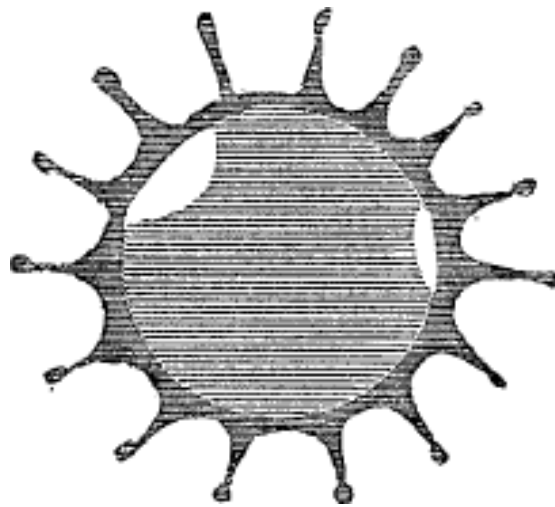


Figure 2.34: Illustration of a droplet impact made by Worthington [31] in 1876

Image Capture

The next major advancement in the use of cameras to capture images of droplet impacts. In 1908 Worthington [4] used a film camera to record images. However, the stand-out use of this technique is by Edgerton [32], who in

1938 used an electronic flash to capture images of droplets of milk as shown in Fig. (2.35). The pictures obtained are very clear, with minimal motion blur. However, this technology could still capture single frames, and so it was less useful as it is difficult to create a timeline of the events after a droplet impingement without many experimental repeats.

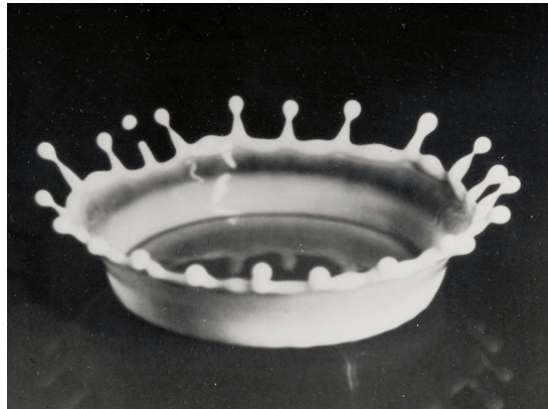


Figure 2.35: Photograph of a droplet impact taken by Edgerton in 1936 [32]

In 1971 Levin and Hobbs [33] used a 5000 Hz film camera, with a powerful spotlight to illuminate their droplets, to ensure there is enough light hitting the film during the short exposure time. Using this method, the authors were able to capture clear images of droplet impingements, and furthermore were able to create a composite image. The images are relatively clear, as shown by a sample image in Fig. (2.36). However, one of the disadvantages of using a film high speed camera, is that the high frame rate uses a large amount of single use film. This in turn makes the process relatively expensive and laborious, resulting in only a small range of conditions being investigated within this work.

The next big development in image capture was in the widespread availability of digital cameras. Since these require no single-use film, the cost of operation is significantly reduced. Furthermore, the data can be manipulated on a computer, making it much easier to manipulate and process the images. In 1995, Yarin and Weiss [34] used a digital video camera which was charge coupled to an array of LEDs. The LED array is linked to the camera shutter to ensure the sensor has enough light to create a clear image.

Yarin and Weiss [76] also used long exposures on a film camera with a strobe light, to generate single pictures, with a snapshot from several points in time overlaid. Although this method is low cost, the fact that the images overlap make it difficult to fully understand how the splash develops, as shown in Fig. (2.37).

In recent years, high-speed digital photography has further improved, cam-

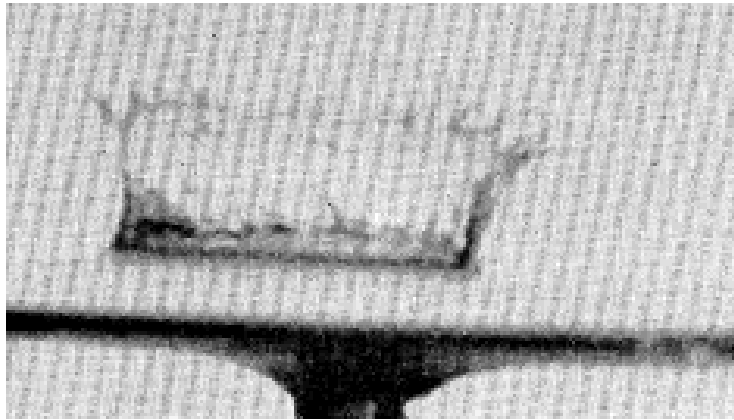


Figure 2.36: Still from the film obtained by Levin and Hobbs [33]

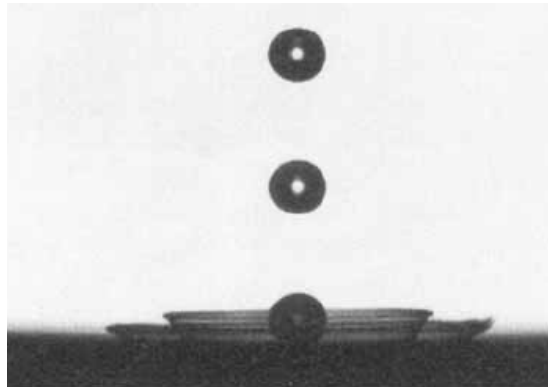


Figure 2.37: A long exposure image obtained by Yarin and Weiss [34] using a strobe light

eras such as the Phantom v12.1 are now capable of frame rates of 6000Hz, whilst still maintaining image resolutions of 1 mega-pixel. Furthermore, sensor technology has significantly improved, allowing a higher range of colours and intensities, and lower noise levels than earlier cameras.

More recently, the advent of Pulsed-LED spotlights has allowed even higher levels of illumination with high-powered LEDs. The light source can produce much higher illumination levels, whilst generating significantly less heat than a conventional halogen lamp. Furthermore, these LED's can accept a TTL pulse from the camera, allowing an increase in light output during the exposure, and the light to be turned off when the shutter is closed. This means the light intensity whilst the shutter is open can be higher, whilst keeping the temperatures within tolerable levels.

Summary

The work presented in this thesis uses the most advanced technology available. This consists of a digital high-speed camera, and high intensity lighting. Two high-speed cameras have been utilised, a Phantom V12.01, and an IDT Vision OS3. Both cameras can achieve frame rates in excess of 6000Hz at 1 mega-pixel image resolution, and are suitable for use recording droplet impingements. Illumination is provided by either high-powered halogen lights, or by pulsed-LED lights as described in section 3.3.

2.6.2 Laser Induced Fluorescence (LIF)

Alongside conventional high-speed imaging, Laser Induced Fluorescence (LIF) is commonly used to investigate behaviours of fluids across a broad range of single and multi-phase experimental applications, including droplet impingement scenarios [44, 28, 82]. This section discusses the usage of Laser Induced Fluorescence for the investigation of droplet and film interactions, before finally examining the Brightness Based-LIF technique, which allows determination of the fluid thickness based on the illumination intensity.

One of the earliest usages of LIF to visualise fluid flows was by Hewitt and Nicholls [83], who used laser fluorescence to visualise flows of disturbance waves in annular dispersed flows. Their approach used the relative intensities of the peaks and troughs of the waves to visualise propagation of these waves along the surface, and paved the way for later techniques investigating film thicknesses.

Another common use of LIF is to investigate the dispersal and mixing of fluids, Hoffman et al. [84] investigated the mixing of liquids using Rhodamine B fluorescent dye and high-speed camera. This work showed that with the correct dyes and optical techniques, it is entirely possible to record the movement of a very small amount of fluid doped with fluorescent dye.

Similarly, Castrejon-Pita et al. [28] use LIF to investigate the mixing at the droplet-film interface, and confirmed the existence of Von Karman vortex shedding causing mixing between the droplet and film as shown previously in Fig. (2.32).

More recent development of LIF has focused on developing the ability to determine film heights from the illumination intensity. Alekseenko et al. [35] developed on the observations of Hewitt and Nicholls, and developed the Brightness Based Laser Induced Fluorescence (BB-LIF) technique. This allowed conversion of image intensities for fluids of constant concentration into height data. These experiments used a film containing Rhodamine-6G fluorescent dye in

water at a concentration of 30 mg/l , this dye was illuminated using a light sheet from a 532 nm , 50 mW laser. A low pass filter was placed in front of the camera with a cut off wavelength of 550 nm , this allowed only the $550 - 600 \text{ nm}$ fluorescence from the dye to be detected by the camera, without any interference from the laser. Depth Measurement was achieved by determining the absorption co-

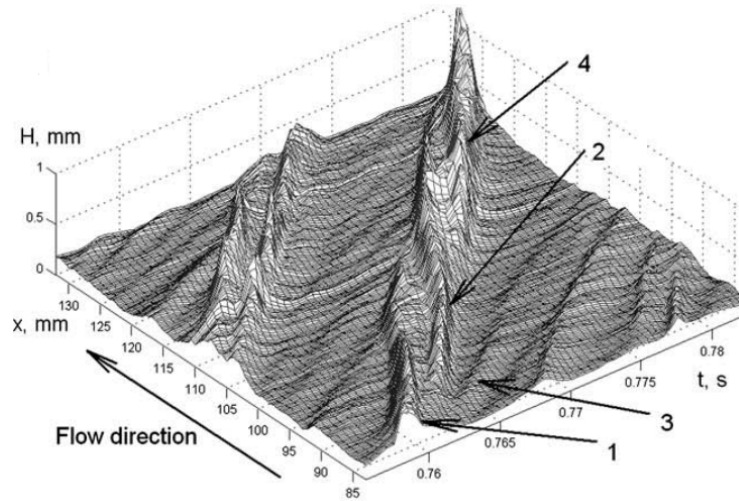


Figure 2.38: Depth profile obtained using BB-LIF from Alekseenko et al. [35], numbered labels indicate features in the film referenced in the original literature.

efficient of the fluid using known depths of the solution. For the experimental tests, the film heights could then be calculated based on the Beer-Lambert law, in the form shown in Eqn. (2.27) and discussed in much greater detail in section 3.5. This technique allowed measurements to be taken with high temporal and spatial resolution in two dimensions for a row of pixels. Fig. (2.38) shows a typical dataset from this work, a 3D graph of time, pixel location, and film height.

$$\frac{J(x,y) - D(x,y)}{C(x,y)} = [1 - \exp^{\alpha_{abs} \cdot h(x,y)}] \cdot [1 + k_{refl} \cdot \exp^{-\alpha_{abs} \cdot h(x,y)}] \quad (2.27)$$

where:

- $J(x,y)$ is the image in intensity values
- $D(x,y)$ is the dark level of the camera
- $C(x,y)$ is an illumination correction matrix
- α_{abs} is the absorption coefficient of the dye

- $h_{(x,y)}$ is the film height
- k_{refl} is the coefficient of reflection at the air-water interface

Cherdantsev et al. [36] used a similar technique using a rectangular duct, with a film loaded by a shearing airflow. The most obvious variation from the methods used by Alekseenko et al. [35, 85] is that rather than using a light sheet to illuminate a plane, this work used a wide, dispersed beam, to gather brightness information inside a two-dimensional array. By using a two-dimensional data array, it is possible to resolve the experimental region in three dimensions as shown in the false-coloured image in Fig. (2.39). The technique gave a spatial resolution of 0.125 mm , with sampling rate of 10 kHz . This work used Rhodamine 6G fluorescent dye at a concentration of 15 mg/l .

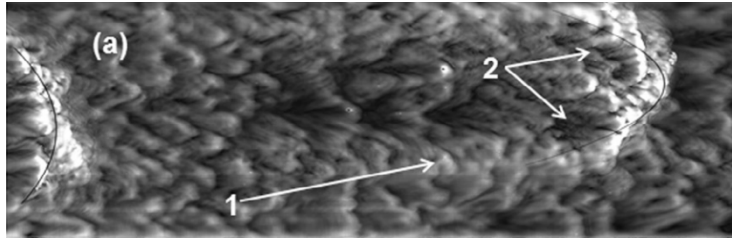


Figure 2.39: Depth profile obtained using BB-LIF from Cherdantsev et al. [36]

Hann et al. [26] used the technique from Cherdantsev et al. [36] to investigate impingements of water droplets upon thin static films, with a dimensionless film thickness of $\delta = 0.43$. In the course of the experiments, a single droplet size was used, with five different droplet heights. There were three dye regimes, (i) both the droplet and film were dyed (ii) the droplet only was dyed (iii) the film only was dyed. This shows that the BB-LIF technique can be applied to droplet impingements with high levels of success. An example image is shown in Fig. (2.40) showing a crater, and its deviation from the nominal film thickness, nondimensionalised against the droplet diameter. Discussion of the findings of this study was presented in sections 2.4.4 and 2.4.5.

Summary

Considering the capability of this technique to resolve films in three dimensions, with high spatial and temporal resolutions, it was decided to use LIF and BB-LIF for this investigation. Specifically, the technique was used to investigate spreading of the droplet, and development of the crown and cavity after the impingement. The data processing for this work is discussed in section 3.5, and the results are presented in chapter 5.

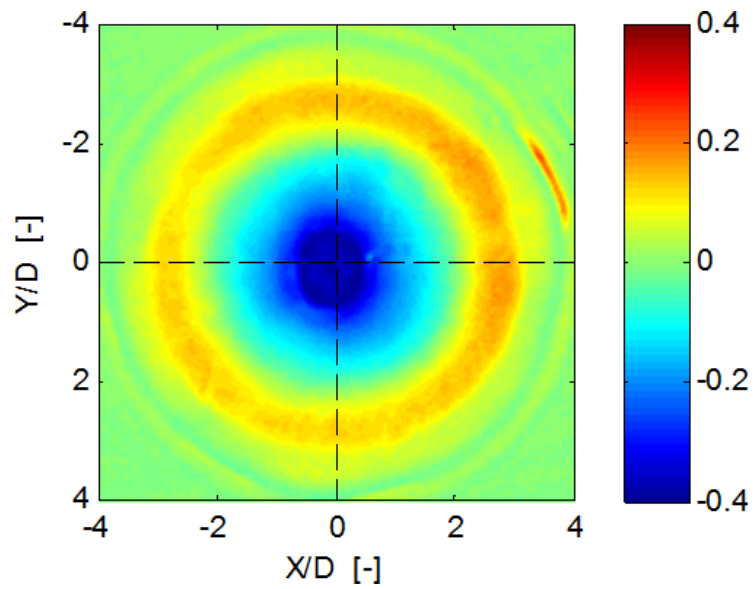


Figure 2.40: Depth profile obtained using BB-LIF from Hann et al. [26]

2.7 Droplet Generation Methods

This section reviews the various methods of creating droplets, and the sizes of produced by each method. Previous studies deriving correlations for droplets impinging on static films have predominantly focused on droplets in the range of $D = 2 - 4 \text{ mm}$. However previous works within the University of Nottingham [86] has shown that droplets entering the bearing chamber are in the range of $0.051 - 0.235 \text{ mm}$.

The simplest form of a droplet generator is to push fluid through a hypodermic needle. This typically creates droplets in the $2 - 5 \text{ mm}$ range [17, 8, 31, 87, 88]. These droplets usually detached from the hypodermic needle either due the influence of gravity, or a pressure pulse.

Other possibilities for droplet generation include vibrating orifice droplet generators, such as those proposed by Schneider & Hendricks [89], these can be used to create droplets in the range of $160 - 230 \mu\text{m}$ [88]. Another option is described by Le. [90] who explains that using ink jet printer cartridges, it was possible to create droplets of $13 \mu\text{m}$ using the cartridges from a HP Desk Jet 890C, and to create $15 \mu\text{m}$ droplets using the cartridge from an Epson Color Stylus 800.

Considering that previous study within the University of Nottingham has indicated that droplets in the range $1.5 - 2.3 \text{ mm}$ form 73% of the mass entering the chamber, and that most correlations for static film literature are in the range of $2 - 5 \text{ mm}$. It was decided to select droplet sizes of 2 mm and 3 mm , created using a needle system. This gave a level of comparability with both previous literature, whilst still maintaining an aspect of applicability to bearing conditions. The specific system and characterisation of the produced droplets are discussed in section 3.1.2

2.8 Data Processing and Analysis

Within literature, several methods have been used to analyse the data, this section outlines the methodologies used to enhance images and to detect and characterise features within them.

The key challenges are:

- Illumination correction and contrast adjustment
- Impinging droplet detection
- Height conversion for BB-LIF images
- Feature detection for BB-LIF processing

2.8.1 Image Post-processing and Enhancement

Vernon [37] discussed methods to filter out background noise, spatially calibrate the camera, and to determine droplet sizes.

In order to attain the best results, Vernon decided to remove the background from the image using a Gaussian filter. This created a blurred version of the image being analysed. If the blurred image was then subtracted from the original image, this has the effect of removing the background. Results of this process can be seen in Figure 2.41. As is evident, there is a significant reduction in background noise and the droplets are much easier to discern from the background. This increase in uniformity and contrast made the image easier to process by reducing the probability of any false positive results.

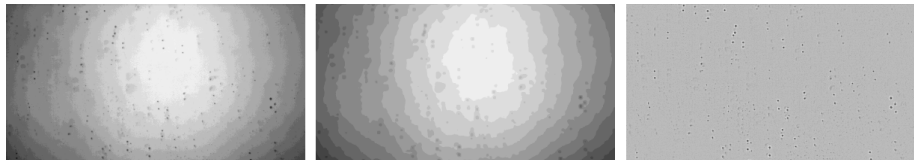


Figure 2.41: The background removal process used by Vernon [37]. The left image is the original image captured by the camera. The central image is the same, but with a Gaussian filter applied. The right image is the result when the blurred image is subtracted from the original, showing the droplets in the image.

This process bears a resemblance to the lighting correction detailed on the Mathworks website [38] however instead of using Gaussian blur, this method uses a morphological structuring element to create a blurred background image. Which is then subtracted from the original image in the same manner as used by Vernon. It is possible to tweak the performance of this function by changing the shape of the structuring element. Overall both methods produce an acceptable result, removing the background and smoothing out lighting discrepancies.

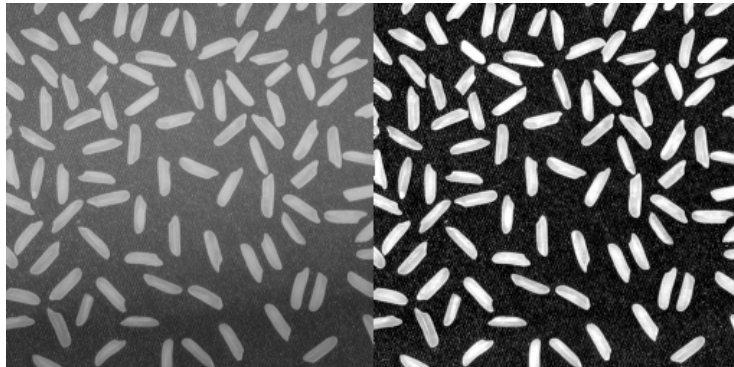


Figure 2.42: The original image is shown on the left, and the right show it after lighting correction and contrast adjustment. [91]

Mathworks [92] and The San Diego State University [93] detail a method of de-blurring images using a Weiner filter. This technique is shown to be able to reduce the blur of an image by significant amounts. However, in this process some noise is introduced into the image. Therefore, although it is possible to restore blurred images, it is much more desirable to avoid motion blur when capturing the images initially. This technique may however be useful for smaller secondary droplets where the reduced radius reduces the threshold at which motion blur occurs.

2.8.2 Spatial Calibration

To spatially calibrate the lens, Vernon used an object of known size, and then found the number of pixels that object occupied. From this it was possible to determine a spatial constant, which made it possible to calculate the size of objects with unknown dimensions from the frame.

2.8.3 Droplet Detection

It is desirable to detect the droplet and key regions in images, this can be done using a variety of methods, those that detect regions, and those that detect edges.

Edge Detection

Vernon used morphological operations to determine the approximate area of the drop. To do this the 'fill holes' function in LabView was used. However, it is remarked that this function is proprietary, and no details are given on its methodology. Nevertheless, it created a bright region, extending across the

diameter of the droplet. Vernon then used the 'particle analysis' function. This identified the dimensions of the region, and selected the larger, as this represents the diameter of the droplet. Finally, the diameters could be converted from pixels to real measurements using the spatial constant calculated above.

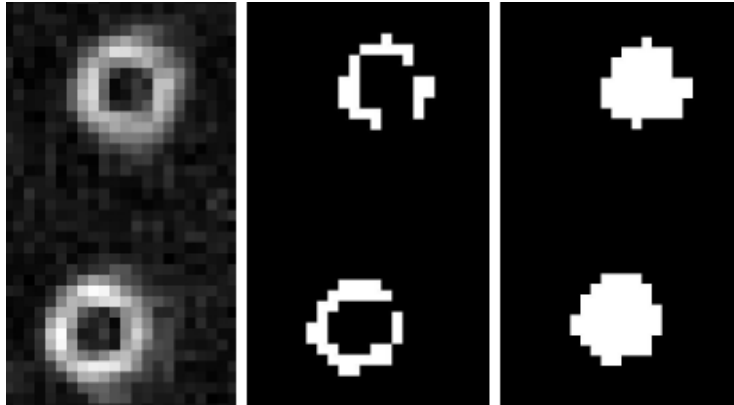


Figure 2.43: The edge detection, thresholding and morphology from Vernon [37]. The left image shows the result of the edge detection software. The central image shows the thresholding used to determine if the droplet is in focus and the right image shows the result of the hole filling.

Mathworks details a method to detect cells using the `edge` function [91]. This function is a simple way to apply a variety of complex edge detection kernels to an image. The available kernels are comparable to those used by Vernon in LabView. Alghoul [57] compares the effects of several edge detection kernels on a pendant drop. Using *Sobel* and *Prewitt* kernels it is determined that increase in sensitivity required to get a continuous outline of the pendant drop, also causes 'undesired edge pixels' to be detected. The *Roberts* kernel showed similar undesired pixels, however these were typically concentrated around the drop profile. Alghoul notes that the best results were obtained from the *Canny* and *Laplacian of Gaussian* operators. By tuning the threshold, it was possible for Alghoul to generate a continuous, one pixel thick, outline of the pendant drop with no unwanted edge pixels. The detected area of the droplets is also stated to vary by a maximum of $60 \mu m$ using *Thresholding*, *Canny* and *Laplacian of Gaussian*.

Region Detection

Mathworks [38] details a procedure using the thresholding technique in Matlab. This makes it possible to detect regions of an image. However, this is a very primitive method for region detection. Alghoul [57] notes that whilst global

thresholding struggled to accurately detect a pendant droplet due to its transparency, it was possible to detect an edge region.

Vernon details a method for determining the ideal setting of the ‘threshold’ comparing the results with varying threshold levels, and determining an ideal level for each set of conditions. However, Alghoul [57] used the inbuilt MATLAB function *imthresh* was used to provide an initial threshold, which was then tuned manually to improve the results.

Matlab also provides an inbuilt circle finding function [39] which is designed specifically to find circles in images, this is achieved by implementing the circular Hough transform in the method proposed by Yuen et al. [94]. This method is preferred as it is highly robust, even where there is varying illumination or high levels of noise. Sample images using this technique are shown in Fig. (2.44). From this image it is evident that the methodology can detect circular objects with ease, even when they are in a non-enhanced grayscale image.

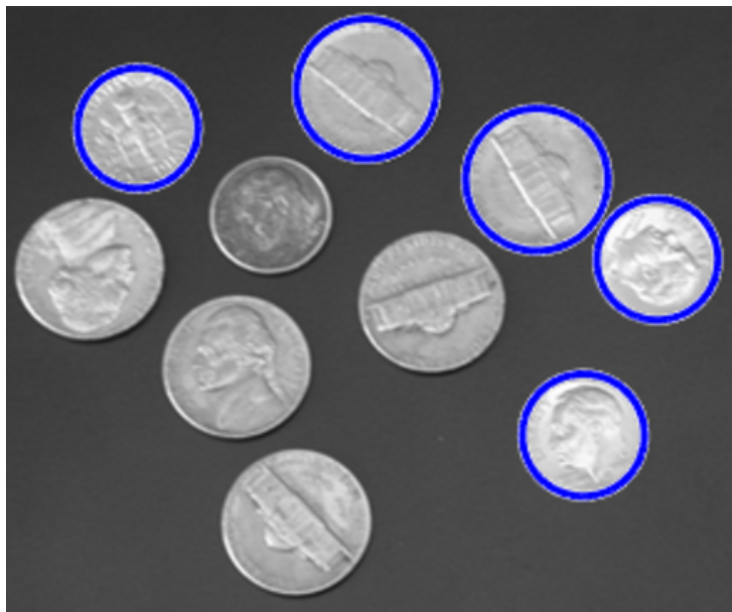


Figure 2.44: Circled detected using the *imfindcircles* function from MATLAB literature [39]

LIF Data Processing

Hann et al. [44] outline the steps of processing LIF images to obtain height data. Firstly, the absorption coefficient (α_{abs}) is calculated by comparing the image intensity to known thicknesses of dyed fluid. By plotting the image intensities against the fluid thickness, it is possible to fit Eqn. (2.27) and calculate the

dye absorption coefficient α_{abs} . The next step was to correct for the dark-level of the camera. This dark-level image was acquired by taking an image from the camera with the lens cap obscuring the lens, and the base values of the pixels could then be cancelled out.

Whilst a volumetric light-sheet, like that used by Hess et al. [95] was used to illuminate images, it was necessary to correct for unevenness in the illumination using a correction matrix. This was created by averaging each pixel across the time domain, and then calculating the relative brightnesses across the image. This does unfortunately reduce the Z-axis resolution in darker areas of the image, as fewer pixel intensity values are used to represent the same depth of film.

The images were then converted to height data, this was achieved by re-arranging Eqn. (2.27) and applying across each image. The absorption coefficient was the experimental calculated value, and the reflection coefficient at the air water interface was presumed to be the standard value of air and water of 0.02. This assumption does present a weakness within the technique, as this assumption will deteriorate for highly curved regions of the film.

Chapter 3

Experimental Investigation

Within this chapter, the details of the inclined plane experimental testing rig are discussed. This generates a moving film onto which droplets are targeted. Previous works [8, 19, 42, 41] have shown that post-impingement behaviours are dependent on the properties of the target film. Therefore, a number experimental and theoretical methods were applied to determine the film depth and bulk velocity across the entire range of film conditions.

This chapter includes a description of the testing rig, characterisation of the flow along the channel, and set up of the cameras, lights and laser system. Finally, the applied methods of data acquisition and analysis are discussed in section 3.4. This includes positioning and set up of the high-speed cameras and illumination sources, and an overview of the automated data processing. When manual data processing techniques have been used, the heuristics used to draw distinctions between different behaviours are provided.

3.1 Experimental Apparatus

The inclined-plane testing rig was designed to provide an environment closer to aero-engine bearing chambers than explored by static film research. This was achieved by introducing movement to the film, and impinging the droplets at non-normal impingement angles to the film, whilst still maintaining comparability to existing static-film literature. This section includes an overview of the experimental rig and droplet generation methods.

3.1.1 Test Rig Summary

A schematic for the apparatus used in these experiments is outlined in Fig. (3.1), and a photograph is provided in Fig. (3.2). This consisted of a water tank,

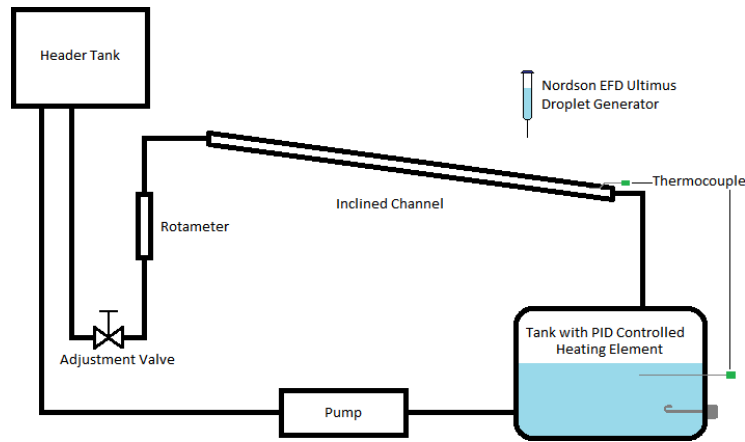


Figure 3.1: Diagram showing the Testing Rig

fitted with a PID controlled heating element, consisting of a Watlow EZ Zone controller and a Redring 33324601, to ensure a constant water temperature (typically $30\text{ }^{\circ}\text{C}$). This was then pumped using a Nocchi Pura Dom pump to a header tank, a constant pressure head was achieved by using an overflow, to return water to the main tank. This provided a constant flow down the channel, and reduced back-pressure (and therefore wear) on the pump compared to using a control valve directly.

After exiting the header tank, water flowed through a valve controlling the flow, and an RS components 441-4879 Liquid Flow Indicator to measure the flow rate, with a stated accuracy of $\pm 2\%$, and a repeatability value of $\pm 1\%$ [96]. Finally, the water flowed down the channel, and returned to the tank. Accuracy of the flow meter was verified using a bucket of known volume and a stopwatch, the flow control mechanism is shown in Fig. (3.3). The channel was 50 mm wide, and had walls 25 mm high and was fabricated from clear perspex. As discussed in section 3.2, the impingement site was placed 1.4 m from the beginning of the channel, to allow the flow to become fully developed at the point of impingement.

Inclination of the channel was adjusted using a vertical slot with an adjustment rod, as shown in Fig.(3.4). Through basic trigonometry it was possible to determine the angle based on the length of the adjustment rod, and the distance between the adjustment slot and the pivot point. Increments of 10° were marked on the adjustment rod, to allow easy and repeatable adjustments. The PID control system measured the temperature of the water in the channel using a thermocouple, and adjusted the power to the heating element to ensure the water temperature was constant. For safety purposes, a second thermocouple measured the temperature of the water in the tank, and was designed to cut

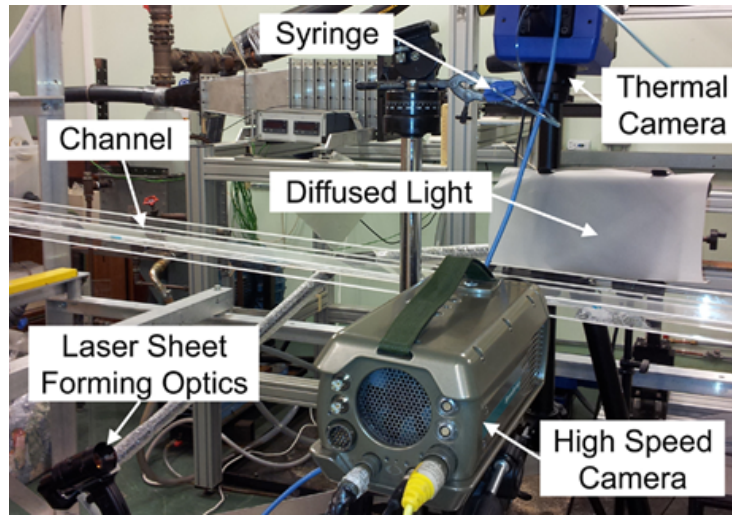


Figure 3.2: Photograph of the testing rig, showing the inclined channel, cameras and laser optics.

power to the element if tank temperature exceeded $40\text{ }^{\circ}\text{C}$.

3.1.2 Droplet Generation

Most static film literature has focused on droplets within the range of $1.5\text{ mm} < D < 3.5\text{ mm}$ range. Therefore, to maintain comparability with previous studies, droplets of 2 mm and 3 mm were generated. Previous work within the Gas Turbine Transmission Research Centre (G2TRC) [86] has shown that droplets formed from a geometry and regime of interest are within the range of $0.051 - 0.235\text{ mm}$, with droplets in the range of $1.5 - 2.3\text{ mm}$ forming 73% of the mass of fluid. Whilst future work is anticipated to consider the smaller droplets within an aeroengine oil system, these sizes were selected to give both bearing relevant sizes, and sizes comparable to static film literature. Finally, use of these larger droplet sizes provided ease of visualisation using commonly available photographic lenses.

These droplets were produced using a syringe and 0.3 mm and 0.71 mm diameter dispenser tips, as shown in Figx. (3.5, 3.6). Droplets were formed by blowing gently into the attached pipe, and allowing a droplet to form and detach. Accuracy values for this method are discussed in section 3.4.2.

3.1.3 Flow Calibration

Although the rig is fitted with a RS 441-4879 Liquid Flow Indicator, it was deemed prudent to check if this was accurately displaying the flow rates. Ex-

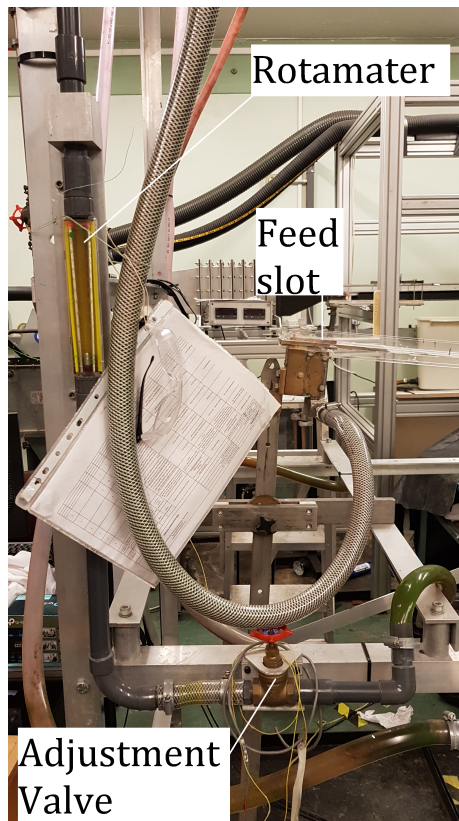


Figure 3.3: Photograph of the testing rig, showing the adjustment mechanism in detail

periments were undertaken using a 'bucket and stopwatch' technique. A bucket of known volume was placed under the outlet of the channel, with a stopwatch used to record the time taken for the bucket to fill up. From the time taken, and the bucket volume, it was then possible to determine the flow rate. Results from the experiments are shown in Tbl. (3.1), where percentage difference is calculated as:

$$\%Difference = | IndicatedFlow - MeanflowRate | \times 100 / IndicatedFlowRate$$

Considering the results, it is evident that the rotameter is accurate for most measurements, with an average variation of 2.74%, which can be attributed to parallax errors and human reaction times. Therefore, the indicated flow values will be used in further calculations.

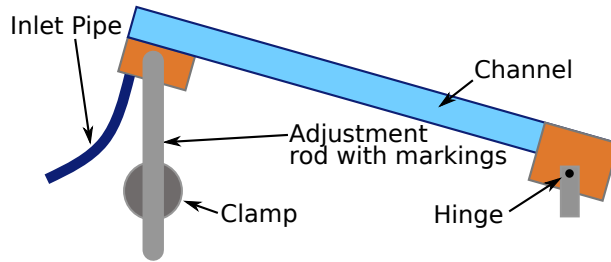


Figure 3.4: Schematic of the Channel elevation system

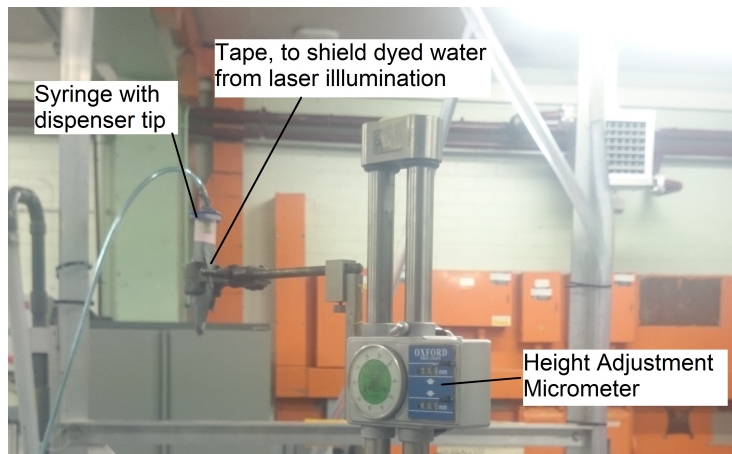


Figure 3.5: Photograph of the syringe height adjustment system

3.1.4 Experimental Parameter Range

The range of experimental parameters considered within the course of this thesis are summarised in Tbl. (3.2).

3.2 Channel Characterisation

As many authors [8, 15, 10, 41, 42, 44] have observed, post impingement behaviours are influenced by the properties of the target film, it was deemed necessary to understand the nature of the film flowing along the channel. The key parameters required included the flow regime (laminar, turbulent), if the flow is fully developed, and the film height and bulk velocity.

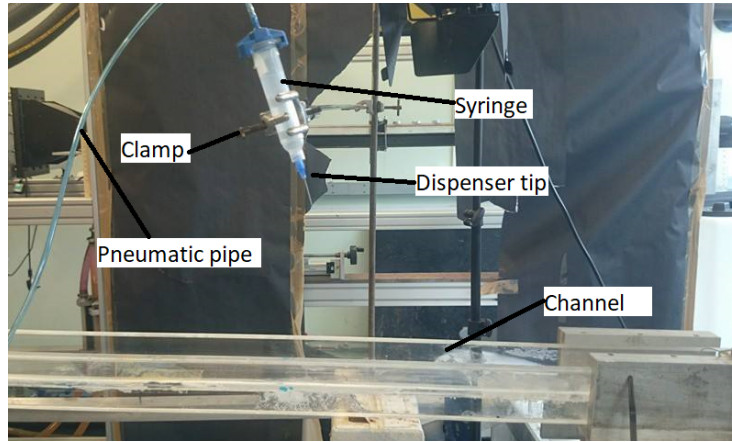


Figure 3.6: Photograph of the droplet generation system from preliminary testing.

Table 3.1: Calibration of the Flowmeter

Indicated Flow Rate (l/m)	Bucket Volume (l)	Fill Time (s)			Mean Time (s)	Mean Flow Rate (l/m)	% Diff-erance
		1	2	3			
4	20	290.6	292.6	291.6	291.6	4.115	2.88
6	20	190.4	195.6	193.3	193.1	6.21	3.57
8	20	150.1	151.5	147.4	149.67	8.02	0.22
10	20	114.3	114.2	115.2	114.57	10.47	4.74
12	20	98.1	97.2	98	97.77	12.27	2.28

3.2.1 Empirical data

This subsection details the empirical data collection processes for flow down the channel, including the experimental processes, determination of flow development, film heights, and key dimensionless parameters.

Experimental Set-up

On the experimental rig the fluid emerges from a slot 50 mm wide, with a height of 2 mm. The channel is made from clear perspex, measuring 50 mm wide, 1.4 m long and with sidewalls 25 mm high. It can be angled at various inclinations between 10° and 40° to the horizontal. The fluid is fed from a header tank fitted with a weir, this allows a constant pressure head, and hence creates a more repeatable film, whilst simultaneously reducing the risk of damage to the pump. Flow from the header tank was controlled through combination of a

Table 3.2: Experimental Parameters

Parameter	Nominal Values	Calculated Values
D (mm)	2, 3	2.05, 2.98
Release height (mm)	100 - 700	
V_d (m/s)		1.25 - 3.4
α	10°, 20°, 30°, 40°	
Flowrate (lpm)	4, 6, 8, 10, 12	
Film height (mm)		0.82 - 2.79
<i>Dimensionless Parameters</i>		
We_d		75 - 854
Re_d		4100 - 13700
Oh_d		0.00208 - 0.00250
Re_f		6300 - 18000
Fr_f		6.3 - 13.5
δ		0.24 - 1.36

rotameter and a gate valve to measure and adjust the flow rate.

To measure the film height, a Keyence LT-9030M Laser Displacement sensor was used, this allows determination of the various layers within the channel (air, perspex, water, air) utilising the confocal principle patented by Minsky [40] and shown in Fig. (3.7). This allowed determination of the distances to the peaks in the signal, caused by the interfaces between the layers. Modern systems using this technique have been shown to be able to determine the thickness of transparent, multi-layered objects with a high degree of accuracy [97].

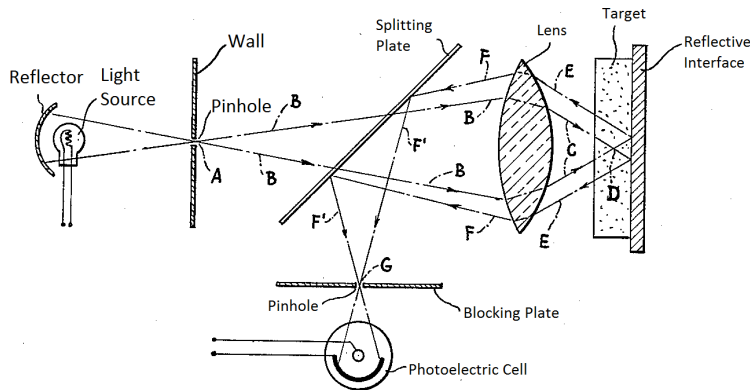


Figure 3.7: Illustration of the confocal laser displacement technique from the original Minsky patent [40] (annotated)

The sensor was placed below the channel perpendicular to it as shown in Figs. (3.8, 3.9). The sensor was mounted upon a micrometer which allowed it to move perpendicular to the channel base determine the interfaces between air, perspex, and water.

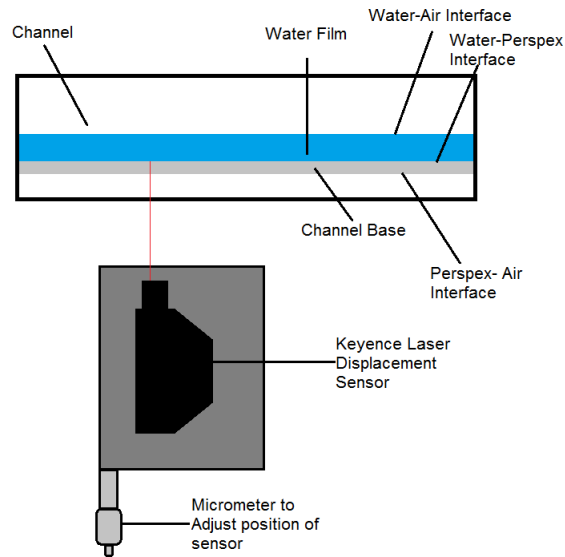


Figure 3.8: Experimental apparatus for determination of film thickness

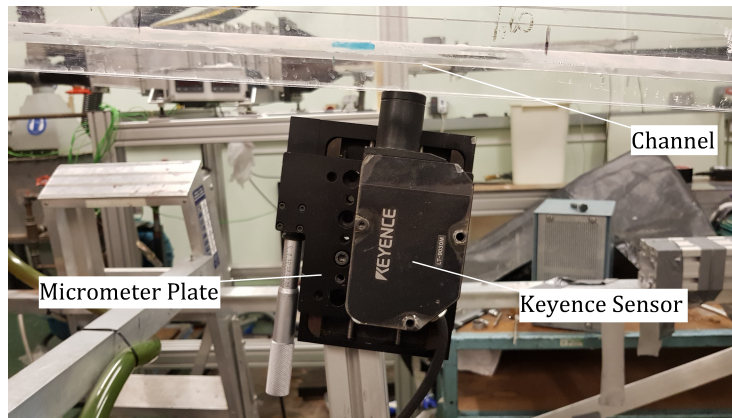
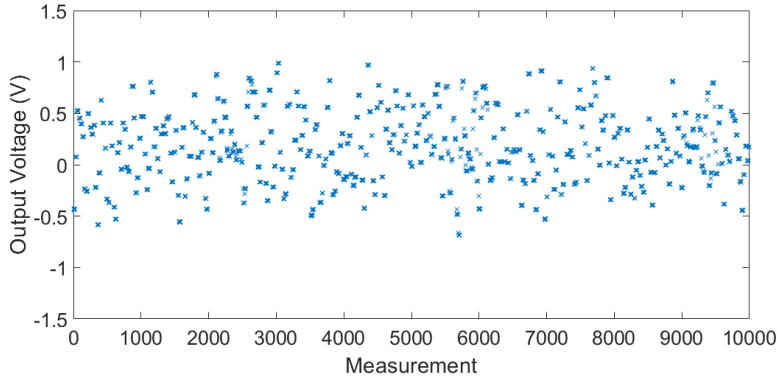


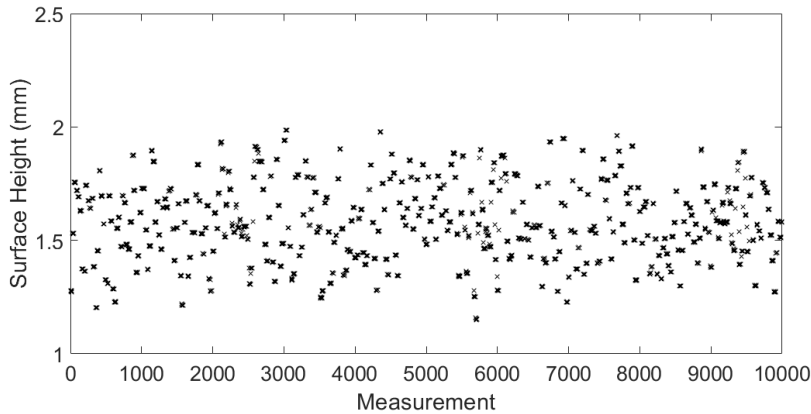
Figure 3.9: Photo of experimental apparatus for determination of film thickness

The sensor was initially placed in the lowest position, and raised until the first interface was observed. Due to the geometry of the channel, this interface was between the air and perspex at the underside of the channel and unimportant for the film measurements. The sensor was then further raised until the interface between the Perspex and water was found. A reading was taken from the micrometer, and a series of measurements were taken from the

Keyence sensor and the average was added to the micrometer reading. This process was repeated at the air/water interface at the surface of the film, and the average of two distances to determine a film thickness.



(a) Surface voltage reading from the Keyence LT-9030M confocal laser displacement sensor, showing a typical signal profile.



(b) Surface profile taken from the Keyence LT-9030M confocal laser displacement sensor, showing height data. Calculated as $R_{surf} - \bar{R}_{base}$

Figure 3.10: Surface profile taken from the Keyence LT-9030M confocal laser displacement sensor, showing a raw voltage signal, and the processed height readings, and the x-axis shows the measurement number.

The measurements from the micrometer were recorded. And the data from the sensor was recorded for 10,000 measurements, at a rate of 50 Hz per second. This gave a run time 3 minutes and 20 seconds, to account for any wave patterns on the surface. This was outputted in the form of an analogue $-10 V - +10 V$ signal. The signal was recorded using a National Instruments USB-6009 DAQ and LabView, and a typical representation of this is shown in Fig. (3.10a) The signal was converted to a distance measurement by interpolating based on the output voltage, and the displacement range of the sensor

in the form:

$$(R_{surf} - R_{base}) + [(V_{surf} + 10/20) \times (B_u - B_l) + B_l] - [(V_{base} + 10/20) \times (B_u - B_l) + B_l]$$

where:

- R_{surf} is the surface micrometer reading
- R_{base} is the base micrometer reading
- V_{surf} is the voltage recorded for the surface measurement
- V_{base} is the voltage recorded for the base measurement
- B_u is the upper bound set in the sensor software
- B_l is the lower bound set in the sensor software

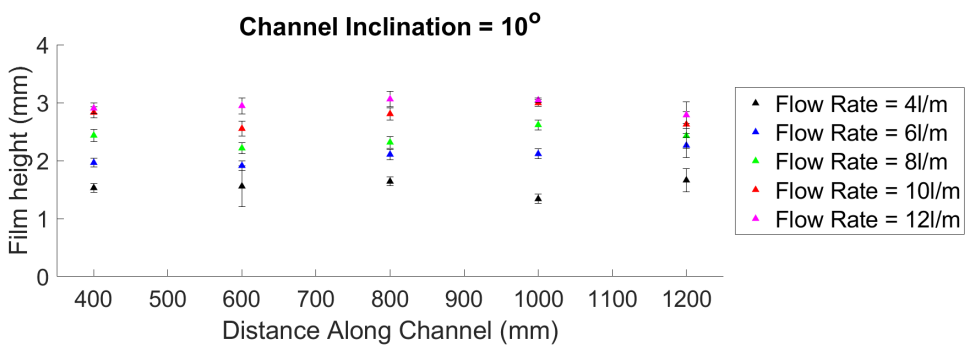
Measurements were taken at 200 mm intervals along the channel, at flow rates of 4, 6, 8, 10 and 12 l/m a typical graph of measured height against time is shown in Fig. (3.10b), and the average values are shown in Figs. (3.11a-3.11d). The data-points are the mean value for each position. The error bars are calculated as the arithmetical mean deviation of the surface as given by Degarmo et al. [98], in the form;

$$R_a = \frac{\sum |h_i - \bar{h}_f|}{n}$$

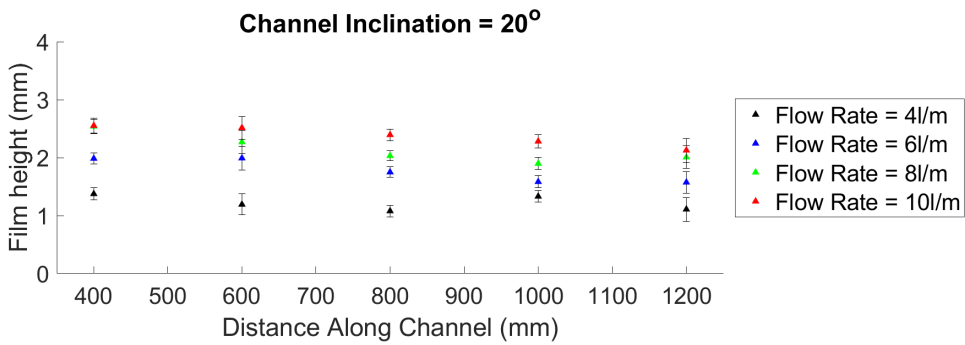
where:

- h_i is the individual film height measurement
- \bar{h}_f is the mean film height
- n is the number of measurements

It should be noted that R_a appears to be independent of the inclination angle of the channel

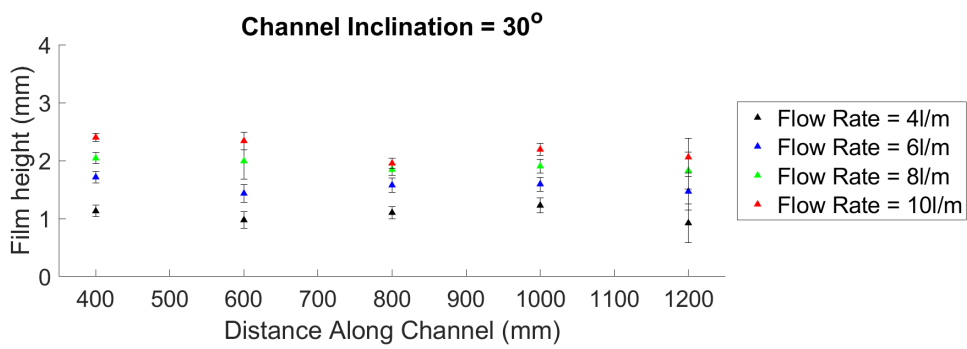


(a) Average film thickness along the channel for various flow rates at 10 ° inclination

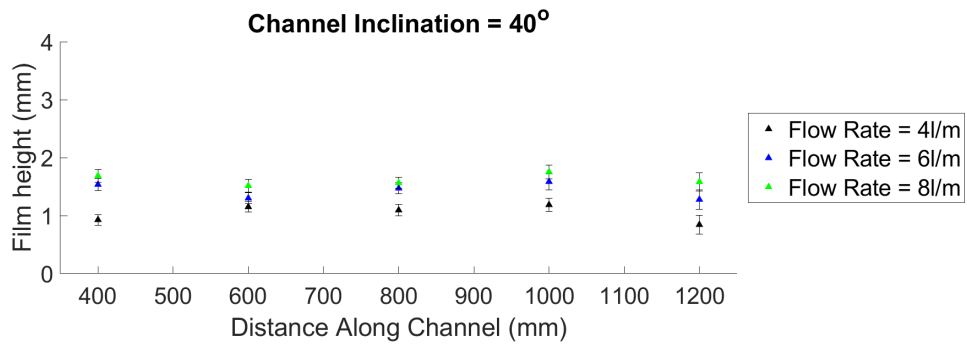


(b) Average film thickness along the channel for various flow rates at 20 ° inclination

Figure 3.11: Experimental measurements of film thickness for various flowrates and channel inclinations.



(c) Average film thickness along the channel for various flow rates at 30 ° inclination



(d) Average film thickness along the channel for various flow rates at 40 ° inclination

Figure 3.11: Experimental measurements of film thickness for various flowrates and channel inclinations.

Fig. (3.12) shows the velocities of the film, calculated by dividing the volume flow rate by the cross sectional area of the film ($V_f = \dot{Q}/base \cdot h_f$), the error bars indicate the velocity to 95 % confidence. The confidence interval affects the calculations most significantly for the thinner films, which generally shows larger error bars than when the film is thicker.

The work using this value can be divided into two parts, the crown skew (section 5.3.1), and the upstream and downstream crown modelling (section 5.3.2). With the prediction of the crown skew, a very large dataset is present which is then manipulated to create a global statistical correlation. Resulting from this, it can be anticipated that any errors will average out across the large number of experiments.

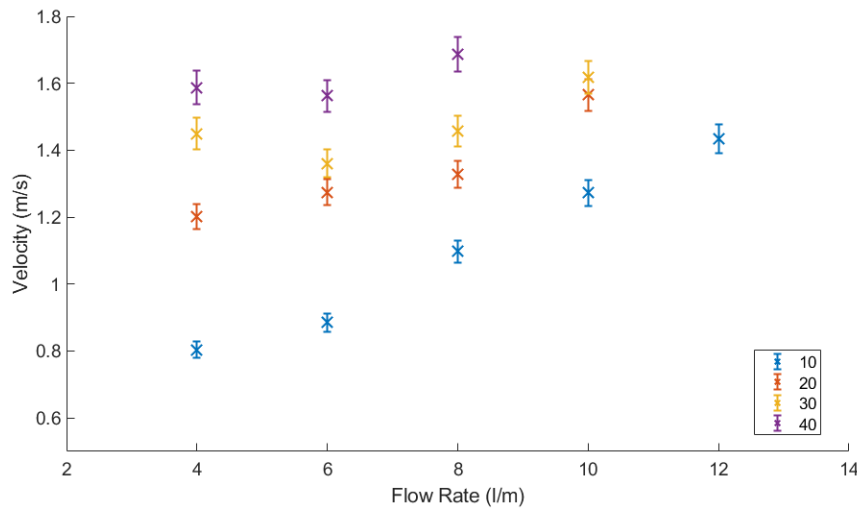


Figure 3.12: Bulk film speeds, including error bars calculated using the 95 % confidence intervals shown in Tbls. (3.3 - 3.6). The legend indicates the channel inclination angle in degrees

Previous studies have shown that surface roughness has an influence on post impingement behaviours. Tropea et al [62] postulated that surface roughness (R_a) has only a weak relationship with post-impingement behaviours in the range of $3(R_a/D)^{0.16} < \delta < 1.5$; a region for which the majority of our experimental conditions fall into, except for when $\dot{q} = 4l/m$ and the channel inclination is $\alpha \geq 30$. However, to ensure that the experimental results are not unduly affected, each case was repeated 10 times, and if any waves were deemed to have influenced the outcome, the experiment was repeated. For each condition, the experiments were performed only on one day.

Calculation of key dimensionless film parameters

Tables. (3.3- 3.6). Shows the calculated nondimensional parameters for film flow rates of 4, 6, 8, 10, and 12 l/m error in the flow rate assumed as the 2% error +1% variance, as taken from the RS components datasheet [96]. These values are calculated using standard values for fluid properties from data tables. These are the values which will be used as the film properties in the analysis of droplet impingement results. Examining the mean film velocities and thicknesses, these are of comparable values to those found by Wittig et al. [99], for oil film flow in aeroengine bearing chambers. (1 – 1.5 mm, 0.8 – 1.5 m/s). The Froude and Reynolds numbers of the channel are given by:

$$Fr = V_f / \sqrt{g \times h_f}$$

$$Re_f = \rho V_f R_h / \mu$$

Where:

- V_f is the bulk film velocity ($\dot{Q} / \text{width} \cdot h_f$)
- g is acceleration due to gravity (9.81 m/s)
- R_h is the hydraulic radius, ($R_h = [\text{width} \times h_f] / [\text{width} + 2 \times h_f]$)
- ρ is the fluid density at 30 °C (995.7 kg/m³)
- μ is the dynamic viscosity of water ($7.98 \times 10^{-4} \text{ Pa} \cdot \text{S}$)

The error values in Tbls. (3.3- 3.6) indicate a 95 % confidence interval, calculated using the method of Kline and McClintock [100] a sample form for Re_f is shown in Eqn. (3.3), and a sample calculation is included below in Eqn. (3.4). In this case errors for the fluid properties and channel width are presumed at 2 %. To ensure comparability with the error calculations for droplet parameters, the 95 % confidence interval is used for the error values of V_f and R_h ; as these parameters are derived from empirical measurements, their uncertainty values are calculated using Eqns. (3.1,3.2).

$$\frac{V_{f(\text{error})}}{V_f} = \sqrt{\left(\frac{H_{f(\text{error})}}{H_f}\right)^2 + \left(\frac{\dot{Q}_{(\text{error})}}{\dot{Q}}\right)^2 + 0.02^2} \quad (3.1)$$

$$\frac{R_{h(\text{error})}}{R_h} = \sqrt{\left(\frac{H_{f(\text{error})}}{H_f}\right)^2 + 0.02^2 + \left(\frac{\sqrt{(2 \cdot H_{f(\text{error})})^2 + 2^2}}{(2 \cdot H_f + 100)}\right)^2} \quad (3.2)$$

$$\frac{Re_{f(error)}}{Re_f} = \sqrt{\left(\frac{V_{f(error)}}{V_f}\right)^2 + \left(\frac{R_{h(error)}}{R_h}\right)^2 + 0.02^2 + 0.02^2} \quad (3.3)$$

$$0.0428 = \sqrt{\left(\frac{0.0247}{0.803}\right)^2 + \left(\frac{1.45 \times 10^{-5}}{0.00156}\right)^2 + 0.02^2 + 0.02^2} \quad (3.4)$$

Therefore, as for this case, $Re_f = 4629$, this implies $Re_{f(error)} = 198$.

Table 3.3: Key nondimensional film parameters at 10 °.

Flow (l/m)	Rate	Height (mm)	Mean Velocity (m/s)	Fr	Re_f
4		1.66 ± 0.0109	0.80 ± 0.12	1.18 ± 0.037	4629 ± 198
6		2.26 ± 0.0115	0.88 ± 0.11	1.29 ± 0.039	5177 ± 218
8		2.43 ± 0.0115	1.10 ± 0.13	1.60 ± 0.049	6453 ± 271
10		2.63 ± 0.0120	1.27 ± 0.14	1.85 ± 0.056	7479 ± 314
12		2.79 ± 0.0126	1.44 ± 0.16	2.09 ± 0.064	8478 ± 355

Table 3.4: Key nondimensional film parameters at 20 °.

Flow (l/m)	Rate	Height (mm)	Mean Velocity (m/s)	Fr	Re_f
4		1.11 ± 0.0109	1.20 ± 0.27	1.79 ± 0.059	6748 ± 326
6		1.57 ± 0.0104	1.27 ± 0.19	1.87 ± 0.058	7309 ± 312
8		2.01 ± 0.0093	1.33 ± 0.17	1.94 ± 0.059	7741 ± 325
10		2.13 ± 0.0109	1.57 ± 0.20	2.29 ± 0.071	9156 ± 386

Table 3.5: Key nondimensional film parameters at 30 °.

Flow (l/m)	Rate	Height (mm)	Mean Velocity (m/s)	Fr	Re_f
4		0.92 ± 0.0125	1.45 ± 0.44	2.17 ± 0.077	7976 ± 379
6		1.47 ± 0.0120	1.36 ± 0.25	2.01 ± 0.071	7804 ± 340
8		1.83 ± 0.0126	1.46 ± 0.23	2.14 ± 0.071	8460 ± 363
10		2.06 ± 0.126	1.62 ± 0.23	2.37 ± 0.073	9438 ± 401

Table 3.6: Key nondimensional film parameters at 40 °.

Flow (l/m)	Rate	Height (mm)	Mean Velocity (m/s)	Fr	Re_f
4		0.84 ± 0.0087	1.58 ± 0.36	2.39 ± 0.079	8651 ± 389
6		1.28 ± 0.0087	1.57 ± 0.25	2.32 ± 0.076	8880 ± 380
8		1.58 ± 0.0082	1.69 ± 0.22	2.48 ± 0.076	9694 ± 409

3.3 Visual Data Acquisition

This section outlines the set-up of data acquisition equipment, including the positioning of the high-speed cameras, lights and laser head. Also included are the necessary considerations when setting up the optics and software. Firstly, the positioning of the cameras is described for the various experimental set-ups. Then the dye seeding and optical considerations for BB-LIF are discussed. Finally, the settings of the camera and lenses are summarised.

3.3.1 Camera Positioning

As shown in Figs. (3.2, 3.13), the IDT OS4 high speed camera was positioned to the side of the channel, looking inwards. The other side of the channel had a Veritas Constellation 120E pulsed-LED light with a diffuser (tracing paper) in front of it to ensure an even light distribution.

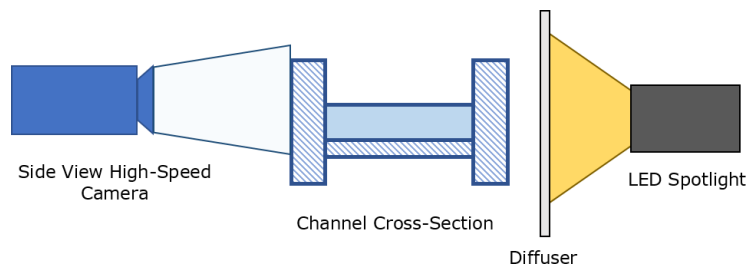


Figure 3.13: Diagram of the Camera Positioning

BB-LIF Set up

For the BB-LIF experiments, the side-view camera was set up in the same manner as described above, the primary difference was the reliance upon the laser and fluorescence to illuminate the target, rather than a conventional back light. A second camera was placed perpendicularly below the channel to record the crater and cavity development as shown in Figs. (3.14, 3.15). Alongside this a volumetric laser light sheet was located, powered by a Dantec DualPower laser, this projected a dispersed beam of monochromatic 532 nm light into the target area. A volumetric light sheet optic was used, which created an even region of illumination across the channel, and reduced the severity of any illumination corrections. The film was doped with Rhodamine 6G, which fluoresces at a higher wavelength than the laser light. The original 532 nm illumination from the laser could then be filtered out using a 532 nm notch filter, leaving all other

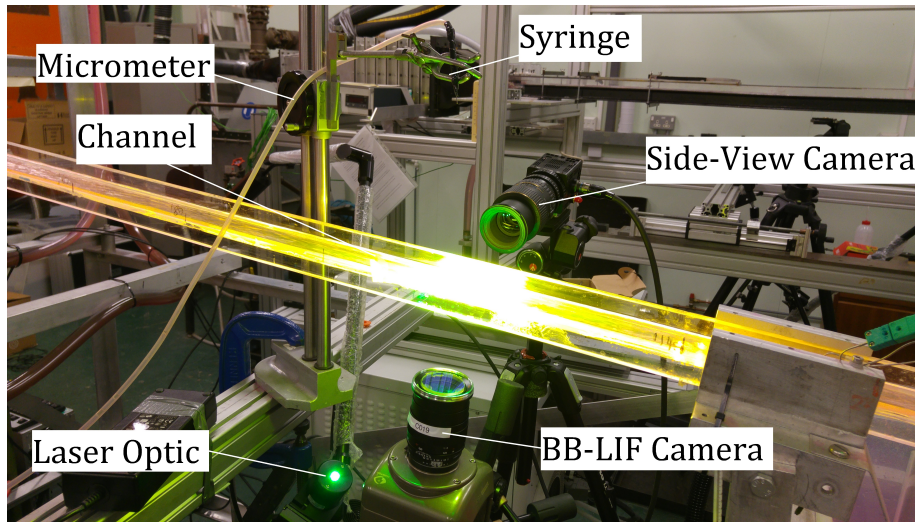


Figure 3.14: Positioning of the cameras and laser optics

spectra unimpeded. This allowed the camera to observe only light produced from fluorescence of the film.

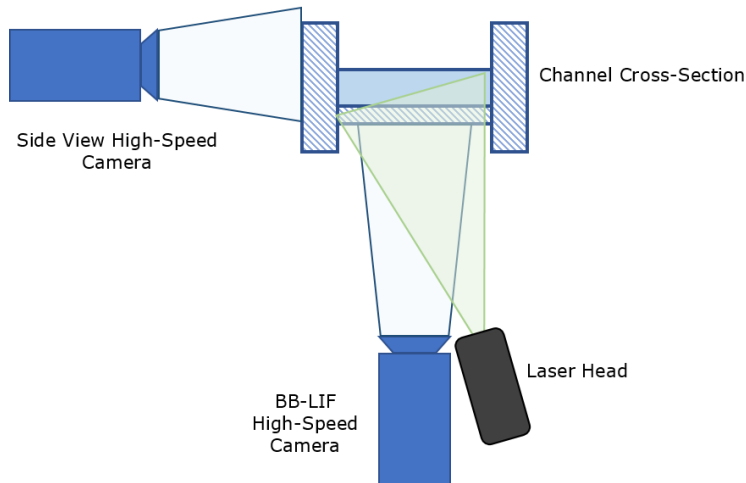


Figure 3.15: Diagram of the Camera Positioning

3.3.2 BB-LIF Dye Concentrations

For the experiments undertaken using the BB-LIF technique, it was necessary to seed the droplet, film or both with Rhodamine 6G dye. Depending on the thickness of the fluid layer, concentrations were in the range of 8-15mg/l as suggested by previous works [36] to provide suitable illumination

and contrast. Careful selection of the concentration was important, as at high thicknesses and concentrations the emission begins to exhibit non-linear behaviours [101]. The published BB-LIF theory and mathematics does not compensate for this non-linear response, and depth determination would be unproven and increased in difficulty.

When only the droplet was dyed, conventional LIF was used to track the spreading of droplet material within the cavity. As the droplet fluid forms very thin layers on the inside of the crater. It was required to increase the dye concentration above the linear limit to approximately 30 mg/l . This precluded the use of BB-LIF, however ensured that the droplet material could be accurately tracked. Droplet spreading is considered important as droplet spreading has significant implications for heat transfer between the droplet and film.

3.3.3 High Speed Camera Set-up

This section details the processes undertaken to set up the individual cameras for experiments. The exposure time was set to avoid motion blur being present in the images. For these experiments, a 105 mm micro-NIKKOR lens was used. This was set up by setting the focal plane to the centre of the channel where the droplet impinges. To achieve this, an object of half the channel width was placed against the far side of the channel, and the focal plane adjusted until the edges of the object were sharp and well-defined. The aperture was set by taking test images, and closing it until both the front and back of the crown were in focus. For BB-LIF images the calibration plate was placed on the base of the channel and the calibration image was taken under ambient illumination and higher exposure times.

To ensure accuracy, new calibration images were regularly taken, to account for any unwanted movement of the camera.

3.4 Data Processing and Analysis

This section outlines the data processing and analysis utilised to generate quantitative data from the videos of impingement for the conventional high-speed camera imaging. Whilst there is distinct overlap between the data processing techniques, methodologies specific to BB-LIF are later discussed in Section 3.5.

3.4.1 Preprocessing

The first steps in data analysis were to import the images into MATLAB, enhance the illumination and contrast, and determine the spatial calibration factors.

Importing to MATLAB

Depending on which camera was used, the data could be imported directly into MATLAB using third party functions. Data from the Phantom V12.1 camera was imported using the `cineRead` function, produced by Brainerd [102], whilst Data from the IDT OS4 camera was imported using functions supplied by the original equipment manufacturer, in the software development kit [103].

Illumination Correction

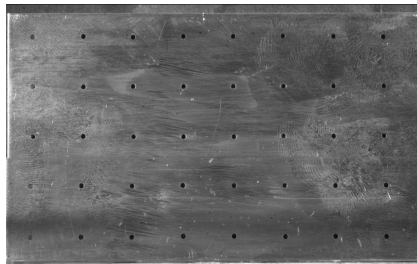
After importing the data, the next step was to adjust the illumination. As the level of illumination was consistent across the image, this was achieved simply by adjusting the contrast of the image using the MATLAB function `imadjust`. By default, this function maps the intensity values in the image so that 1% of the data is saturated at the highest and lowest intensities of the image. This increase in contrast assists the implementation of threshold and edge-detection techniques in later processing.

Spatial Calibration

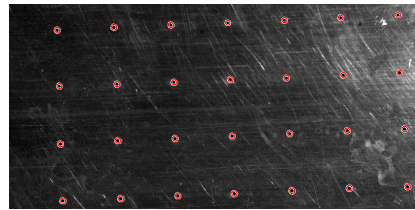
The next step in the data processing was to spatially calibrate the images. This made it possible to calculate droplet and crater sizes, and compare the crater sizes in different impact conditions.

This was done by creating a calibration plate, with a number of 1 mm holes in it, equispaced at a 10 mm pitch on in grid pattern (See Fig. (3.16a)). The cameras then recorded a frame with the calibration plate in the shot. This

made it possible to identify the centroid of the holes using the Matlab function `imfindcircles`. Knowing the pixel coordinates and the distance between the holes, it was then possible to calculate the number of pixels per mm in both images. This was undertaken for both the side-view and BB-LIF images where appropriate. Typical scaling factors for the BB-LIF images were $20.49 \pm 0.25 \text{ pix/mm}$ to 95% confidence, calculated from all 10 calibration images taken at the same notional location. For the side-view images, a typical scaling factor was $53.66 \pm 0.45 \text{ pix/mm}$, giving an error of approximately 1% across the two views.



(a) Image of the calibration plate taken with the high-speed camera



(b) Holes detected on Calibration plate using `imfindcircles`

Figure 3.16: Spatial calibration

3.4.2 Image Feature Detection

After preprocessing, the next step in analysis was to determine features of the impingement, this was achieved using a variety of automated and manual processes outlined below

Detection of the Impinging Droplet

The impinging droplet properties were calculated using canny edge detection, and the Matlab `imfindcircles` function. The radius was determined by taking the mean across several frames, and the velocity was determined by observing the displacement between the final frames before the droplet hit the film. This displacement could then be converted into a velocity by dividing by the frame rate. The frame of impingement was defined as the moment the droplet touched the film, and this was determined manually from the frame number.

Impinging Droplet Properties

Whilst theoretically each droplet should be almost identical in size, to account for any discrepancies, each droplet size was measured, to allow any omission

of deformed or mis-sized droplets. The droplet sizes for high-speed camera investigations were collated and Fig. (3.17) shows histograms for each nominal droplet size, calculated using the `imfindcircles` function in Matlab (discussed in more detail in section 3.4). The averages of these were found to be $2.086 \pm 0.0065 \text{ mm}$, and $3.076 \pm 0.0129 \text{ mm}$, with uncertainties to 95% confidence interval. For the BB-LIF experiments it was necessary to tilt the syringe

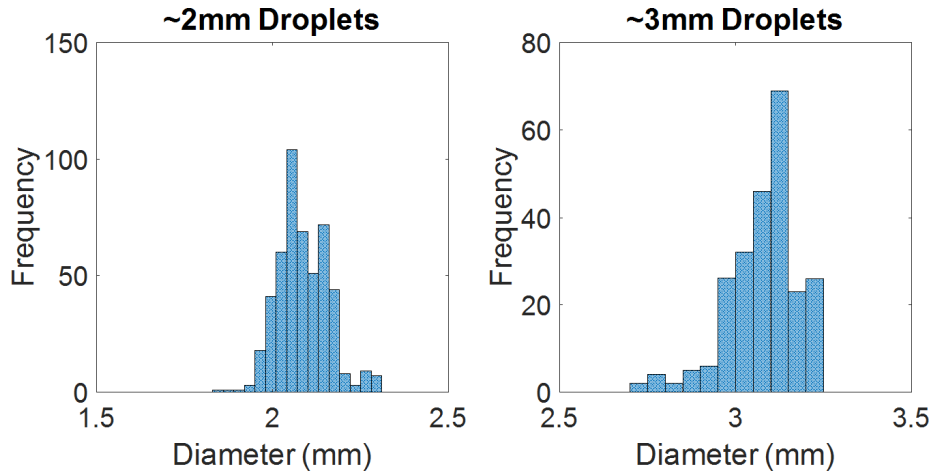


Figure 3.17: Histograms of droplet sizes produced from syringe for conventionally illuminated experiments

to avoid the fluorescent fluid within appearing within the frame of the camera and disrupting the measurements. In these cases, the droplet sizes were found to be $2.34 \pm 0.014 \text{ mm}$ and $3.34 \pm 0.021 \text{ mm}$ for 2 mm and 3 mm droplets respectively across the 350 tests at each condition. Shown as a histogram in Fig. (3.18).

Whilst these sizes are different, they are still within 15 % of each other across the two testing regimes. Furthermore, for any comparisons made between the two datasets, the variance should be accounted for using nondimensional parameters. Alongside this, repeatability of the experiments, was ensured at each experimental condition by the use 10 repeats. If any of these repeats were influenced by waves on the film, they were discarded and the experimental re-performed.

The droplet centroid was calculated using `imfindcircles` (discussed in more detail in section 3.4) for the last two frames prior to impingement. Knowing the differences in centroid, time between frames, and scaling factor, the velocity could be determined. For comparison, the measured values are compared to predictions from basic kinematics with and without air resistance, as calculated using Eulers method [104] in Fig. (3.19).

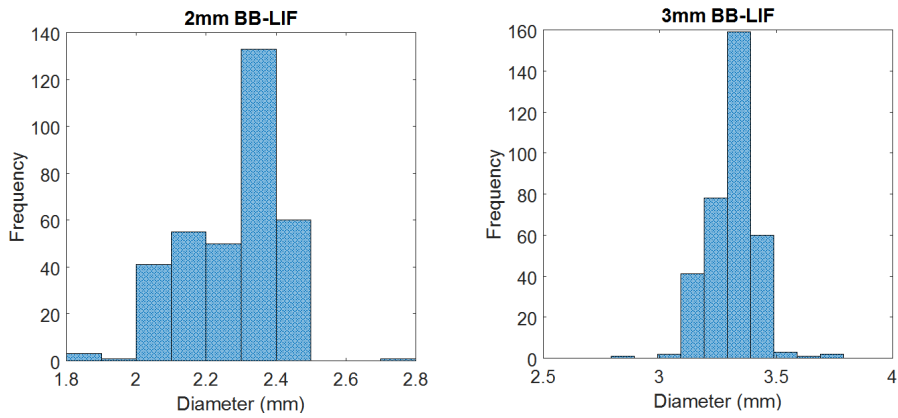


Figure 3.18: Histograms of droplet sizes produced from syringe for BB-LIF experiments

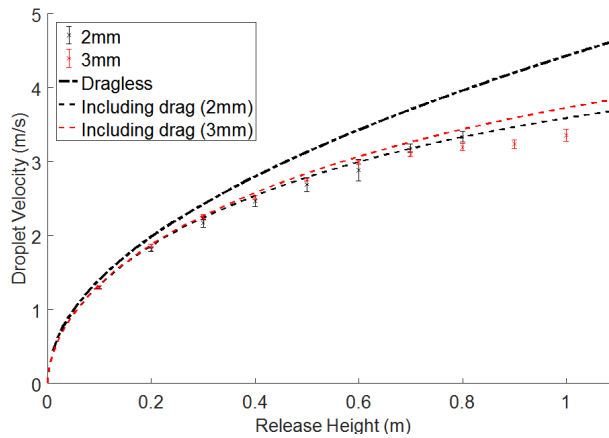


Figure 3.19: Mean droplet speeds for 2 mm and 3 mm impinging droplets

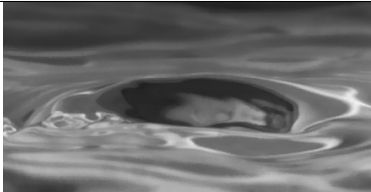

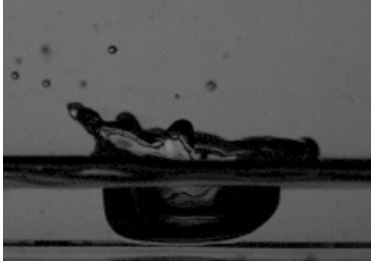
Impingement Outcome

The impingement outcome was manually determined by watching the images. Each outcome type was assigned a numerical value, and this was input using a dialogue box in Matlab produced using the `questdlg` function. To ensure consistency it was necessary to determine a set of criteria for each impingement type, this is outlined in Tbl. (3.7)

Secondary Droplets

Due to the complexity of the image after a droplet impingement, the secondary droplet parameters were determined manually. Firstly, a droplet was chosen that formed on the upstream side (as upstream splashing was observed more

Table 3.7: Impingement Outcome Classification

Impingement outcome	Criteria	Image
Coalescence	Minimal disturbance on the surface any waves produced have heights less than their width	
Crown Formation	Production of a crown or wave with a height greater than its width.	
Crown Splash	Production of a crown and any generation of secondary droplets.	

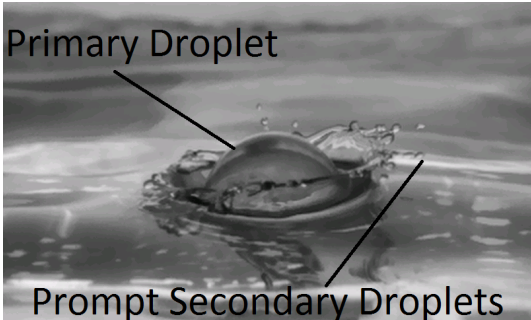
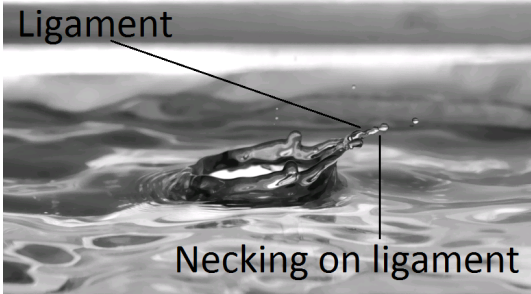
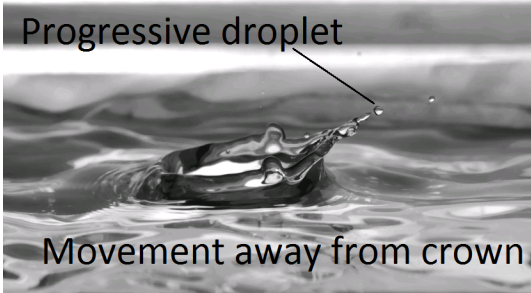
consistently) of the impingement site, and remained in focus. Secondly the frame in which the droplet detached was recorded. Comparing this to the Impingement frame allowed the time of secondary droplet formation t_{SD} to be determined. The size and velocity of the droplet was measured manually using the `ginput` function and selecting the left and right edges of the droplet. Repeating this procedure across two frames allowed the average diameter and the velocity to be calculated from the coordinates. Only droplets which remained within the focal plane of the camera were used, as otherwise it would be impossible to accurately measure the droplet velocity due to the out-of-plane component. Furthermore, only visibly spherical droplets were chosen, with distorted droplets being omitted due to the increased difficulty of determining their radius.

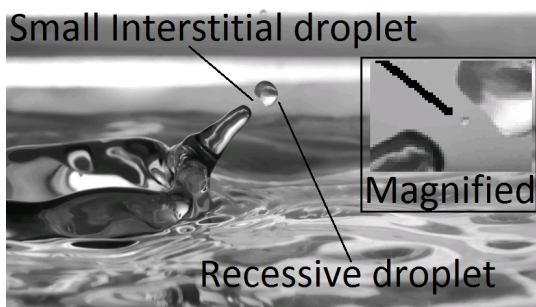
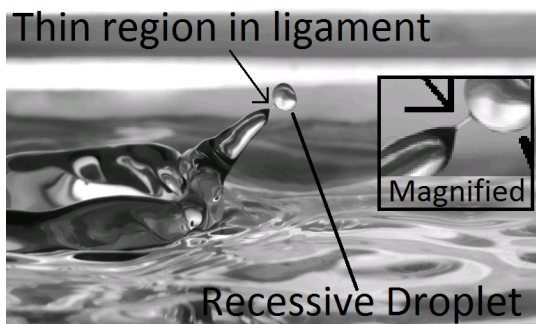
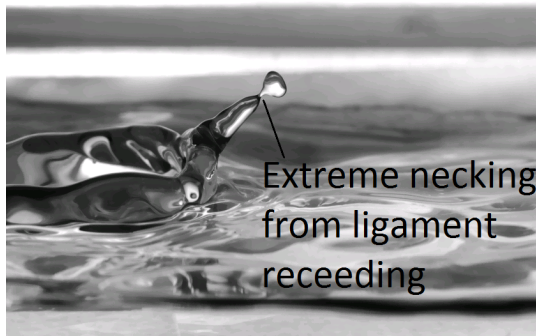
3.4.3 Secondary Droplet Production Mechanism

The secondary droplet production mechanism was determined manually, this involved observing the impingement and comparing to the criteria set out in Tbl. (3.8) The typical heuristics to determine the boundary between prompt and progressive droplets involved examining when the fluid forming the droplet was displaced. Fluid that was displaced from the droplet-film interface and breaking up under Richtmyer-Meshkov instability at the instant the droplet hit the film was regarded as prompt splash. However, fluid displaced later, in the inertial regime, at the end of long ligaments were regarded as progressive splashing.

The boundary between Progressive and Recessive splashing was characterised by examining the movement of the crown fluid around the detachment time. If the crown continued to increase in size after the droplet detached it was classified as progressive, whereas if the crown began to shrink, and the ligament receded rapidly it was recessive.

Table 3.8: Droplet production mechanism criteria

Mechanism	Description
	<p>Prompt Caused by Richtmyer-Meshkov instability at the droplet-film interface immediately after the droplet hits the film.</p>
	<p>Progressive Caused by short-wave breakup of the ligaments as the crown expands. Droplet accelerates away from ligament tip</p>
	



Recessive Caused by the ligament beginning to withdraw, produces very large droplets, with low apparent velocity. Remaining ligament tail accelerates away rapidly under surface tension

Interstitial During the recessive phase, a small droplet is formed in a manner similar to *satellite* droplet production for gravity driven jets. The thin region of fluid separates at both ends, and forms a small droplet.

3.5 BB-LIF Image Processing

The BB-LIF data facilitated a much greater level of automated analysis for the conventional high-speed imaging. However, greater care had to be taken in the pre-processing, to ensure accurate results.

3.5.1 Conversion to Height Data

The first step in converting from pixel intensities to height data was to calculate the absorption coefficient. This was achieved by measuring the intensity of light emitted by the dye for fluids of known thickness, this could then be fitted in Matlab to the form shown in Eqn. (2.27). This was achieved using a series of cuvettes placed in the centre of the image to give different thicknesses of fluid. Illumination correction was omitted, as the volumetric light sheet produced an even intensity in its centre, and any small discrepancies could be accounted for by averaging the intensity over an area.

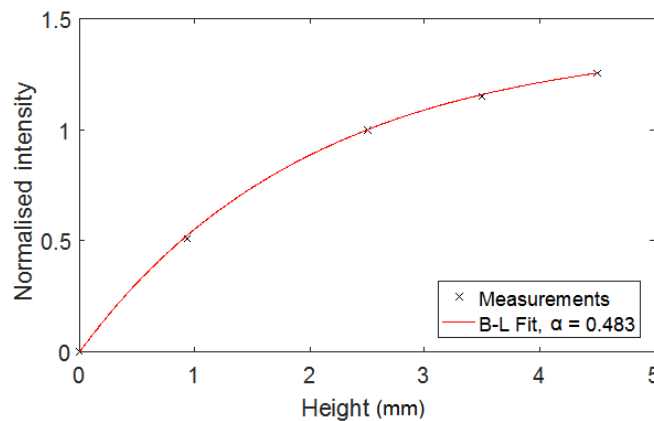


Figure 3.20: Calculation of the absorption coefficient

The absorption coefficient was calculated by plotting the thickness of fluid in the cuvettes, against the measured intensity (normalised by one of the dat-points) as shown in Fig. (3.20). From this, it was possible to for α_{abs} using Eqn. (3.5), and curve fitting in Matlab. This gave a value for α_{abs} which could then be used to convert film intensities into height data.

With the absorption coefficient calculated, the next step was to load the image into Matlab, this gave Fig. (3.21a), exhibiting uneven illumination. To fix the uneven lighting, the illumination correction matrix, $C_{(c,y)}$ was created. This was undertaken by first calculating the nominal intensity level correlating to the film height h_f , using the calculated absorption coefficient, and Eqn. (3.5).

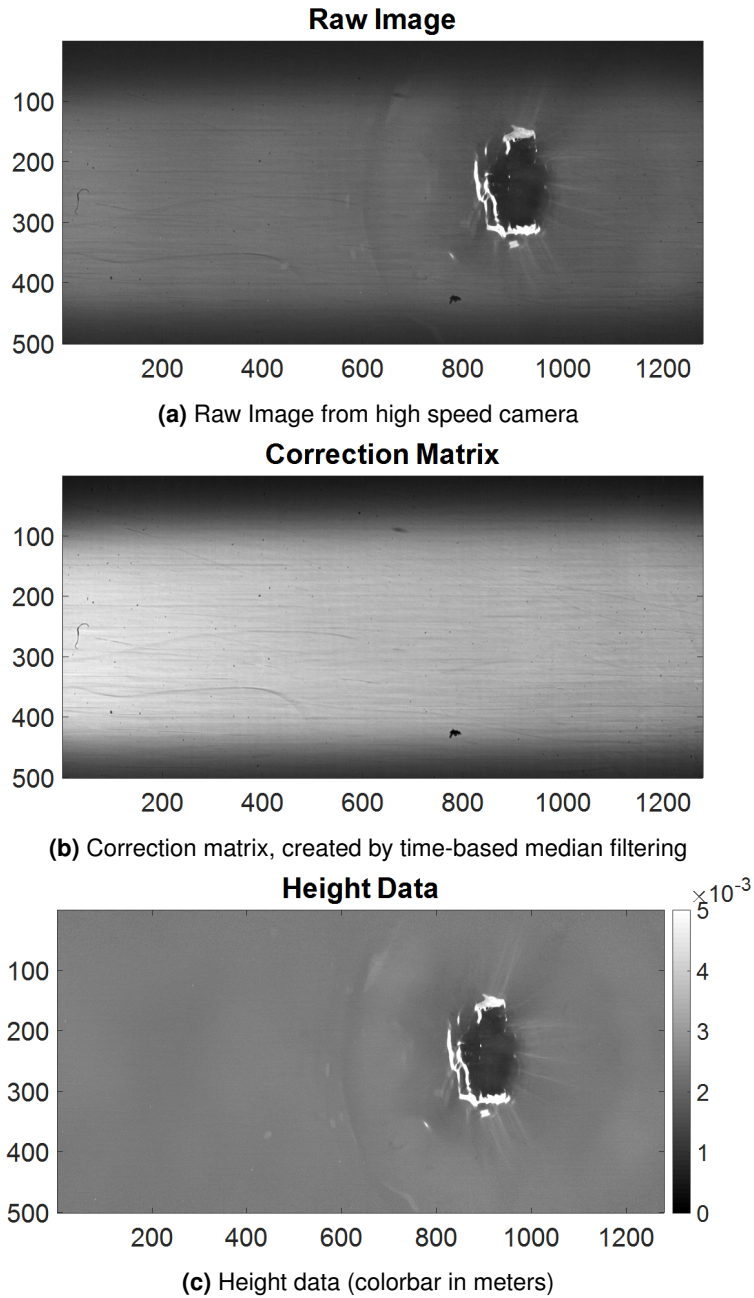


Figure 3.21: Steps of BB-LIF processing

$$J_{nominal} = [1 - \exp^{\alpha_{abs} \cdot h_{nominal}}] \cdot [1 + k_{refl} \cdot \exp^{-\alpha_{abs} \cdot h_{nominal}}] \quad (3.5)$$

Then, time-based median filtering [105, 106] was used to create a background image. The intensities in this background image could then be used to correct the illumination in the original image, as per the theory from Eqn. (2.27). This was achieved by creating a correction matrix that would compensate for uneven illumination across the image, the result is shown in Fig. (3.21b). It should be noted that this technique will result in a loss of resolution in the Z-axis for the darker areas, as the same range of depths is represented by fewer intensity levels. However, this effect was minimised by the use of a volumetric light sheet, which provided a large region of even illumination.

The final step of pre-processing was to convert the images into height data, this was achieved by rearranging Eqn. (2.27) to solve for h , for speed and accuracy this was implemented using the Matlab `solve` function. After conversion, this produced the matrix shown in Fig. (3.21c) showing even height values across the film, and the height differences in the cavity and disturbance waves. It is important to note that the height within the crown could not be resolved. This can be attributed to two reasons; the BB-LIF equation presumes a constant coefficient of reflectivity which is not valid in regions of high curvature, and the presence of total internal reflection of light within the crown increasing the apparent brightness values.

Crown and Crater Properties

The size of the crater and crown, in the directions both parallel and normal to the flow were determined by thresholding. The threshold value was determined by analysing the data using a histogram of the film values under nominal conditions, as shown in the upper plot of Fig. (3.22). The upper and lower thresholds were then placed either side of this peak. Any values outside these thresholds could then be considered as representing the crown or cavity, a histogram of which is shown in the lower plot in Fig. (3.22). Returning to actual images Fig. (3.23a), is a false coloured image, where the colour represents the height as shown by the colour-bar. The material below the lower threshold was easily segmented into the crater (3.23b), and the material above the upper threshold as the crown (3.23c). These images were achieved through simple thresholding techniques, applying *greater than* and *less than* operators to the pixel values based on the determined thresholds.

From these images, the furthest extent of the features in the x and y direc-

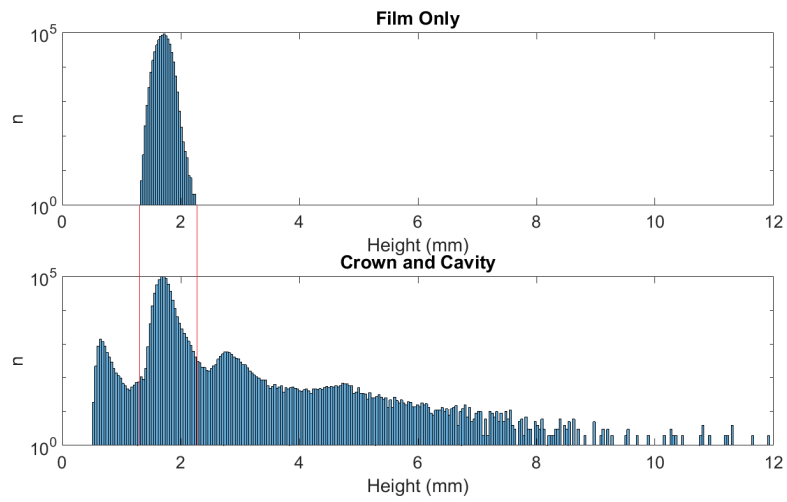
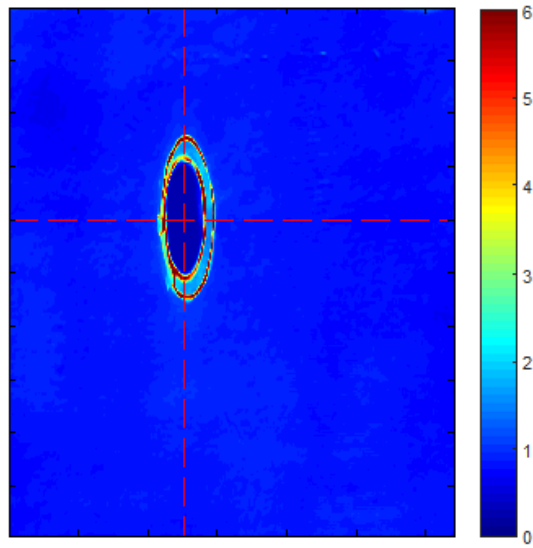
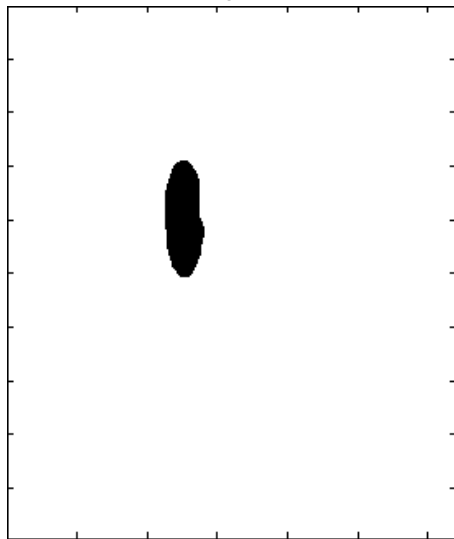


Figure 3.22: Histogram of Film-height values, showing the thresholds used for feature detection

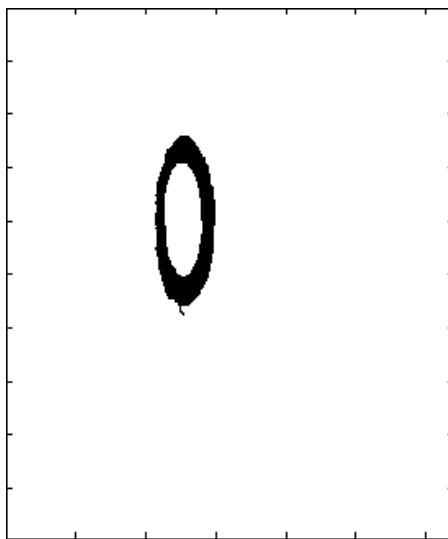
tions could be found, corresponding to the crown or crater dimensions. For crown detection, further filtering was undertaken to remove any secondary droplets from the image using the `bwareaopen` function, which omitted any regions below a manually defined number of pixels.



(a) BB-LIF Image with colour scale showing the height in mm



(b) Detected Crater

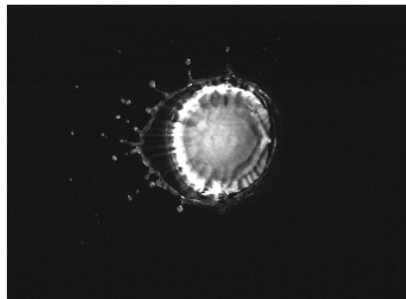


(c) Detected Crown

Figure 3.23: Detection of crown and crater using the Thresholding technique

Droplet Spread within the Cavity

The spread of the droplet within the cavity was determined using the same threshold techniques as used to determine the properties of the crown and crater. The raw image from the high-speed camera was imported into Matlab (Fig. 3.24a). The threshold was then set by creating a histogram, (Fig 3.25) to a level just above the noise of the camera. This allowed differentiation between the dark background and the fluorescent droplet material. Finally, logical operators were applied determine the regions with illumination greater than the threshold, as shown in Fig. (3.24b). The bounds and area of this region could be calculated using `regionprops`.



(a) High-Speed Camera Image



(b) Thresholded to detect droplet material, secondary droplets removed using `bwareaopen`

Figure 3.24: Detection of Droplet material from thresholding of the High-Speed Camera images.

3.6 Conclusions on Data Analysis

This chapter has discussed the data analysis techniques applied to the data from both the conventional and BB-LIF imaging. This includes detection and characterisation of the impinging droplet, analysis of the high-speed images, and conversion and analysis of the BB-LIF experiments.

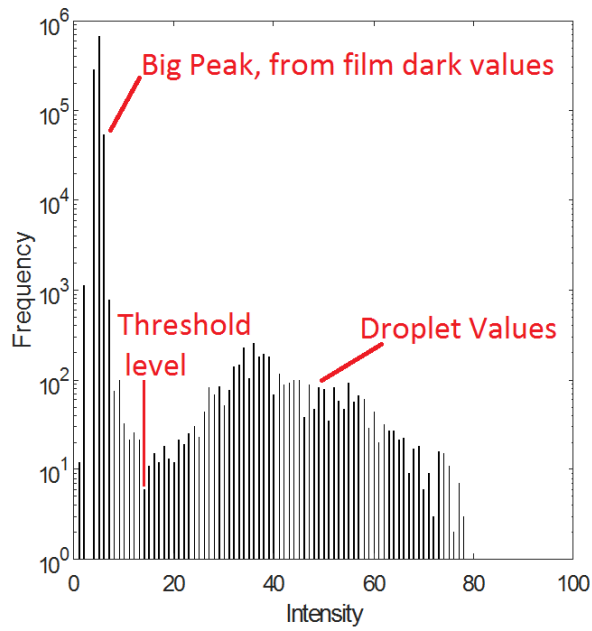


Figure 3.25: Histogram of intensity values from 3.24a

Chapter 4

Secondary Droplet Production

The production of secondary droplets is a key cause of parasitic efficiency losses within the highly rotating flow of an aeroengine bearing chamber. There is a pressing economic and environmental need to reduce these losses, and to increase efficiency. Typically, this is achieved by design iterations which are supported by CFD simulations; however, these simulations can be highly computationally expensive, creating a great burden in terms of cost and delays to the project.

The aim of this work is to increase physical understanding and to aid in large-scale Computational Fluid Dynamics. This is achieved by devising correlations from experimental data, that can then be applied in a simulation, rather than requiring the modelling of each individual droplet impact, with associated significant savings in labour and computational time.

This chapter presents data and analysis pertaining to secondary droplet formation and characteristics, the results were obtained through analysis of high-speed images. Both qualitative and quantitative analyses are presented and comparisons with existing works from static film impingement literature is made.

The work undertaken can be broken down into four main categories;

- The transition between coalescence, crown formation and splashing behaviours.
- An investigation into the physics of ligament breakup in varying conditions.
- The number of secondary droplets produced from the crown.

- The properties of these secondary droplets.

For the sake of brevity, nominal droplet sizes will be used in the course of this discussion, as defined in section 3.4.2.

4.1 Impingement Outcomes

Previous authors have observed that secondary droplet production is dependent on the characteristics of the impinging droplet for impingements on static films [20, 10, 19]. However, there is a remarkably small body of work concerning droplet impingements where the film is moving. The aim of this section is to compare the conditions under which droplet production occurs with previous understanding for static film impingements.

To delineate between impingement outcomes the criteria from Tbl. (3.7) are used to categorise the outcome. Typically, previous authors [17, 8, 10] have evaluated this data by plotting the splashing parameter (K) against the dimensionless film thickness (δ). As previously discussed in section 2.1.2, this work uses the form of K from Cossali et al. [8] (referred to as K_C). The velocity component used in the calculation will be indicated with the following nomenclature $K_{C(V_n)}$ indicates the velocity normal to the film, $K_{C(V_d)}$ indicates the total droplet velocity, and $K_{C(V_t)}$ indicates the component of droplet velocity parallel to the film.

Then to analyse the data, several parameters were determined from the high-speed camera images. The impinging droplet properties were characterised by applying a circular Hough transform across the last frames before the impingement. Other properties, including the impingement outcome, secondary droplet size and velocity, and number of secondary droplets were determined manually using the heuristics defined in Section 3.4

Figure. (4.1) shows $K_{C(V_d)}$ against δ with the three impingement types plotted alongside the $K_{C(V_d)} = 700$ boundary between coalescence and crown formation, and $K_{C(V_d)} = 2100$, the boundary between crown formation and crown splashing, both from Okawa et al. [19] for normal impingements upon static films. On this figure, higher value of δ equates to a higher ratio between film thickness and droplet diameter, and as this work only focused droplets of water, a higher value of $K_{C(V_d)}$ equates to either a larger or faster droplet (higher We_d). From this, it is evident that although points are scattered either side of the boundaries, there is reasonable agreement with these established static film transition points. Okawa et al. [19] found that for inclined impingements upon static films, use the droplet velocity gave good agreement to the $K_{Cossali} = 2100$ transition when $\alpha < 50$. This is unexpected, as previous work

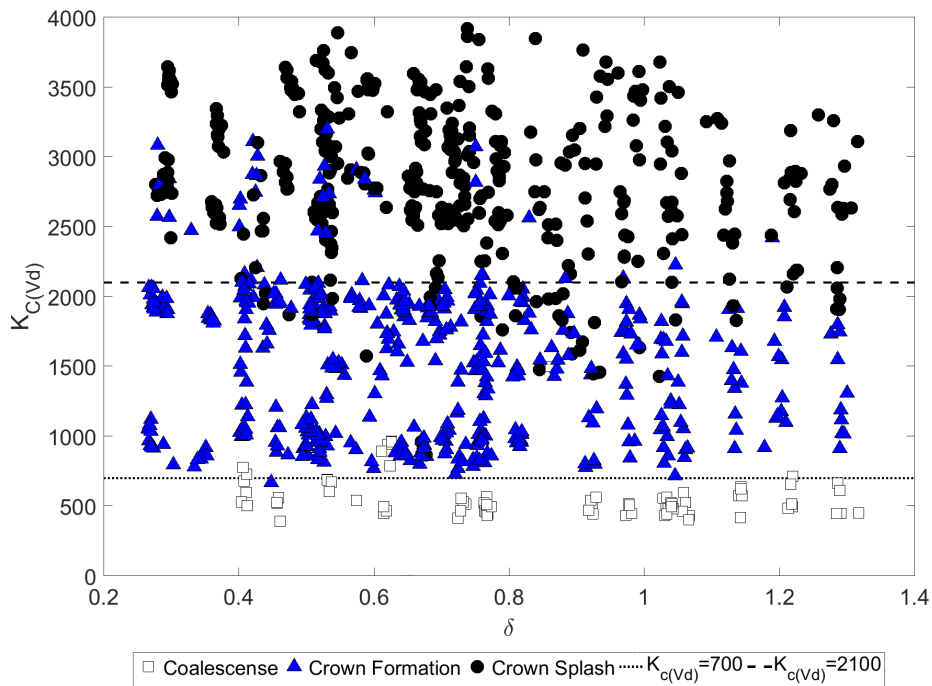
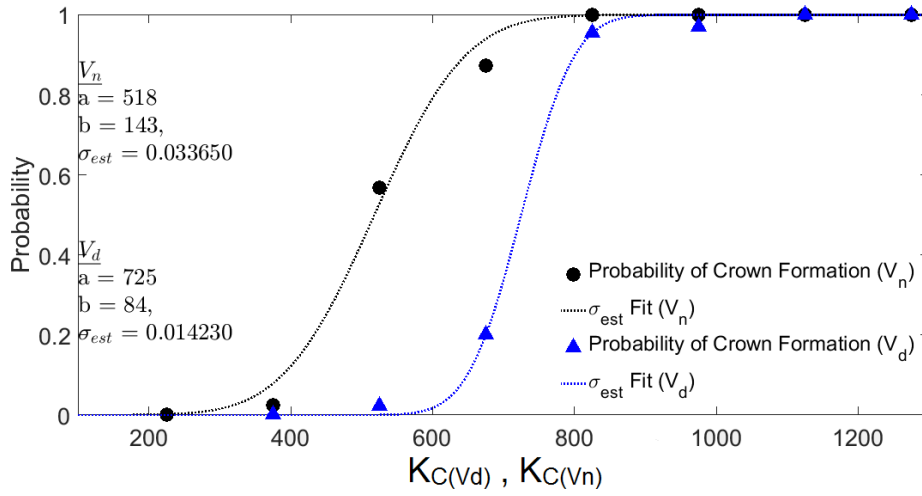


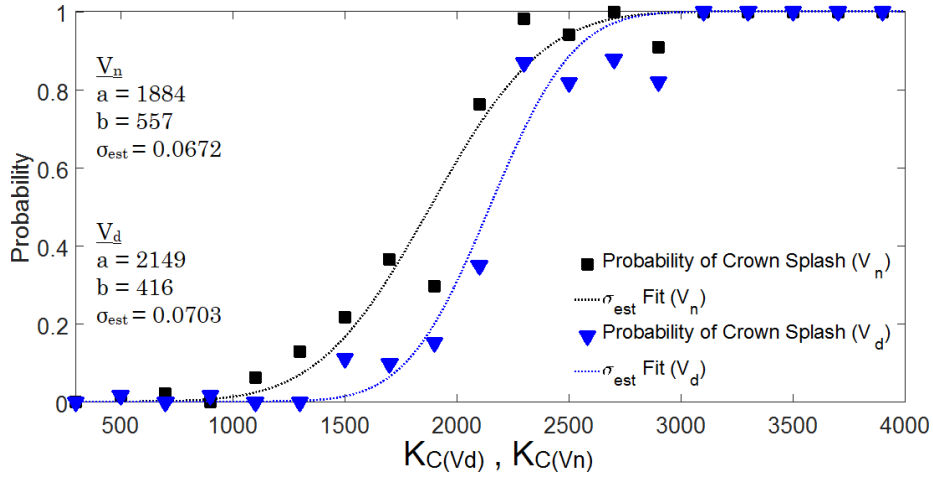
Figure 4.1: Impingement outcomes against δ and K_C calculated using Droplet Velocity (V_d) showing agreement with the static film boundaries of $K_{C(V_d)} = 700$ & $K_{C(V_d)} = 2100$.

by Alghoul et al. [17] on moving films has shown that the film movement enhances the crown size on the upstream side, which as one may expect the threshold of splashing to be decreased. This is an important finding as not only does it bring clarity to a scenario where there is a level of disagreement within the literature, and suggests that there may be scope for successful application of correlations from static-film literature for moving-film impingements.

When examining the literature, it was noted that there were no reported cases of a robust statistical approach being used to determine the transitions between behaviours, with the placement seemingly dependent on qualitative observations. Therefore, it would be useful to develop a statistical approach to determine these boundaries, and characterise the transitions in a more definite and numerical manner. To this end it was decided to create probability histograms for the impingement outcomes. This was achieved by creating bins in the K_C domain. this process was undertaken for both V_n and V_d are shown, as it was anticipated that this work would give further insight and conclusivity into the correct form of K_C to use in the determination of impingement outcomes. Each bin had a width of $K = 300$ found through trial and error. Within each bin, the probability of each outcome was calculated in the form shown in Eqn. (4.1).



(a) Probability of Crown Formation against $K_{Cossali}$ calculated using both V_d and V_n



(b) Probability of Crown Splashing against K_C calculated using both V_d and V_n

Figure 4.2: Statistical analysis of impingement outcome probabilities

For statistical significance, it was ensured that each bin contained at least 10 impingements.

$$Probability = \frac{N_{Outcome}}{N_{Total}} \tag{4.1}$$

This technique generated the data points shown in Fig. (4.2) *a* and *b*. Examining the data, it seemed that the curves had the form of a cumulative distribution function (*CDF*). This is a function used to represent the area under a continuous distribution curve, and hence the cumulative probability of an outcome at a specific point on the x-axis.

Eqn. (4.2) was fitted to each dataset with the use of constants the *a* and *b*. *a* gives a translation in the x-axis, which represents the value of K_C at which there is equal probability of either outcome. *b* is a scaling parameter, which provides an indicator of the sharpness of the transition, with a higher *b* value indicates a more gradual transition and vice-versa.

$$P(\text{outcome}) = CDF \left(\frac{(K_C(V_n) - a)}{b} \right) \quad (4.2)$$

Fig. (4.2) *a*, shows the probability of crown formation against $K_C(V_n)$ and $K_C(V_d)$, with the fitted values of *a* and *b* for each velocity term being shown on the graph as determined by the MATLAB curve fitting toolbox. The standard error of the estimate (σ_{est}) is shown alongside these values, and is an indicator of the level of error between the data and the fitted curve. Across all cases this was very low, indicating a good fit to the data. This information is shown for the data on crown splash probability in Fig. (4.2) *b*.

Firstly, by examining the magnitudes of *b* for each transition, the value is smaller when droplet velocity (V_d) is used to calculate the splashing parameter K_C than when the normal velocity (V_n) is used. This indicates a steeper gradient, and therefore a sharper and more defined transition. This supports the observations made for Fig. (4.1) that V_d is the more appropriate velocity term for nondimensionalisation.

Furthermore, the values for the point of equal probability (*a*), which can be considered as the threshold between behaviours. Is at $K_C(V_D) = 725$ and 2149 for the Coalescence/Crown Formation and Crown Formation/ Crown Splash boundary respectively. These values are extremely close to those found by Okawa et al. [19] for static films. Therefore, this statistical analysis further supports the argument that static film boundaries are valid for impingements upon moving films.

The variables *a* and *b* obtained by employing V_d in calculation of K_C are summarized in Table. 4.1.

Okawa et al. [19] observed a dependence on impingement angle for more severely inclined impingements ($\alpha > 50$). Therefore, it was also decided to investigate the effect of impingement angle on the transitions between impingement outcome types. Whilst the highest level of inclination to the film within this work was 40° , there was concern that the film velocity may also influence

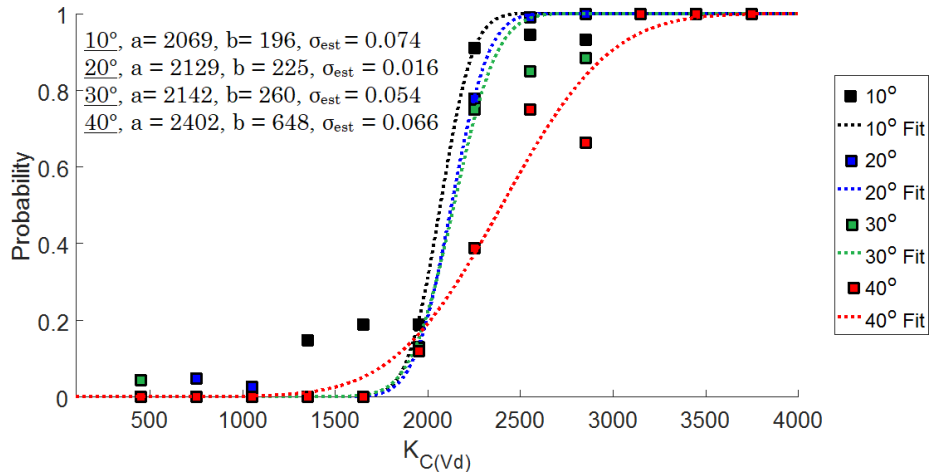


Figure 4.3: Crown Splashing occurrences separated by Impingement angle against $K_C(V_d)$. Showing similar behaviours for $10 < \alpha, 30$, and a much more gradual transition at a higher value of $K_C(V_d)$ when $\alpha = 40$

the transitions at these highly inclined conditions. This investigation was undertaken using the same statistical techniques, but with the dataset subdivided by angle. The results of this analysis are shown in Fig. (4.3) and Tbl. (4.2). As is evident for $\alpha = 10 - 30$ the fitted curves are almost identical, with a sharp transition around the $K_C(V_d) = 2100$ area. However, as the angle increases to $\alpha = 40$ an increase in the transition point is evident, and the sharpness of the transition decreases and becomes more gradual. This is reminiscent of the behaviour observed by Okawa et al. [19]; however, for inclined impingements upon static films, Okawa et al. [19] observed an increase in the critical value of K_C when the impingement angle was 60° , whereas our experiments show an increase in the critical K_C value at much lower inclinations. It is hypothesised that this may be due to the relative velocity between the droplet and film inhibiting splashing at these conditions.

Table 4.1: Transition Equation Coefficients for Eqn. (4.2) when V_d is used in the calculation of $K_{Cossali}$

Transition	a	b
Coalescence / Crown	725	84
Crown / Crown Splash	2149	416

Table 4.2: Transition Equation Coefficients for Eqn. (4.2)

Inclination	10°	20°	30°	40°
Transition	2069	2129	2142	2402

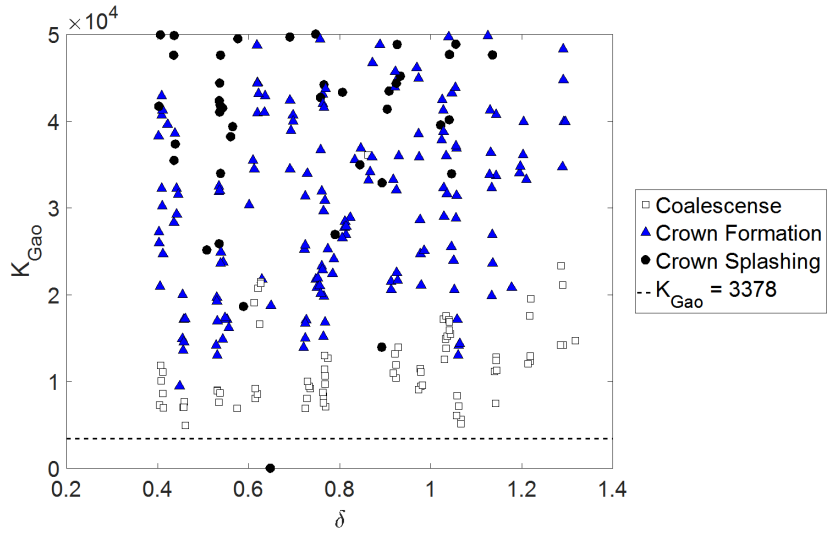
Other Splashing Parameters

Alongside the splashing parameter from Cossali et al. [8], other derivations from Huang and Zhang [46], and Gao et al. [45] were considered. Fig. (4.4) shows the experimental data plotted with the K_{Gao} and $K_{Huang(thin)}$ parameters, alongside the boundaries established in the literature [45, 46]. Examining Fig. (4.4a), it is evident that the transition from crown formation to crown splashing is not defined by the $K_{Gao} = 3378$ boundary established by the original author. This can be attributed to the significant differences in film thicknesses between the original work $h_f \approx 0.2 \text{ mm}$ compared to the experiments in this thesis, shown in Tbl. (3.3- 3.6).

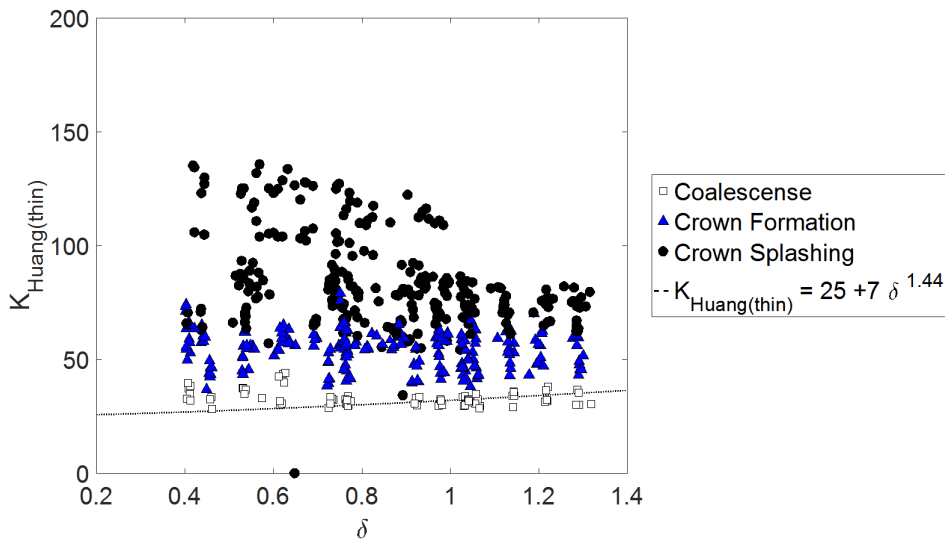
Fig. (4.4b) is somewhat more perplexing, the original paper gave a transition to splashing defined by $K_{Huang(thin)} = 25 + 78^{1.44}$ giving a transition at $K_{Huang(thin)} \approx 550$, which is much higher than the experimental conditions investigated in this thesis. However, this transition value does not correspond with the values plotted on the graph in the original paper, which was referred to this equation. The transition line illustrated on the original figure exhibits a δ dependence, and has values in the range of $K_{Huang(thin)} \approx 25 - 32$. Based on this, it thought that this discrepancy can be attributed to a typographical error, and the actual relationship may be of the form $K_{Huang(thin)} = 25 + 7\delta^{1.44}$. This gives similar values to those in the figure in the original paper.

In this form, the boundary appears close to the transition in the data between coalescence and crown formation. Whereas the original paper from Huang et al. [46] indicates that this is the boundary between coalescence and splashing behaviours. This can be explained as the original work does not specify the criteria which define their *coalescence* and *splashing* regimes. Therefore, it is suggested that the original study used the term *splashing* to refer to both crown formation and crown splashing behaviours.

To conclude, it appears that out of the splashing parameters tested, $K_C(Vd)$ gives the most accurate results for our experimental conditions. However, there may be scope for the application of the K_{Gao} parameter for cases with thinner films than those tested within this thesis.



(a) $K_{Gao} = We \cdot Re^{1/2} (1 + \delta V_f^2) (1 + \delta V_f)^{1/2}$



(b) $K_{Huang(thin)} = (We \cdot Re)^{0.25}$

Figure 4.4: Comparison of experimental data to other derivations of the splashing parameter

Summary of Impingement Outcomes

Within this section, it has been shown that static film boundaries between impingement outcomes are valid for moving films, when the droplet velocity (V_n) is used in the calculation of the splashing parameter K_C . This result has been validated for angles in the range of $0 < \alpha < 30$, however when $\alpha = 40$ the transition point increases from around $K_{C(V_n)} \approx 2100$ to a higher value of $K_{C(V_n)} = 2402$. The various forms of splashing parameter were tested, and for the experimental range investigated in this thesis $K_{C(V_d)}$ was found to offer the most accurate representations of the experimental data.

This information is valuable as it provides conditions under which droplet production does not have to be considered within a CFD program, this allows the modelling of these impingements to be simplified to merely crater and crown dynamics, and omit the modelling of droplet production. Furthermore, if secondary droplet production is desired to be minimised within the bearing chamber, this shows the ideal characteristics of droplets ejected from the bearing; ideally a value of $K_{C(V_d)} < 2100$, meaning small, slow droplets to reduce secondary droplet production.

4.2 Mechanisms of Crown Splashing

Previous studies [8, 9] have outlined different mechanisms of crown splashing, with droplets being produced through *Prompt splashing*, defined as where drops are formed from the advancing crown, at the initial contact between the droplet and the bulk fluid; *Crown Splashing*, where droplets are produced from the crown; and finally *Jet Breakup*, where droplets are formed from the central Worthington jet.

Arising from our study, it is suggested that there are four distinct mechanisms that lead to droplet formation from the crown. These are *Prompt*, *Progressive*, *Recessive*, and *Interstitial* droplet production. The splashing mechanisms categorised here are arrived upon by careful observation of high-speed images. To the authors' best knowledge, the present work is the first attempt to systematically categorize types of secondary droplets resulting from crown splashing. Each of these splashing mechanisms is explained in detail here, elucidating the differences between them, both qualitatively and quantitatively.

Prompt and *Progressive* splashing are depicted in Fig. 4.5, which shows 8 images of a single droplet impact at different times. *Prompt* Splashing (Fig. 4.5a-b) is observed during the *pressure-dominated* regime postulated by Lagubeau et al. [107] and Roisman et al. [42]. This is where the energy of the droplet is in the process of being imparted to the film, generating pressure, which in turn causes the film to accelerate away from the impingement site. Secondary droplets produced during *Prompt* splashing are smaller in diameter and possess greater velocity than those produced by later mechanisms. In our study both diameter and velocity are quantified, and this data is presented later.

Progressive splashing (Fig. 4.5c-h) is defined here as occurring during the crown expansion phase, with droplets being produced from the ligaments of the crown as it expands due to inertia. It is important to understand the differences between prompt and progressive splashing, and these are in the mechanism of production.

Krechetnikov & Homsy [22] suggest that the breakup of the ejecta at early timescales, which produces prompt droplets, is due to Richtmyer-Meshkov instability as the fluid is impulsively accelerated into the air by the impinging droplet. This can be seen in the computational simulations by Haller et al. [108] prompt droplets show vorticity characteristic of Richtmyer-Meshkov 'spikes'. Conversely, ligament formation on the later crown, from which progressive and recessive droplets form, has been attributed to Rayleigh-Plateau or Rayleigh-Taylor instabilities by various authors, [73, 109], with Zhang et al. [23] examining the wavelength of the instability at the rim of the crown, and showing that ligament formation is due to Rayleigh-Plateau instability.

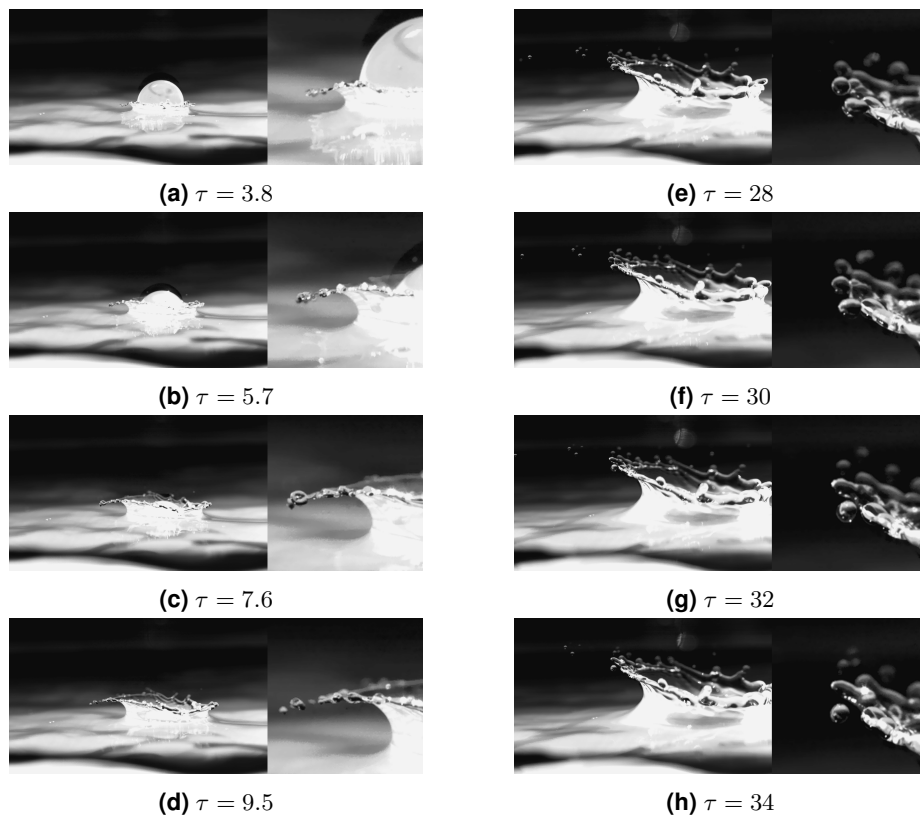
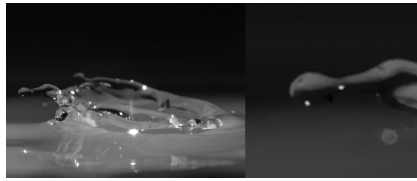
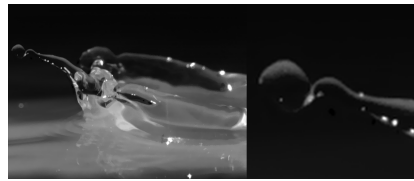


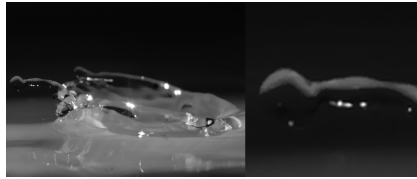
Figure 4.5: Prompt and Progressive crown splashing exhibited during a single impingement at $\delta = 0.87$, $We_d = 442$, $Re_f = 17283$



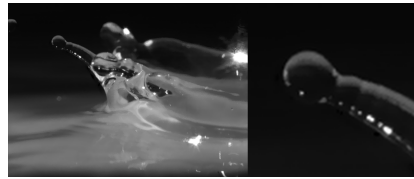
(a) Progressive Splashing at 0.0016 seconds after impingement



(c) Progressive Splashing at 0.0036 seconds after impingement



(b) Progressive Splashing at 0.0020 seconds after impingement



(d) Progressive Splashing at 0.0048 seconds after impingement

Figure 4.6: Surface undulations on a ligament undergoing progressive splashing, at various times after impingement

The detachment of *Progressive* droplets from the ligament is thought to be due to short-wave destabilisation, as outlined by Shinjo et al. [110]. Upon inspection of the ligaments, the characteristic surface undulations are visible along the length, as shown in Fig. (4.6). Within the narrowed regions of the ligament, capillary pressure pushes fluid away from these regions, into the thickened areas. This in turn intensifies the capillary pressure and further promotes ligament breakup and thus the formation of secondary droplets.

The *Recessive* splashing mechanism is shown in the images Fig. 4.7. *Recessive* secondary droplets are formed when the ligament from the crown begins to collapse and recedes, a behaviour first alluded to by Cossali et al. [73]. As the crown begins to withdraw, the ligament base begins to accelerate towards the centre of the crater, however the inertia of the end of the ligament overcomes the surface tension. Hence necking is observed between the end of the ligament and its' base. The withdrawal of the ligament base, coupled with surface tension force within the necked region, cause the tendril of fluid between the ligament-edge and the ligament-base to thin. The surface tension within this thinned region causes an increase in pressure in a manner like that shown for droplet production from the Worthington jet, observed by Castillo-Orozco et al. [111]. This further increases the propensity towards separation. This ultimately results in a large droplet, with low velocity, forming from the tip of the jet. This process is depicted in Fig. 4.7. The droplet is still connected to the crown by a thin ligament of fluid in Fig. 4.7a. However, by Fig. 4.7b the ligament has detached from the droplet due to increased pressure of its narrowed diameter. Furthermore, the ligament is rapidly moving away from

the droplet, towards the centre of the crater. It should be noted that within the course of the experiments in the present study, *Recessive* splashing was only observed on the larger upstream rim of the crater. This is attributed to the difference of crown morphology observed during present study to that of the static film-impact study.

In the past, Rioboo *et al.* [3] observed *Receding Breakup* for impingements upon solid surfaces. Although this is similar in that the breakup is primarily a result of surface tension causing the lamella to retract and form a secondary droplet, there is, however, a key difference in the conditions causing the behaviour. In the case of Rioboo *et al.* [3], receding breakup is caused by part of the lamella of the primary droplet wetting out onto the solid substrate, and being unable to withdraw to the centre due to the counterforce provided as a side effect of this wetting out. Whereas our scenario is more comparable to that of Castillo-Orozco *et al.* [111], with the counterforce being produced by the inertia of the droplet.

Finally, the last category of secondary droplets explored in the present work, here termed *Interstitial droplets* is depicted in Fig. 4.8. *Interstitial droplets* are observed in some cases of *Recessive* splashing when the receding ligament breaks at two instances, causing a small droplet to form at the second instance between the main *Recessive* droplet and the receding ligament. Within the field of capillary jet breakup, Mansour *et al.* [112] described these smaller droplets as *Satellite* droplets, however this term has been used within previous droplet impingement literature to refer to any secondary droplets produced from the crown. Therefore, the term *Interstitial* has been used here to describe these phenomena within the context of this investigation.

During observations of these splashing mechanisms, it was noted anecdotally that each mechanism tended to produce droplets with similar characteristics i.e. size, velocity etc. This is consistent with observations from Cossali *et al.* [8, 73], who observed that *Prompt* splash droplets were typically smaller than those produced through other mechanisms, and droplets formed as the crown recedes are much larger. In our work *Prompt* splash droplets were found to typically be small and fast, whereas droplets produced by *Recessive* splashing were observed to generally be large and slow. Therefore, work was undertaken which is presented in Section 4.3 to determine if a meaningful relationship could be produced between the droplet production mechanism and the secondary droplet characteristics.

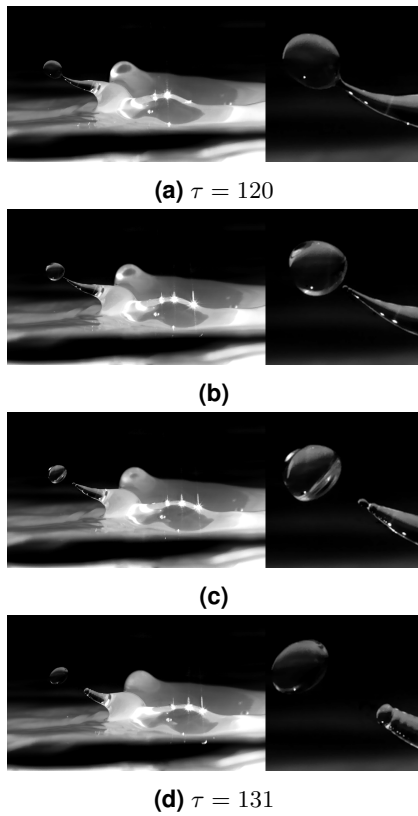


Figure 4.7: Recessive Crown Splashing $\delta = 1.18$, $We_d = 58$, $Re_f = 17283$

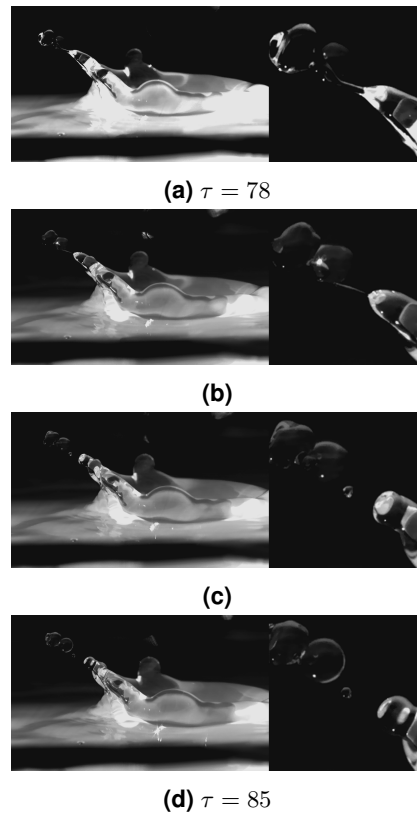


Figure 4.8: Interstitial Droplets formed during Recessive Crown Splashing at $\delta = 0.87$, $We_d = 177$, $Re_f = 17283$

Summary of droplet production mechanisms

Within this section, four distinct mechanisms of droplet production have been described and examples shown. These mechanisms are;

- **Prompt**, caused by Richtmyer-Meshkov instability immediately after the droplet hits the film. Droplets produced are very small and fast.
- **Progressive** caused by short-wave breakup of the ligaments as the crown expands. Produced droplets with medium sizes and velocities.
- **Recessive** caused by the ligament beginning to withdraw, produces very large droplets, with low apparent velocity.
- **Interstitial** similar to satellite droplet production for gravity driven jets, where a thin region of fluid separates at both ends, and forms a small droplet.

Further work will be undertaken in Section [4.3](#) to understand the properties of these secondary droplets.

4.3 Secondary Droplets

Alongside the propensity of droplets towards splashing, and the physical mechanisms of droplet detachment, it is desirable to characterise the splash in a more macroscopic fashion. This allows complete and expensive simulations of droplet impingements within a bearing chamber to be substituted for simplistic and computationally efficient correlations derived from experimental data.

This was undertaken by investigating the number of secondary droplets formed, and the properties of those secondary droplets, and furthermore to investigate the effect of separation mechanism on secondary droplet properties.

4.3.1 Number of Secondary Droplets

Previous work by Okawa et al. [19] has suggested, based on empirical data, that the number of secondary droplets formed from an impingement can be characterised in the form shown in Eqn. (4.3). This was found to be valid for impingement in the range of $0 < \alpha < 50$ for static film experiments. It should be noted that as this correlation was found for normal impingements on static films, where $V_d = V_n$; however follow-up work by Okawa et al. [19] observed that the number of secondary droplets for oblique static film impingements was more accurately modelled by the use of V_n as the characteristic velocity in the calculation of K_C .

At the time of publication, no work has been undertaken which compares this correlation to moving film experiments, and for this correlation to be used to assist in CFD modelling, it is first necessary to validate it for moving-film scenarios. The first step was to determine the appropriate form of velocity to use in the calculation of K_C , both V_d and V_n were plotted, and it was found that V_n provided a much tighter dataset when $K_C(V_n)^{1.8} < 3000000$. This is plotted in Fig. (4.9), the graph shows both single data points, and means with error-bars, error-bars were used where there were at least 8 repeats where the number of secondary droplets and impinging droplet characteristics could be determined accurately, instances where zero droplets were produced were also omitted, to avoid skewing the mean values when within the splashing transition region from Fig. (4.2b). Consideration of the figure shows good agreement with the relationship from Okawa et al. [19] (Eqn. (4.3)). However, when $K_C(V_n)^{1.8} < 3000000$ a distinct deviation from the line is observed.

$$N_{sd} = 7.84 \times 10^{-6} \delta^{0.3} K_C^{1.8} \quad (4.3)$$

This can be understood by consideration of Fig. (4.10a), which shows the splashing on the upstream side of the cavity, this is plotted against the dimen-

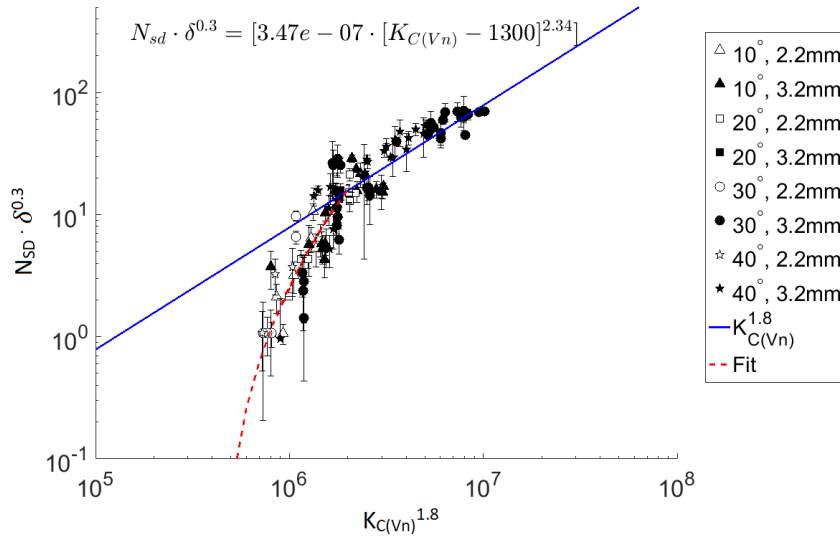


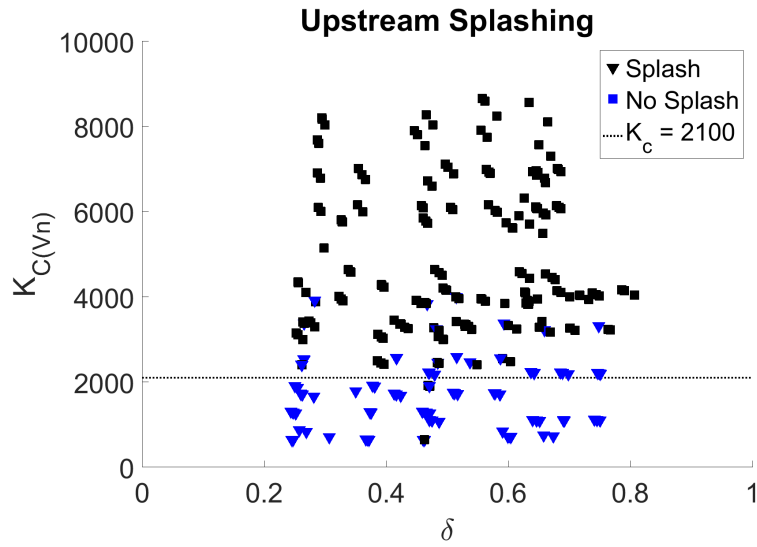
Figure 4.9: Number of secondary droplets against $K_{C(V_n)}$ showing agreement with the $K_{C(V_n)}^{1.8}$ relationship from Okawa et al. [19] at higher values.

sionless film height δ and $K_{C(V_n)}$. From the figure it is evident that on the upstream side, the boundary between no splashing and splashing can be placed around the $K_{C(V_n)} = 2100$ boundary. Conversely if we examine the downstream splashing in Figure. (4.10b) It can be seen that for the majority of cases this transition is at a much higher value, with the value reaching $K_{C(V_n)} \approx 4000$ before consistent splashing behaviours on the downstream side of the cavity is observed. From this it can be concluded that the deviation from the predictions of Okawa et al. [10] below $K_{C(V_n)} \approx 4000$ can be attributed to splashing behaviours only occurring on one side of the cavity, and reducing the total number of droplets formed from the impingement.

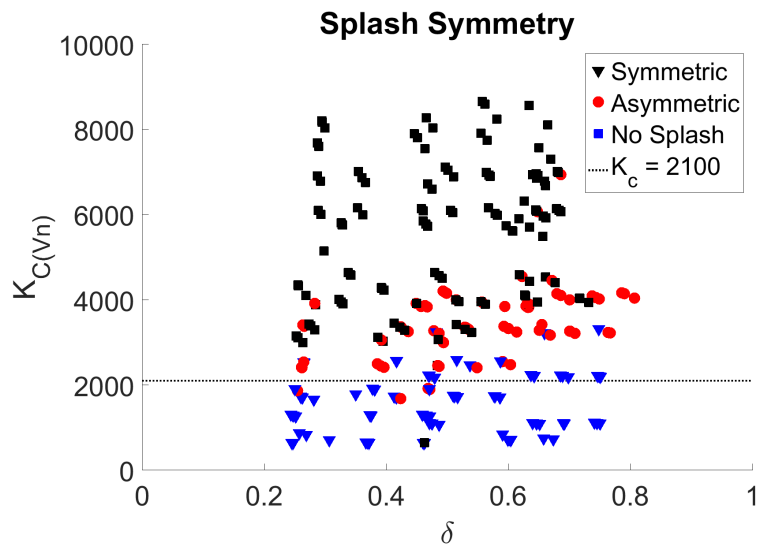
Fig. (4.11), supports the estimation of $K_{C(V_n)} = 4000$ being the boundary between one-side and both-sides splashing, with the statistical analysis giving a point of equal probability at $K_{C(V_n)} = 3969$

Returning to Fig. (4.9), the relationship from Okawa et al. [10] for the number of secondary droplets, Eqn. (4.3), is plotted in blue in Fig. (4.9). As is evident, it matches well with results for higher values of $K_{C(V_n)} > 3 \times 10^6$, although does slightly underestimate compared to our experimental data. This may be attributed to the film motion increasing droplet production on the upstream side of the cavity by enhancing the size of the crown, as observed by Alghoul et al. [17], and allowing more droplets to be produced from this larger crown.

However, as previously noted, for points below $K_{C(V_n)}^{1.8} = 3 \times 10^6$, the agree-



(a) Splashing from the upstream side of the crater



(b) Splashing from the downstream side of the crater

Figure 4.10: $K_{C(Vn)}$ against δ chart for splashing on the upstream and downstream sides of the crown, showing that crown splashing is not observed on both sides until $K_{C(Vn)} = 4000$

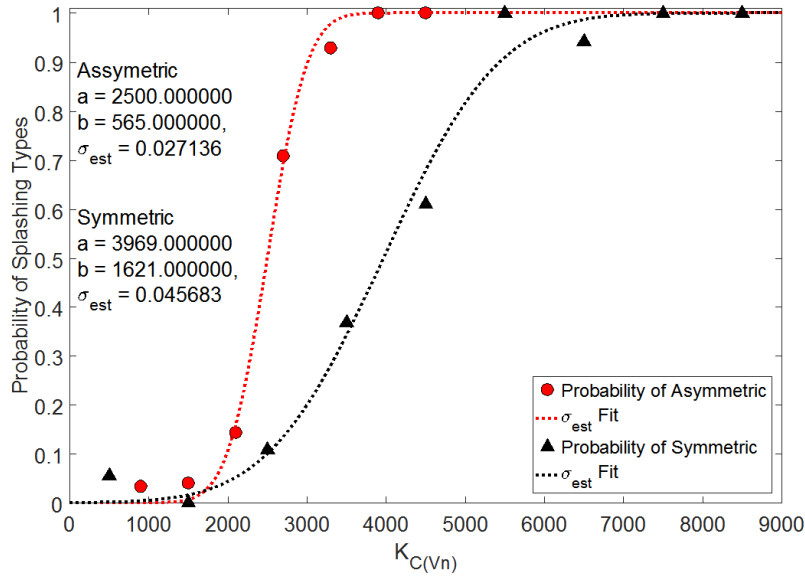


Figure 4.11: Probability of symmetric and asymmetric splashing across the range of $K_{C(V_n)}$

ment begins to deteriorate, therefore a new relationship was required for this low K regime, where splashing may be observed on only a single side of the crown, to accurately describe the number of droplets produced, and provide a correlation for CFD modelling.

Firstly, it was necessary to determine the form of the equation. It was noted that the empirical relationship from Okawa et al. [19] predicted secondary droplet production even for values below the splashing threshold. Considering this situation logically, no droplets should be formed below the point on Fig. (4.2b) where the probability of splashing reached zero ($K_{C(V_n)} = 1300$), it was decided to include this critical value in the equation. Furthermore, as there appeared to be a curve in the $K_{C(V_n)}^{1.8}$ domain, the exponent was set as a variable and fitted. This gave the form shown in Eqn. (4.4).

$$N_{sd} \cdot \delta^{-0.3} = a (K_{C(V_n)} - 1300)^b \tag{4.4}$$

Curve fitting gave empirical values of a and b as 3.47×10^{-7} and 2.34 respectively, and shows a good level of agreement with the data in the low- K regime. Furthermore, this model avoids predicting the production of droplets below the threshold for splashing. Therefore, this empirically derived model can accurately predict the number of secondary droplets within the low- K regime, and may prove useful in future CFD software.

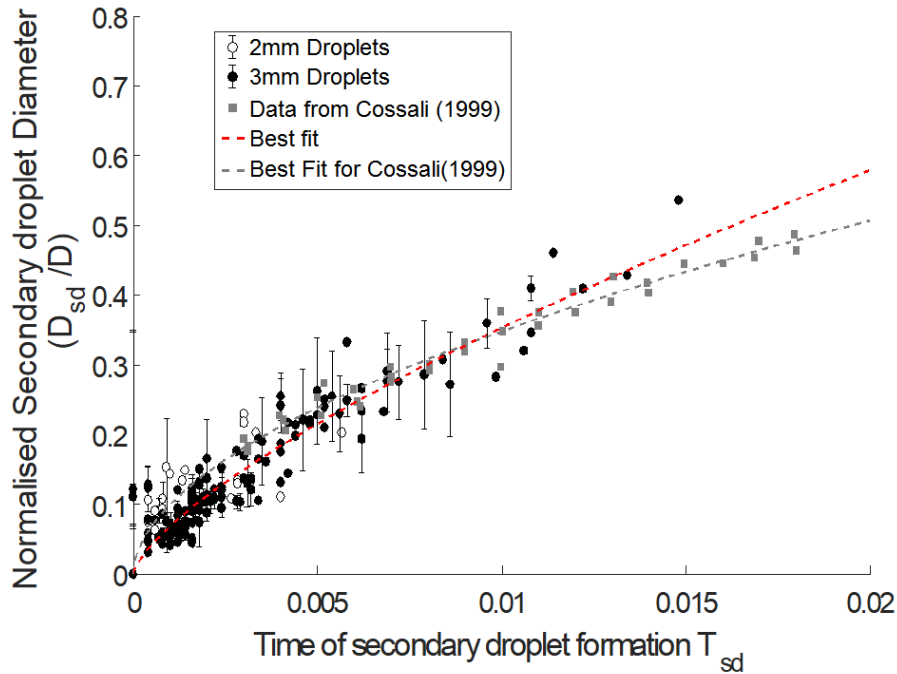


Figure 4.12: Secondary droplet sizes against time of formation compared to the data from Cossali et al. [20]

4.3.2 Secondary Droplet Properties

Alongside the number of droplets produced, to understand the mass transfer within a bearing chamber it is also desirable to characterise their properties. Perhaps the most relevant to bearing chamber conditions out of these properties are the size and speed of the secondary droplets. Previous authors [20, 73] have endeavoured to characterise the droplet size for static films, however it is desirable to experimentally validate these correlations for moving-film impingements. To ensure they provide an accurate representation of moving-film impingement behaviours.

As discussed in more detail in Section 3.4, droplet sizes were determined manually, and the frame recorded to calculate the time of formation (T_{sd}). These values could then be plotted against the results of static film experiments from Cossali et al. [20], as shown in Fig. (4.12). A reasonable level of agreement is shown for lower values of τ_{sd} , with a slight deviation at higher values of τ_{sd} , this is not unanticipated considering the extra kinetic energy of the moving film, and observations literature [17] which observed a larger crown on its upstream side, when compared with static-film work.

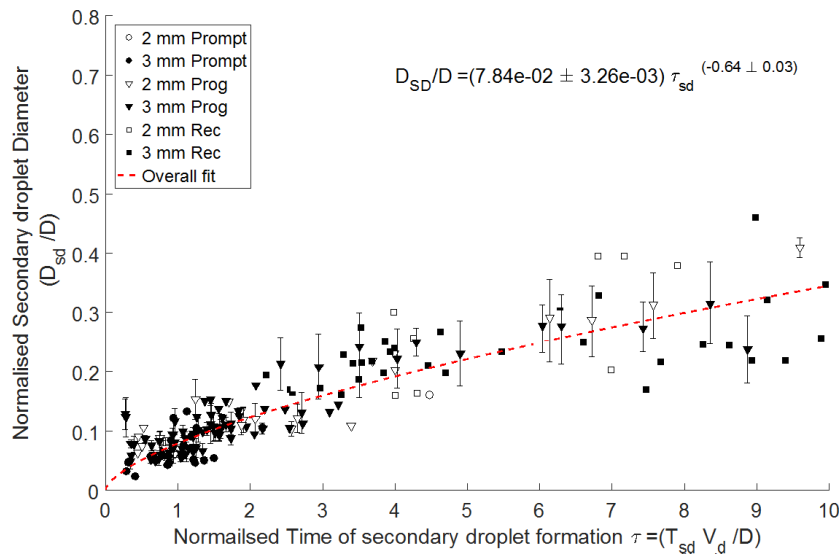


Figure 4.13: Nondimensional size of secondary droplets against dimensionless time of formation separated by splashing type. The line of best fit is described by the equation shown.

Figure. (4.13) plots the dimensionless secondary droplet diameter from our experiments against the time of formation, nondimensionalised in the form $\tau = T_{sd}V_d/D$ with error bars showing 95% confidence intervals. The data is either plotted as individual points, or a mean value with error bars if secondary droplets were observed for 6 out of the 10 repeats performed at each condition. The data is sub-categorised by both impinging droplet diameter and the splashing mechanism. Examining these subcategories, it is immediately obvious that each splashing mechanism populates a certain region of the graph. This shows an overall trend for an increase in droplet diameter, and that prompt droplets are typically only observed at the early time, as suggested from analysis of the inverse bond number by Zhang et al. [23]. Progressive droplets are predominantly within the range of $2 < \tau < 8$. Finally, recessive droplets are observed at the latter end of the timescale, at the transition from crown expansion to contraction.

Examination of the graph also provides quantitative confirmation of the qualitative observations of secondary droplet size. Prompt droplets are the smallest, residing in the range of 0.2 times the diameter of the impinging droplet. Progressive droplets are in the range of 0.1 – 0.3 times the droplet diameter, and recessive droplets being the largest, with typical sizes ranging between 0.2 – 0.4 of the droplet diameter.

For CFD simulations, it is desirable to be able to predict the size of secondary droplets produced from an impingement. Therefore, a curve was fitted

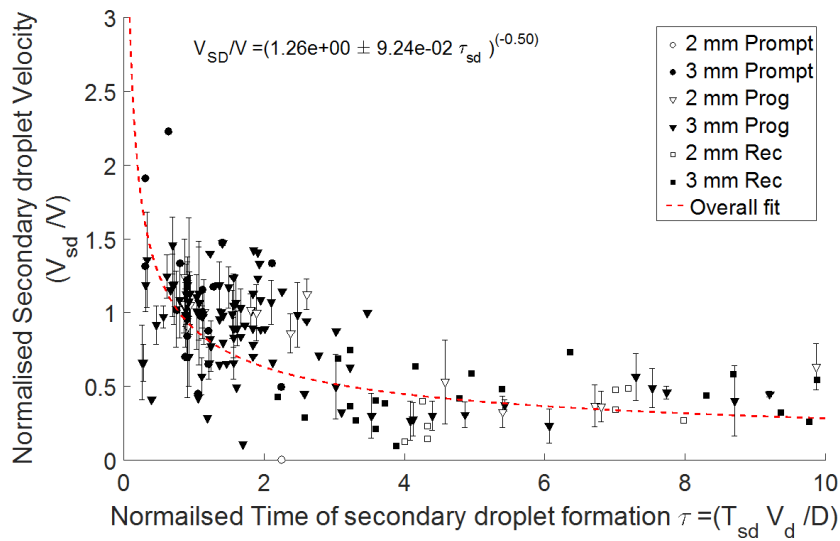


Figure 4.14: Secondary droplet velocity against dimensionless time of formation separated by primary droplet diameter

to the data, based on the form proposed by Cossali et al. [73] for the average secondary droplet size for normal impingements upon static films.

$$\frac{D_{sd}}{D} = a \cdot \tau_{sd}^b \tag{4.5}$$

Through curve fitting to the empirical data, values of a and b were found to be $a = 7.84 \times 10^{-2} \pm 3.26 \times 10^{-3}$ and $b = -0.64 \pm 0.03$ to 95% confidence interval. Examining this fitted curve, it accurately describes the centre of the data spread for the full range of droplet diameters and angles within the experimental range. This provides a useful range of droplet sizes to use in simulations of bearing chambers.

Figure. (4.14) shows a similar graph of dimensionless secondary droplet velocity against dimensionless time of formation. This form of nondimensionalisation was chosen due to previous work from Stow and Hadfield [5].

Previous work [41] has suggested that the crown diameter can be expressed as a function of $\tau^{(0.5)}$. Logically, the secondary droplet velocity should be at least partially related to the speed of crown expansion, so by differentiating this exponent from the position domain in to the velocity domain, we would expect that secondary droplet velocity is likely a function of $\tau^{(-0.5)}$.

Therefore, an attempt was made to curve-fit the velocity of secondary droplets based on the form below:

$$V_{sd}/V_d = (c) \cdot \tau_{sd}^{(-0.5)}$$

and the best fit obtained from our empirical data is:

$$V_{sd}/V_d = (1.26 \pm 0.00924) \cdot \tau_{sd}^{(-0.5)} \quad (4.6)$$

The three types of splashing appear to present a continuous curve, rather than being subdivided granularly into distinct regions, however it is still possible to establish typical velocity ranges for each behaviour. Prompt droplets typically have greater velocity than the primary droplet, with $1 < V/V_{sd} < 2.5$, Progressive droplets have velocities in the range of $0.5 < V/V_{sd} < 1.5$, and recessive droplets have a velocity range of $0 < V/V_{sd} < 1$.

Summary of Droplet Properties

This section has investigated the number of secondary droplets and their sizes and velocities compared to their time of formation. A series of correlations have been derived to this effect, describing the secondary droplet properties for droplet impingements upon moving films for the first time.

The number of secondary droplets formed has been related to the splashing parameter $K_{C(Vn)}$. For higher values ($K_{C(Vn)} > 4000$) a reasonable level of agreement was found with the correlation from static film experiments by Okawa et al. [10]. For lower values, a new curve has been derived, which avoids falsely suggesting droplets were generated below the lower limit of crown splashing. Evidence is presented that suggests this low-K regime is due to splashing behaviours only being observed on one side of the crown.

4.4 Concluding Remarks on Droplet production

This work has shown that impingement outcome transition values for static films are remarkably close to those on moving films, this has been achieved by implementation of statistical methods which are novel in this field.

Four distinct types of crown splashing have been identified and characterised these have also been shown to produce droplets with consistent characteristics, at specific timescales. The quality and size of secondary droplets has been quantified and enhancements have been made to static film models to more accurately represent moving film impingement behaviours.

This supports the CFD modelling of bearing chambers by outlining conditions under which secondary droplets are formed, and then the number, size ranges and velocities of these droplets. This allows greater understanding of the key challenges of bearing chamber design; mist generation, which causes parasitic losses to increase, and of mass transfer between the droplet and the

walls, which has significant implications for cooling and mixing of the oil film on the wall, and in turn affect oil degradation and coking.

Whilst agreement with static film correlations was found for both the splashing boundary, and the number of secondary droplets produced at high values of K , this work has used several novel methods to specifically understand moving-film impingements; including finding a lower limit of splashing, and fitting the splash probability to a cumulative probability curve. This allowing the number of droplets produced for lower values of $K_{C(Vn)}$ to be related to splashing only occurring on one side of the crown.

Chapter 5

Crown and Cavity Development

The production of secondary droplets is an important characteristic of droplet impingements; however, it is desirable to understand the movement of the film and droplet material. In this chapter the development of post-impingement cavities formed from water droplets impinging vertically on water films flowing at an angle of 10° to horizontal and exhibiting supercritical flow behaviours is described. Particular attention is paid to the depth and width of the cavity and crown, as this is likely to affect heat and mass transfer within the bearings. These dimensions are defined in Fig. (2.27).

Furthermore, extensions to an existing analytically derived models are proposed, and the new model is compared to experimental data for validation.

The spreading of droplet material after the impingement will be compared to existing literature for solid surface and static film impingements.

This section investigates:

- Cavity development
- Crown morphology, including the differences upstream and downstream.
- Crown development and modelling both parallel and transverse to the flow (the crown *length* and *width* respectively)
- Crown modelling in the upstream and downstream directions

For the sake of brevity, nominal droplet sizes will be used in the course of this discussion, as defined in section 3.4.2.

5.1 Comparison of BB-LIF and Side-View Data

Before considering the development of the crown and cavity in detail, it is useful to understand how to interpret the BB-LIF images. A sample sequence is shown in Fig. (5.1). As can be seen in Fig. (5.1a), the brighter regions of the BB-LIF image correspond well to the crown formed around the impingement site, whereas darker regions correspond to the cavity under the impingement site.

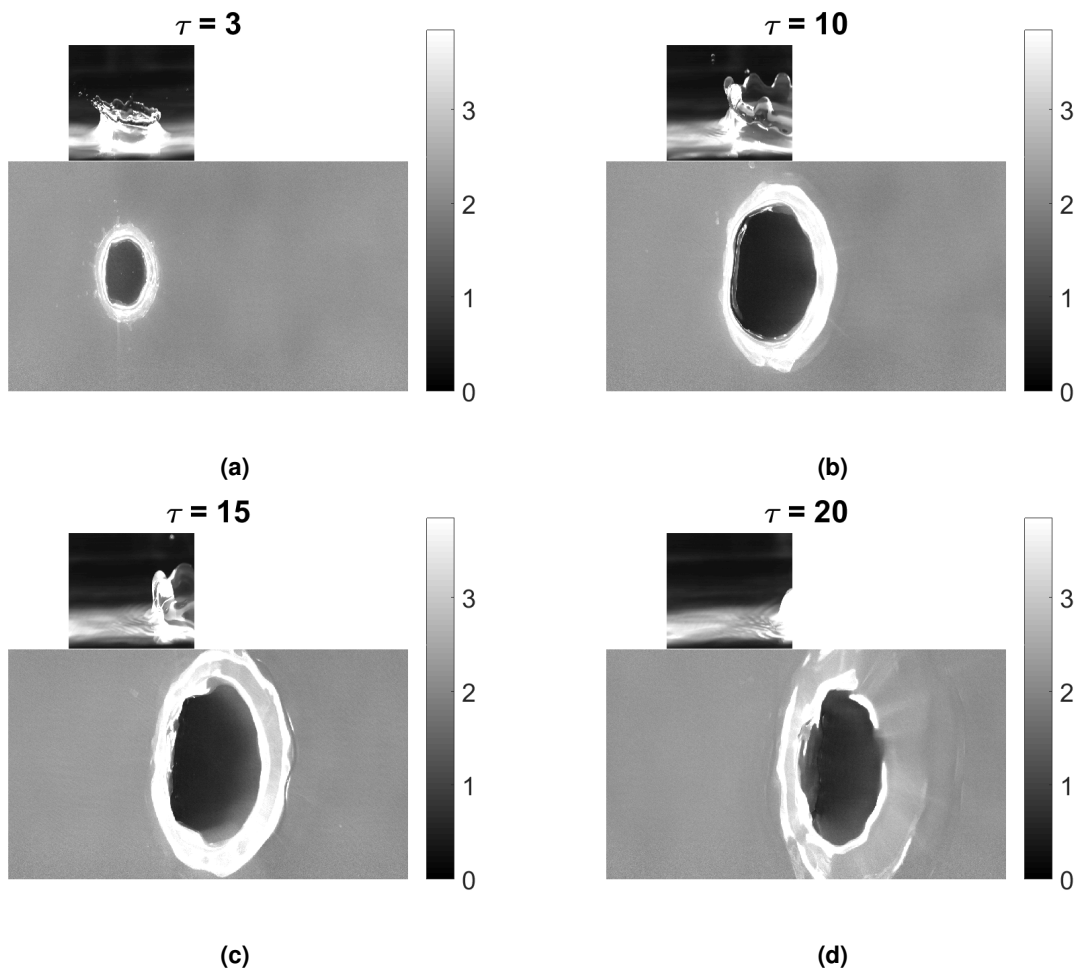


Figure 5.1: Comparison of BB-LIF data to side-view images, Colour-bar showing height in *mm* for the lower (plan view) image

Furthermore, whilst it is possible to create 3D surfaces from this data, the

BB-LIF technique breaks down in areas of high curvature, therefore as shown in Fig. (5.2), the utility of these images is limited, as the crown height is not properly represented. Therefore, whilst it is possible to examine the crater in three dimensions; we cannot accurately measure the height of the crown, and therefore can only investigate the crown diameter. Whilst undoubtedly inconvenient, this behaviour is a well understood limitation of the BB-LIF technique, and has been discussed extensively in prior literature [82, 44, 35].

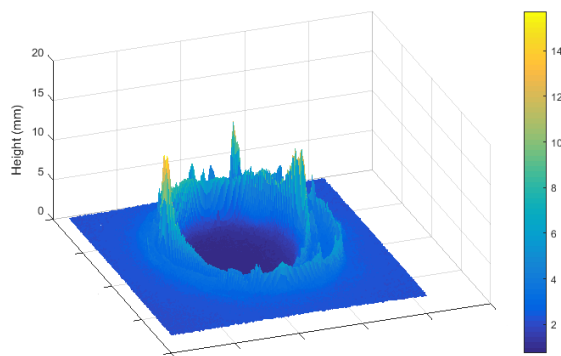


Figure 5.2: Sample 3D image from the BB-LIF data, showing erroneous readings within the crown due to internal reflections. Colour-bar showing height in mm

5.2 Development of Cavity Shape

Droplet production has been shown in previous works [113, 114], to exhibit a dependence on surface roughness and waves. One of the major causes of surface disturbances within bearing chamber wall films is the cavities produced by interactions of previous droplets. Therefore, it is desirable to understand cavity dynamics for impingements on moving films, and the differences between this scenario and static film understanding. As explained within the literature review (2.4.2, 2.4.4), the lifecycle of a cavity for static film impingements is well understood, and several models exist which approximate the cavity diameter for static films. However, it is not clear if these models can be related to impingements upon moving films, where additional factors, such as the momentum and inclination of the film must be accounted for. Therefore, it was decided to undertake an investigation into cavity mechanics using both qualitative and quantitative methods.

5.2.1 Cavity Dynamics

From static film theory, it is anticipated that in the initial stages, the cavity will expand as the droplet inertia is transferred into the fluid. It appears that this behaviour also occurs for droplet impact on moving films.

Figures 5.3 and 5.4 are each two sequences of instantaneous BB-LIF images showing false-coloured height data for droplet impingements at various values of droplet Weber number (We_d), and dimensionless time (τ). Fig. 5.3a-d shows 2 mm droplets at $We_d = 123.7$ and e-h at $We_d = 248.4$. Figure 5.4a-d shows 3 mm droplets at $We_d = 88.9$ and e-h at $We_d = 257.0$. Both sets of images are for the most similar values of δ available within our dataset. Although a δ dependency has been observed within prior literature, this has been shown to have a significantly smaller effect on cavity dynamics than the properties of the impinging droplet [44, 43].

Initial examination shows behaviour very similar to that exhibited by static-

film impingements in that the cavity width increases with time, before collapsing upon itself. Interestingly the larger droplets of Fig. 5.4 produce larger cavities (note that both X and Y in these figures are nondimensionalised against droplet diameter) than the smaller droplets of Fig. 5.3, even when at similar Weber numbers (compare Fig. 5.3e-h to Fig. 5.4e-h). This suggests that the nondimensionalisation of the cavity diameter against droplet diameter does not fully account for the effect of droplet diameter upon cavity expansion. However, examination of Fig. 5.3d,h and Fig. 5.4d,h shows that for each value of Weber number, the cavities are at similar stages of collapse for the same value of τ , this validates for moving films an observation made by Hann et al. [44] for static film impacts, that the time taken for cavity collapse is a function of the droplet Weber number.

Increasing the droplet Weber number increases the collapse time of the cavity no matter the droplet size. This is despite the cavity being larger at larger droplet sizes. This can be seen comparing Fig. 5.3e-h to Fig. 5.4e-h, for higher values of We_d the cavity persists until higher values of τ . For the early stages of the impingement ($\tau = 3$) it is noted that the cavity is very symmetrical in the upstream and downstream directions. This is in the region where the cavity expansion is driven by the pressure or the droplet impact. However, at later values of τ , when the expansion of the cavity is driven by the inertia of the film, a distinct asymmetry is visible in the cavity, for example Fig. 5.3f shows that the cavity is distinctly longer in its X axis, than the Y axis. Furthermore, comparing the footprint of the cavity (blue) and the crown (red), most cases show the crown extending further away from the centre of the cavity in the downstream direction (right), than in the upstream direction (left).

In the initial stages of cavity development, shortly after the pressure-dominated regime, minimal waviness is observed on the rim of the cavity. However, as τ increases, the outside edge of the cavity appears much less consistent, particularly for the larger droplets, at high values of We_d .

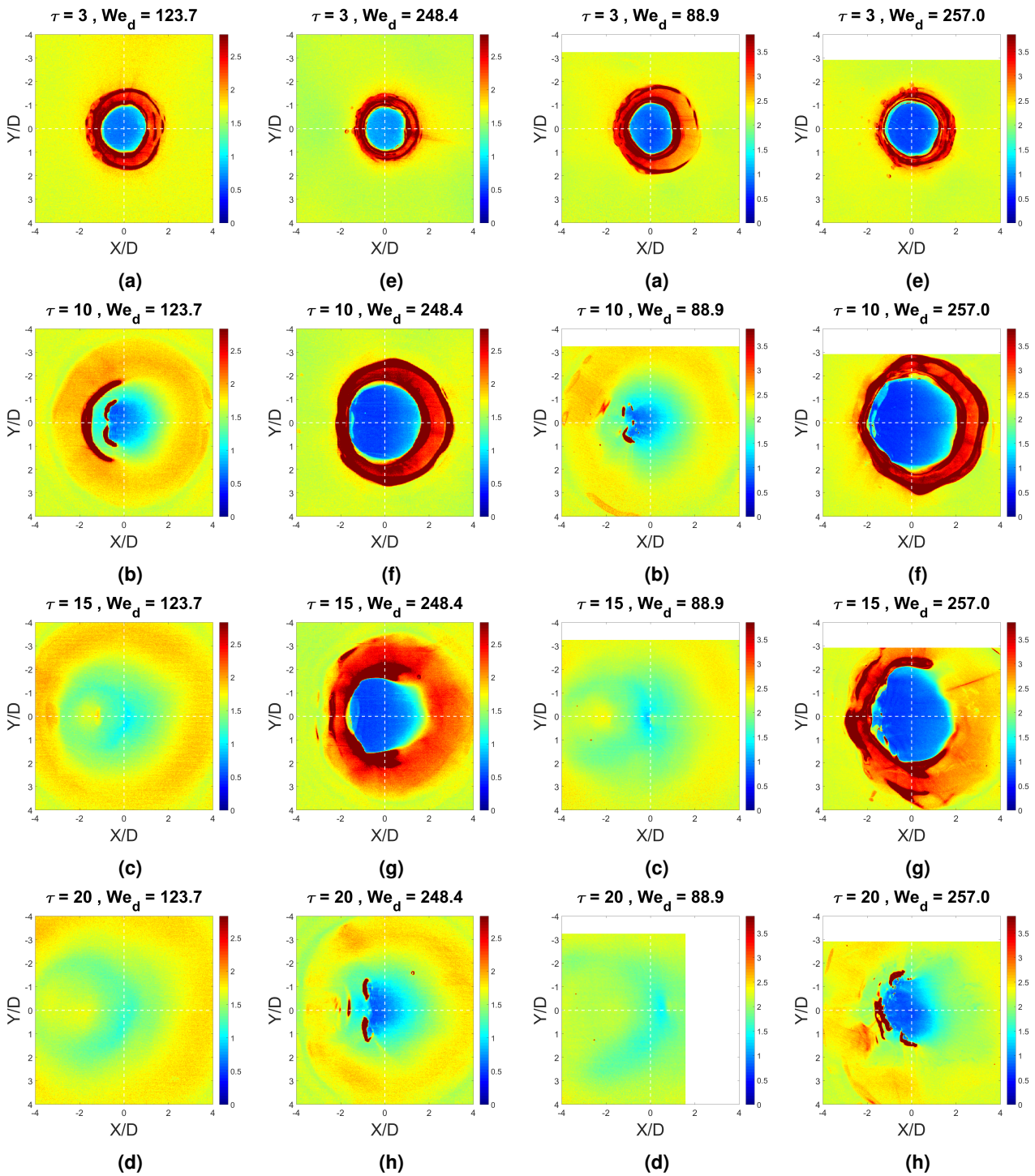


Figure 5.3: 2 mm Droplet Impingements, $\delta = 0.75$. **Figure 5.4:** 3 mm Droplet Impingements, $\delta = 0.71$. Colour-bar showing height in mm

Examining the base of the cavity, the consistency of the blue colour, for example in Figs. 5.3g, 5.4g shows that there is flattening of the base, similar to that observed by Macklin and Hobbs [63]. However looking at the downstream side of this flat region, for example in Figs. 5.3g, 5.4g typically the curvature is much less severe than on the upstream side, suggesting that the film motion or inclination is having an effect on the cavity collapse. A side profile of a cavity, showing these wall-effects is shown in Fig. (5.5)

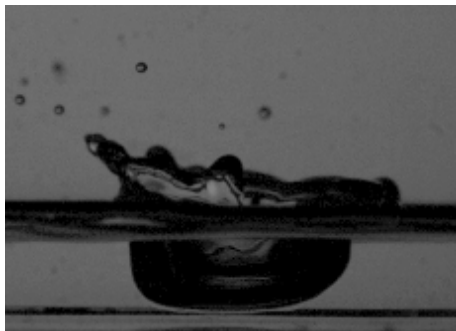


Figure 5.5: Side profile of cavity, exhibiting flattening as it approaches the base of the channel

5.2.2 Cavity Development

Previous authors have shown [115, 116, 117, 113] that the surface roughness and presence of waves on the target surface has a distinct effect upon the production of droplets. Within a bearing chamber, it is expected that the cavities formed from previous impingements will be one of the major causes (alongside the shearing airflow) of surface undulations on the wall-film. As droplet production is understood to be a major cause of parasitic losses caused from the bearing, greater understanding of cavity propagation is desired to support bearing chamber design and optimisation. Therefore, it is desirable to understand the development to the cavity with time. Although previous authors have postulated models for static films, no attempts have been made to validate these for moving film impingements.

As it was desired to measure the width of the cavity, it was decided that a

method to visualise the cavity development like that used by Hann et al. [44]. To this end, the Width-Time diagrams shown in Figs. (5.6, 5.7) were created. These figures were created by taking a single column of pixels from the centre of the cavity from each frame. These columns could then be composited together to give an image showing the of the cavity width against time. The extent of the cavity could be determined by manipulating and scaling this image.

The model from Roisman et al. [42],

$$\Omega = \sqrt{\beta(\tau - \tau_0) - f(\tau - \tau_0)}$$

is plotted. This model relates the cavity growth and recession to an expansion term (β) and a retraction term (f) shown in Eqn. (2.23), relative to the dimensionless timescale $\tau = tV_d/D$. Throughout the literature, several forms for expansion term (β) have been proposed, within the figure, the original derivation of $\beta_{rois} = 0.62\delta^{0.33}$, is shown in black. And the derivation from Hann et al. [44] of $\beta_{Hann} = 3.1 \cdot We_h^{-0.37} + 0.19$, is shown in white.

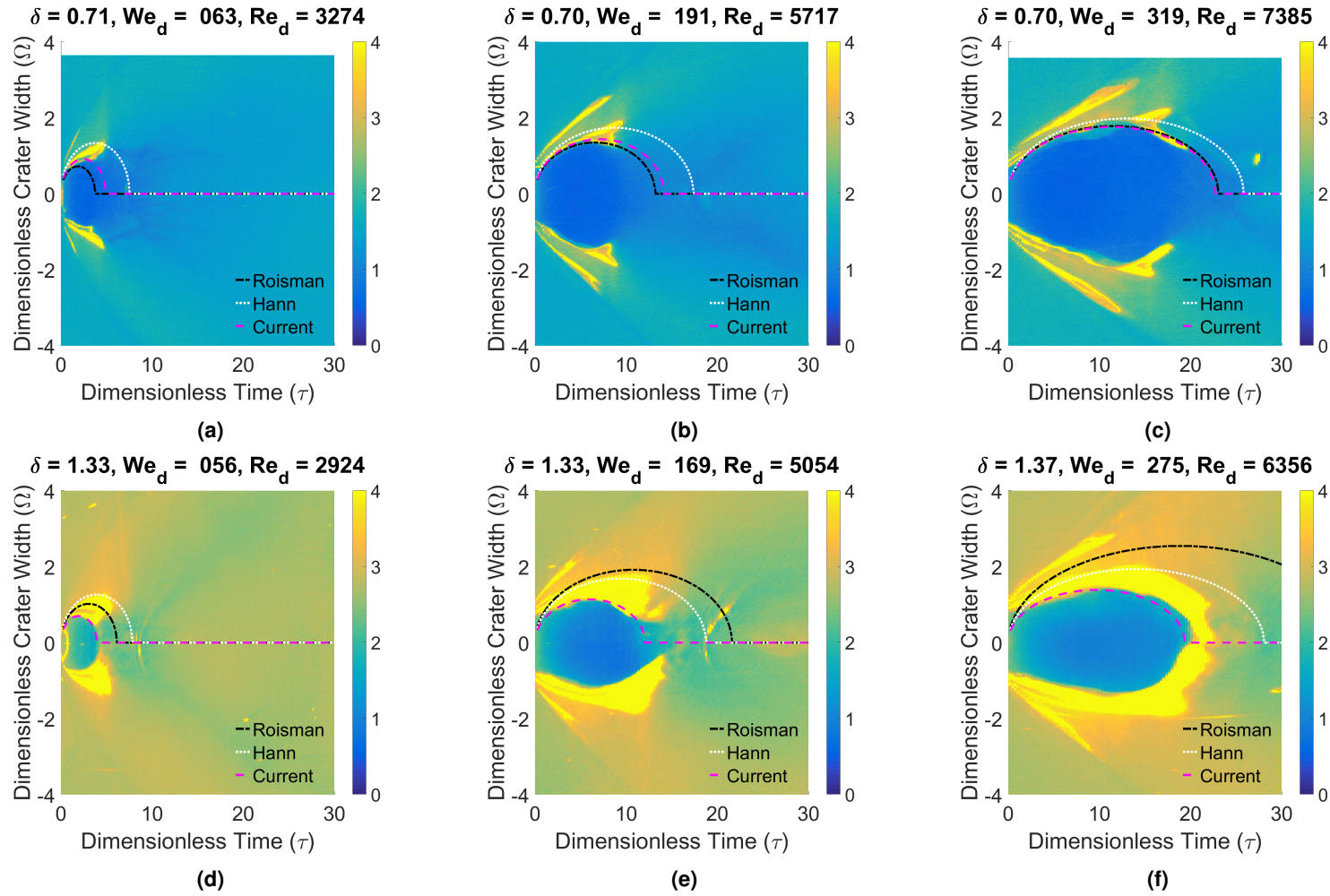


Figure 5.6: 2 mm Droplet XT diagrams when $\beta = We_d^{-0.13}/\sqrt{\delta}$. Colour-bar showing height in mm

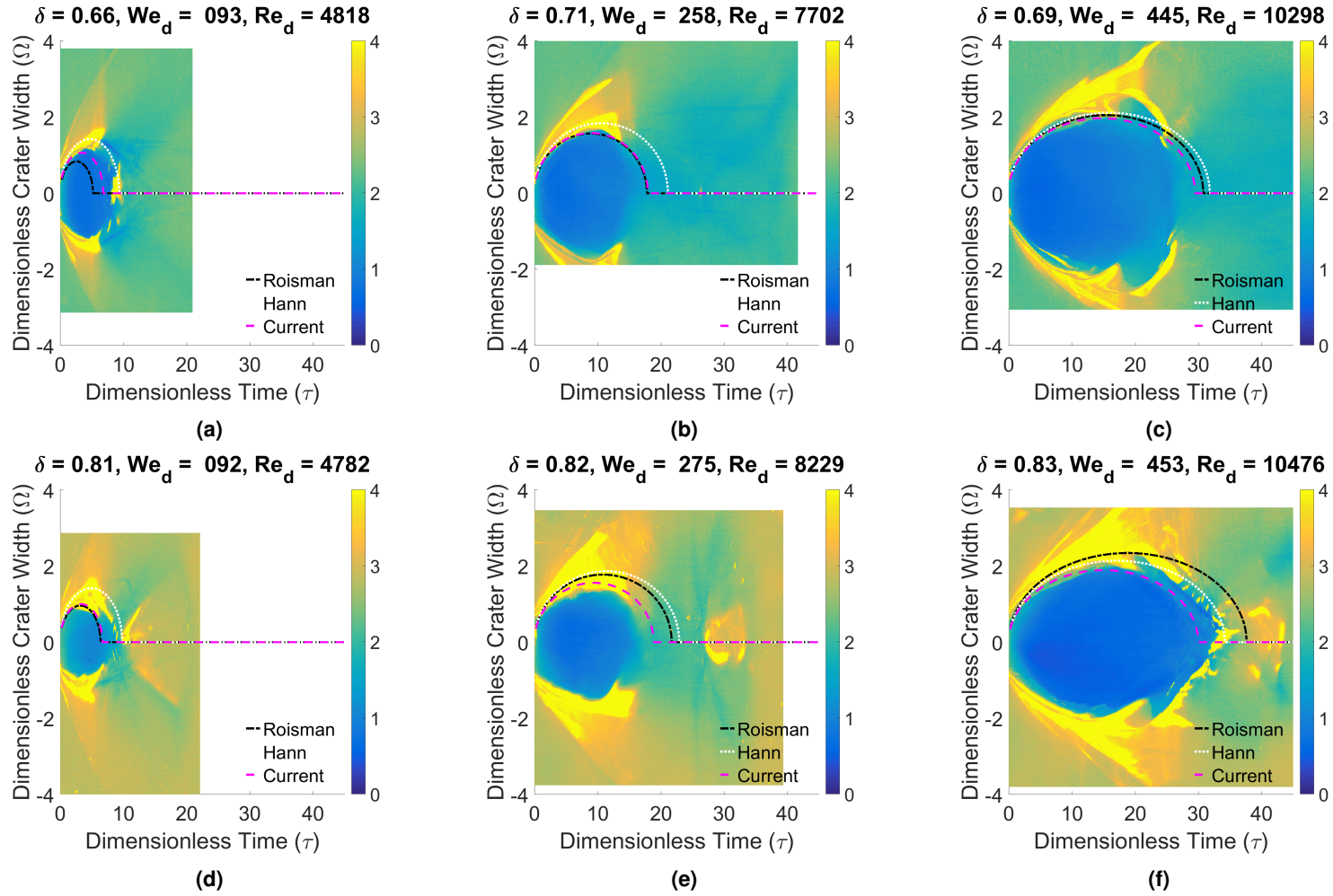


Figure 5.7: 3 mm Droplet XT diagrams when $\beta = We_d^{-0.13}/\sqrt{\delta}$. Colour-bar showing height in mm

Comparing these models with the extent of the crater (*in blue*), it is evident that both derivations provide a reasonable fit for the 3 mm droplets of Fig. (5.7) for the higher Weber number experiments. However, these models begin to deteriorate for both the lowest Weber number impingements with 3 mm droplets. Furthermore, most of the experiments with 2 mm droplets show a poor fit with either of these two relationships. This can be attributed to both experiments only using one droplet size for impingements conducted with distilled water.

Since the primary droplet sizes chosen by both Roisman et al. (3 mm) and Hann et al. (3.5 mm) correspond well to the size of our 3 mm droplet, the accuracy of their predictions is unsurprising. However, the deviation for 2 mm droplets suggests either a previously uncharacterised dependency on droplet diameter, or a mischaracterisation of the Weber number dependence which becomes more evident for lower values of We_d . It is also reasonable to expect some dependency on the ratio of droplet Weber number to dimensionless film height, as for thin films the cavity will begin to experience wall effects as it approaches the base of the channel.

Therefore, a need for a new relationship between the experimental parameters and the contraction term (β) is required. Therefore, the crater widths were determined using thresholding, and then the β values determined using curve fitting. These values could then be plotted against key nondimensional groups related to the impingement; previous works [43, 44, 42] have suggested that β is related to both the properties of the impinging droplet, and the base film, and can be expressed as a function of the We_d & δ . Therefore, initially it was decided to plot in β against We_d , as shown in Fig. (5.8). From this several factors are evident;

- β is inversely proportional to We_d
- There is an undefined dependence on film height
- There is an undefined dependence on droplet diameter

The dependencies on film height and primary droplet diameter may be ac-

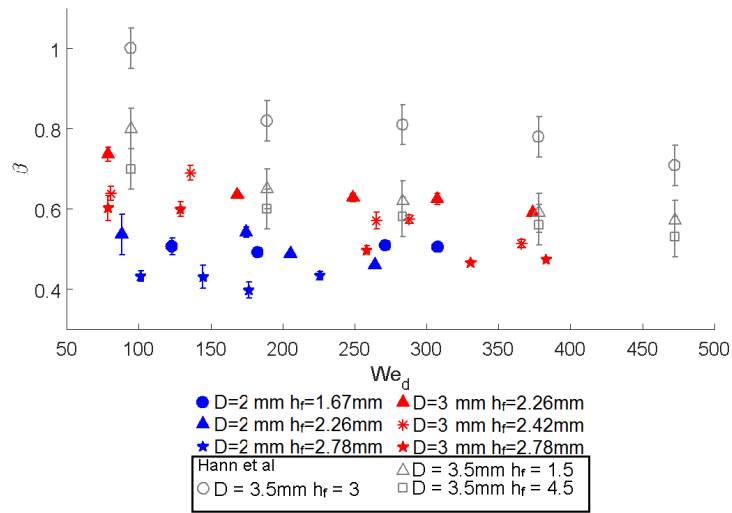


Figure 5.8: Cavity width expansion coefficient (β) compared to droplet Weber number We_d

counted for by using dimensionless film height (δ). This approach has been proposed by Van Hinsberg et al. [43] in the form $\beta_{Hinsberg} = \left(\frac{23.3}{We_d} + 0.5\right) \delta^{-0.33}$ and by Hann et al. in the form $\beta_{Hann} = 3.1 \cdot We_h^{-0.37} + 0.19$. In the case Hann et al., We_h is defined as $We_h = We_d \cdot \delta$. This gives Fig. (5.9), which shows a distinct dependency on droplet diameter and film height within the datasets, which is not suitably nondimensionalised by this form. Therefore, it was decided to separate the components of We_h , into We_d and δ with the aim of finding a relationship with better performance across the range of droplet diameters and film heights.

This resulted in Fig. (5.10), which plots We_d against $\beta \cdot \sqrt{\delta}$. Whilst previous authors have proposed that β is a function of We_d , droplet diameter, and H_f , there is no established consensus on the correct form of this relationship. The relationship proposed on this work was found by optimising to give the highest R^2 value to the fit. Evaluating this from a physical perspective, the dependence upon We_d is well founded in the literature [42, 44, 43], and the dependence on δ is due wall effects caused by the channels base influencing the cavity development. This relationship seems to nondimensionalise well for droplet diameter, and reasonably well for film height. In this form, three curves were

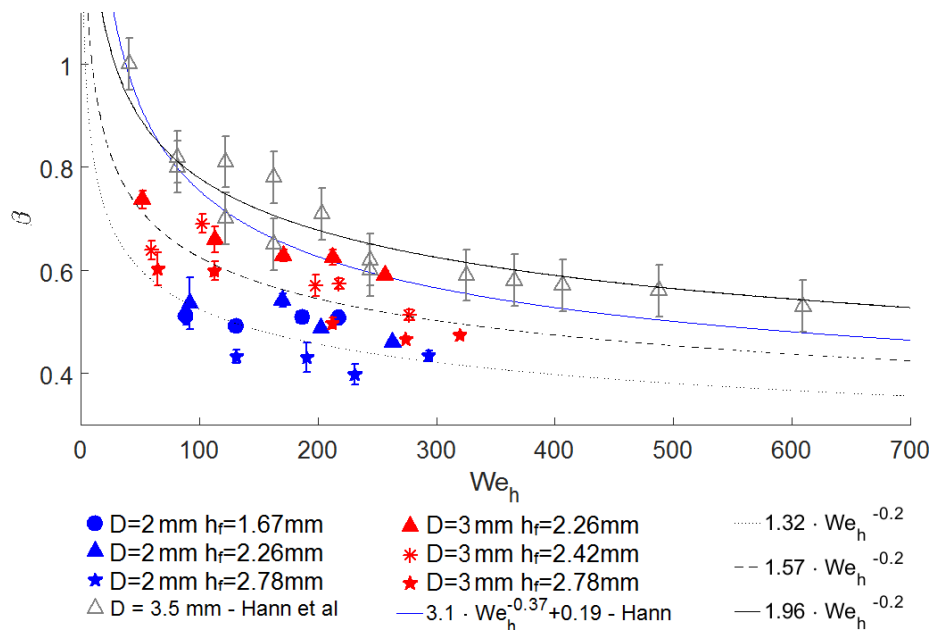


Figure 5.9: We_h against β . showing multiple datasets, and an unresolved dependence on primary droplet diameter (D) and film height (h_f)

fitted, for each individual droplet diameter, as well as the entire dataset. Initially the fit was performed in the form $\beta \cdot \sqrt{\delta} = a \cdot We_d^b$. However, this showed the values of a for each droplet diameter to both be within 95% confidence intervals of 1.

Fitting for $\beta \cdot \sqrt{\delta} = We_d^b$ gave values for the exponent, b , for each droplet diameter (2 mm and 3 mm) almost within 95% confidence intervals of each other (-0.137 ± 0.019 , -0.128 ± 0.019). Indicating a reasonable nondimensionalisation for the two droplet diameters. Therefore, the average of these was taken and the form of β shown in Eqn. (5.1) is proposed;

$$\beta_{Mitchell} = \frac{\sqrt{\delta}}{We_d^{0.132}} \tag{5.1}$$

This form shows a dependence on both the impinging droplet properties (We_d) and the dimensionless film thickness δ . Whilst this form was chosen by analysis of the empirical data, rather than analytical consideration of the problem, it is preceded by the work of Van Hinsberg [43], who also related β

to We_d and δ . The dependence on We_d is obvious, relating the cavity dynamics to the velocity and kinetic energy of the impinging droplet.

However, the dependence on δ is somewhat more complex. It is suggested that this dependence reflects a rough approximation of the wall effects interfering with the cavity expansion; and that for impingements on thinner films, the cavity is unable to expand downwards fully, causing localised pressure build-up which redirects the cavity expansion sideways, in a manner reminiscent of a droplet impinging upon a solid surface. All these aspects change the ratio of expansion and contraction forces acting upon the cavity, and hence their inclusion in β . The final advantage of this form is that it is shown within the present study to accurately model the impingement of droplets of varying diameters.

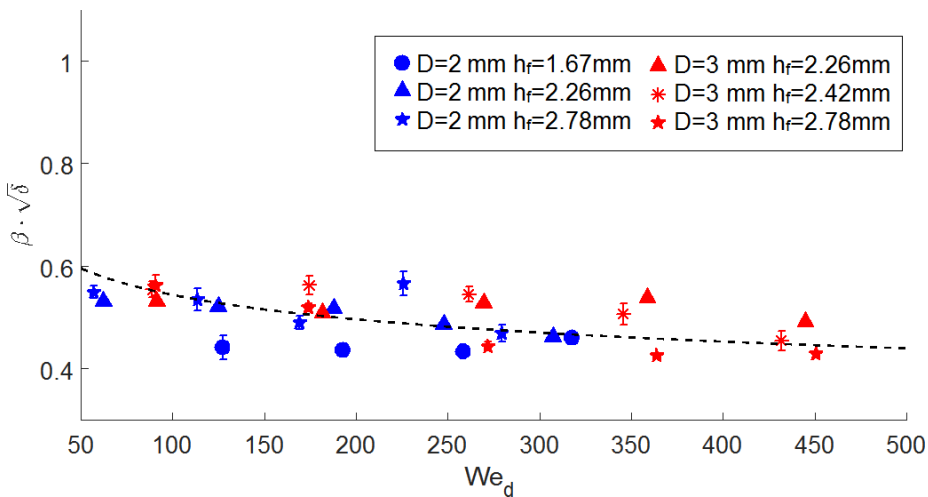


Figure 5.10: We_d against $\beta \cdot \sqrt{\delta}$, showing collapse onto a single line for the values of β from moving film experiments

Plotting the Roisman et al [42] model with $\beta_{Mitchell}$ in Figs. (5.6, 5.7), shows a reasonably accurate prediction of both the 2 mm and 3 mm droplets across the full range of Weber numbers. Although when we examine performance across the range of δ values, we do see slight deterioration at the highest values of δ . Overall, an increase in accuracy is observed for the experimental range compared to both previous models, and specifically an improvement in the prediction of cavity dynamics with 2 mm droplets compared to previous

models.

Examining our correlations, β_{rois} typically over-predicts for higher values of dimensionless film height (δ), and β_{hann} often over-predicts at low values of δ . However, this new form seems less sensitive to variations in δ , and provides a more accurate representation across the range of film heights compared to these previous models.

5.2.3 Droplet Spreading

Oil degradation within an aero-engine is a major cost occurred by airlines. Whilst it is necessary to provide correct lubrication and cooling, to ensure a high level of reliability, it is also desirable to reduce capital and environmental burdens occurred by the frequent replacement and disposal of aero-engine lubrication. Repeated heating and cooling cycles are understood to be one of the main causes of oil degradation within bearing chambers. As the cool droplets impinge on the hot film, it is desirable to understand the interfacial area, which is a key parameter in heat transfer between the two objects. Therefore, it is desirable to understand the spreading of droplet material within the cavity as this allows insight into the mixing and heat transfer between the droplet and film.

Previous authors [44] have suggested that the spreading of droplets within the cavity for static films can be modelled using the solid surface impingement model from Roisman et al. [6] as shown below:

$$h_L = \frac{\eta}{(\tau + \tau_i)^2} \exp \left[-\frac{6\eta r^2}{(\tau + \tau_i)^2} \right]$$

Where:

- h_L is the height of the lamella
- η is a constant estimated as $\eta = 0.39$ by Roisman et al. [6]
- t is time
- τ is the inverse of the initial gradient of the radial velocity estimated as $\tau_i = 00.25$ by Roisman et al. [6]
- r is the radial location.

Therefore, the extent of the droplet spread is plotted against the Roisman model in Figs. (5.11, 5.12). Examining these figures, it is evident that the Roisman model provides a reasonable description of the droplet spread in the early timescale until $\tau = 2.5$. After this stage there is significantly more variance in

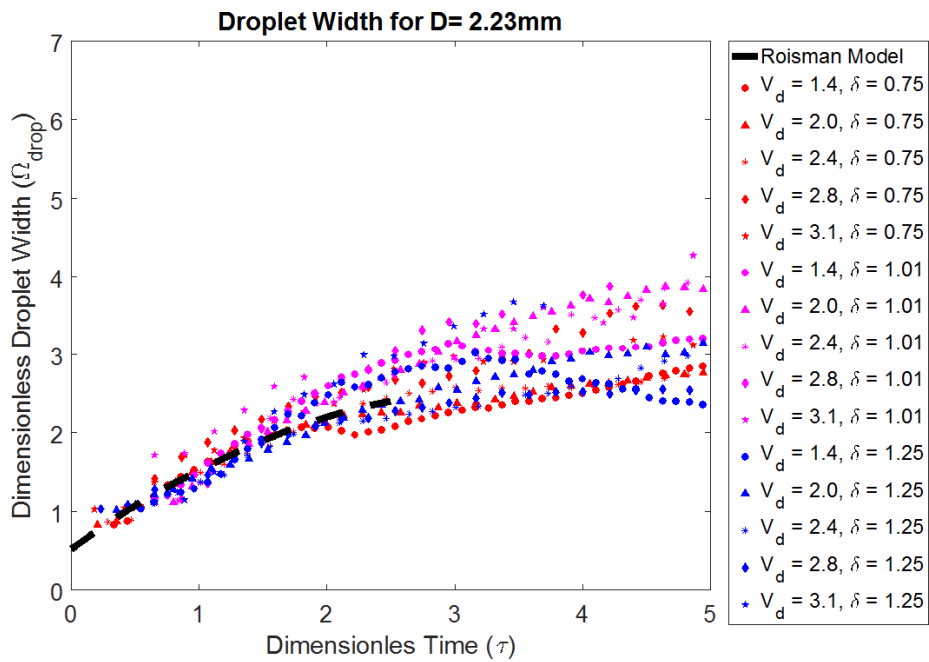


Figure 5.11: Droplet Spreading within the cavity against the model from Roisman et al. [6] for $D = 2 \text{ mm}$

the spread. It is suggested that after this time period, the spread of droplet material is more driven by the cavity drag on the droplet material.

This shows a high level of comparability between droplet impingements on solid surfaces, static films, and moving films. And validation of the Roisman et al. [6] model as an early-time solution for droplets spreading on moving films. This provides useful insight which will aid in CFD heat transfer simulation within the bearing chamber.

Alongside the droplet spreading, it was observed that interfacial mixing between the droplet and film could be seen within some of the images. As can be seen in Fig. (5.13), at later timescales, tendrils of fluid are visible upstream of the cavity, indicating mixing in the slower-moving layers of film close to the base. This is anticipated, as comparison of the values of Re_d and We_d to the regime map from Agbaglah et al. [29] [reproduced as Fig. (2.33)] places our experiments firmly within the vortex shedding regime. This indicates that the LIF technique could be appropriate for investigating the conditions under which

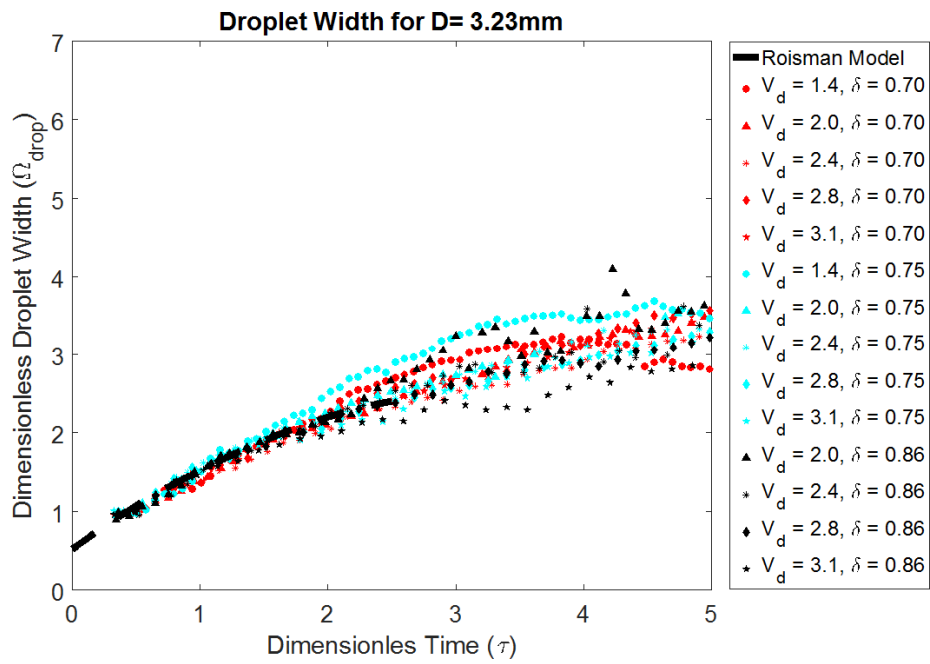


Figure 5.12: Droplet Spreading within the cavity against the model from Roisman et al. [6] for $D = 3 \text{ mm}$

mixing occurs in a future study.

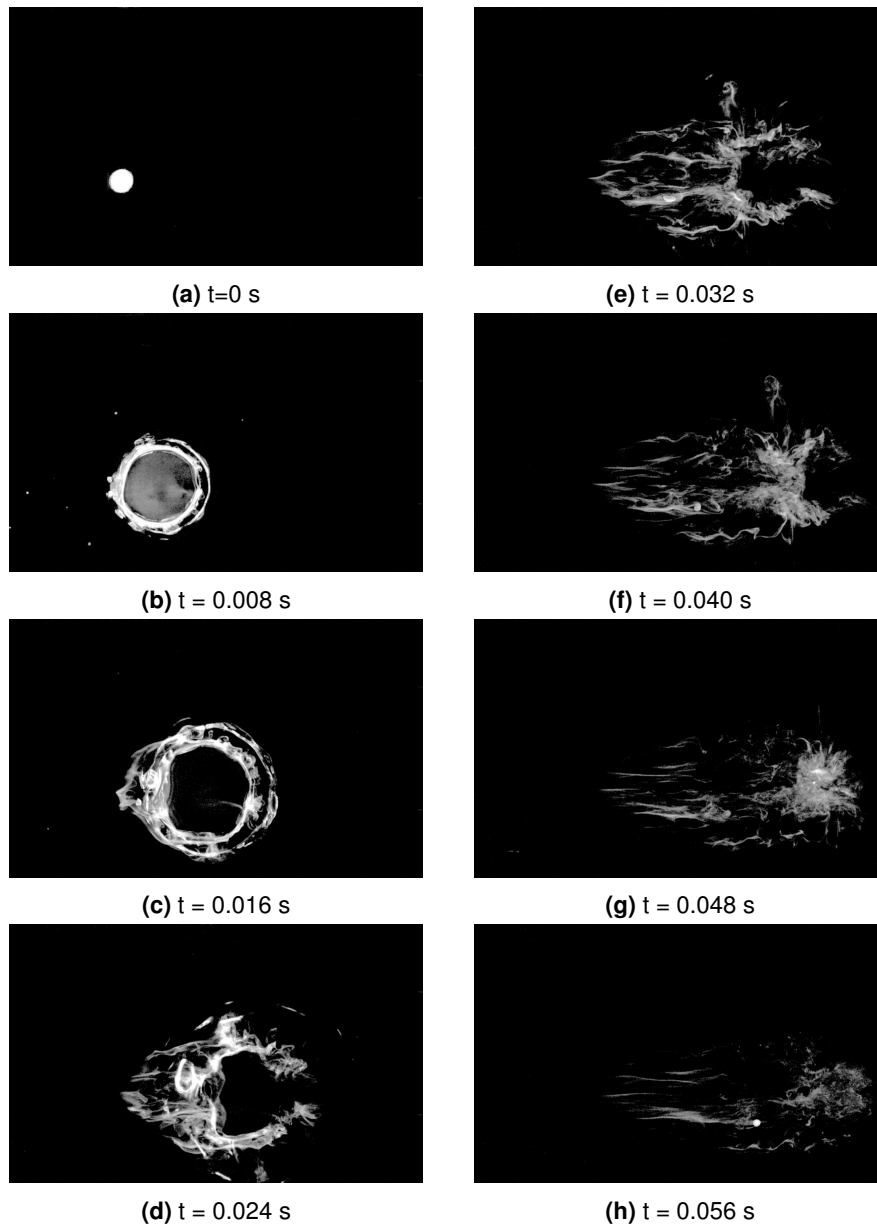


Figure 5.13: Dye-trails indicating interfacial mixing between the droplet and film

5.3 Crown Development

Within the highly rotating environment of a bearing chamber, strong shearing airflows have been previously shown [118] to be a major cause of droplet production from the film. As droplet impingements and their resultant structures are not immune to these shear forces [72], there is concern that these may be a mechanism of oil atomisation. Atomised oil is a key aspect in parasitic windage losses, and pollutant emission. Therefore, an understanding of crown development is key in tuning bearing chamber design to minimise these issues.

Previous literature [19] has shown that the crown is asymmetrical when the droplet impinges at an angle, furthermore early moving film experimentation [17] has also observed uneven crown production. This section describes crown morphology and its relationship to the ratio between film speed and the component of droplet velocity parallel to the flow. Furthermore, development of the crown with time is investigated in directions parallel and normal to the film flow, and compared various against models for static and moving films.

5.3.1 Crown Morphology

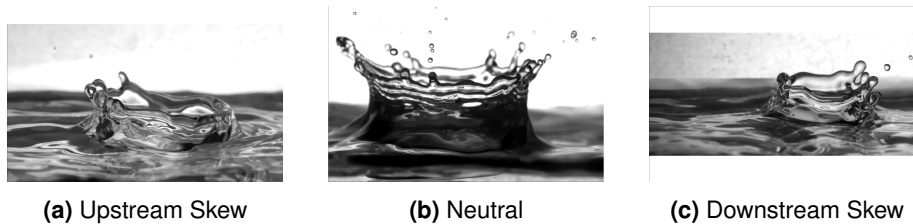


Figure 5.14: Types of Crown Skew (*film flowing left to right*)

Examination of the crown morphology revealed that the crown seemed to tend towards three different shapes, as shown in Fig. (5.14): **a** shows the crown being significantly enhanced on the upstream direction, **b** shows the crown developing evenly on both sides, and finally **c** shows the crown being larger and forming droplets on the downstream side. This is consistent with existing literature; Okawa et al. [10] observed crown-enhancement on the upstream

side. These experiments were performed on near horizontal films, with a very slow rate of movement. Conversely, Che et al. [119] investigated impacts on highly inclined and fast-moving films. This resulted in the downstream side of the crater being enhanced, rather than the upstream. Before discussing this, it is useful to develop a nomenclature for the various velocity components, these are shown in Fig. (5.15). V_d is the absolute droplet velocity, and V_f is the absolute film velocity relative to the high-speed camera. V_n is the droplet velocity component in the plane perpendicular to the film, and V_t is the droplet velocity component in the plane parallel to the film.

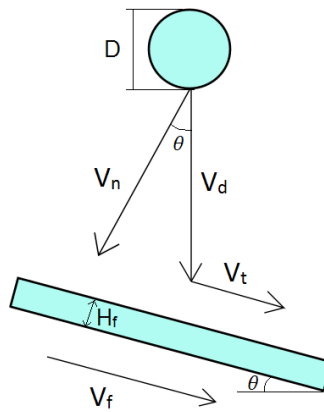


Figure 5.15: Diagram showing velocity components between the film and droplet

Due to the conflicting reports of crown skew in the existing literature, it was decided that further investigation was warranted. We started with Fig. (5.16), which figure compares the crown skew, determined by the maximum crown rim height on the upstream and downstream sides, against the film velocity, and the droplet velocity parallel to the film, calculated as $V_t = V_d \cdot \sin(\theta)$.

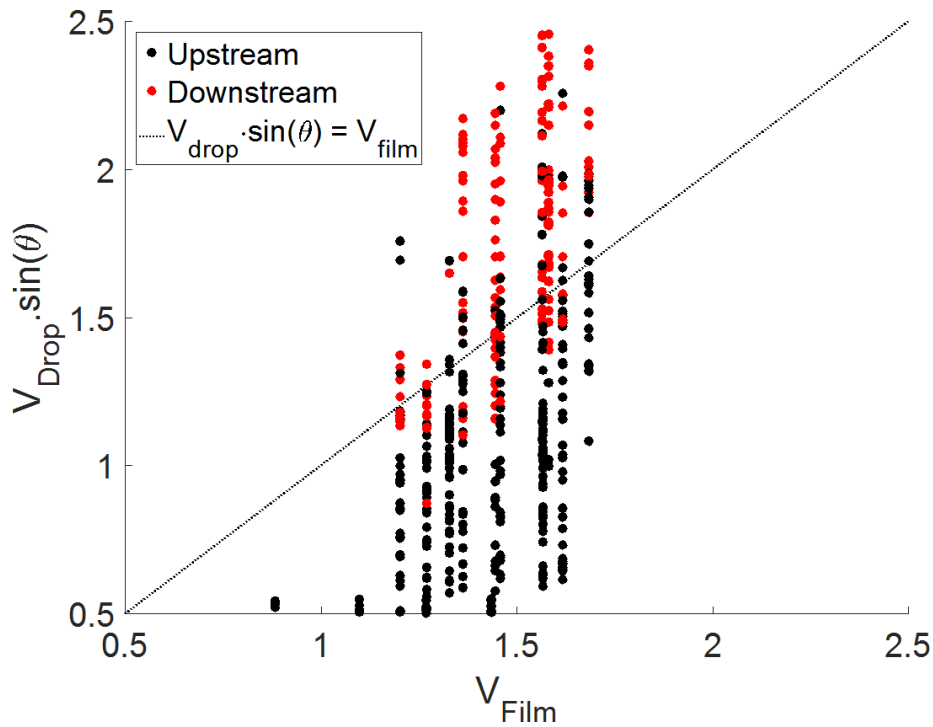


Figure 5.16: Upstream and Downstream splashing plotted against the ratio of droplet and film velocities

Examining Fig. (5.16), it appears that the transition between upstream and downstream splashing is reasonably demarcated by the point where the V_f is equal to the $V_d \cdot \sin(\theta)$. This is not unexpected, as this correlates to the relative velocity between the droplet and the film, in the plane parallel to the film being equal to zero. This also explains the occurrence of symmetric crowns, occasionally observed when $V_{Film} \approx V_D \cdot \sin(\theta)$, as from the perspective of the film, the droplet is impinging normally with no relative transverse velocity.

Fig. (5.17), shows the transition between upstream and downstream skew. This is created using similar principles to those in Fig. (4.2). The probability is calculated by dividing the $V_f/[V_d \cdot \sin(\theta)]$ domain into increments of 0.2, and calculating the probability of downstream skew within each increment. A curve, as described by Eqn. (5.2), could then be fitted to the data using the curve fitting toolbox in MATLAB. In this equation, CPF is a cumulative probability function, V_f and V_d are film and droplet velocity respectively, and a and b are

fitting constants.

Examining the results, we find that the point where curve is centred (denoted by a in the figure) is at $V_f/[V_d \cdot \sin(\theta)] = 1.02$, and that $V_f/[V_d \cdot \sin(\theta)] = 1$ is within the standard error of estimate for the fit. Therefore, this indicates that the point of equal probability for either an upstream or downstream outcome is when V_f and $(V_d \cdot \sin\theta)$ are almost exactly the same, and supports the view that the transition between each behaviour is primarily dependent on the ratio of V_f and $(V_d \cdot \sin\theta)$.

$$P(\text{outcome}) = CPF \left(\frac{([V_f/(V_d \cdot \sin\theta)] - a)}{b} \right) \tag{5.2}$$

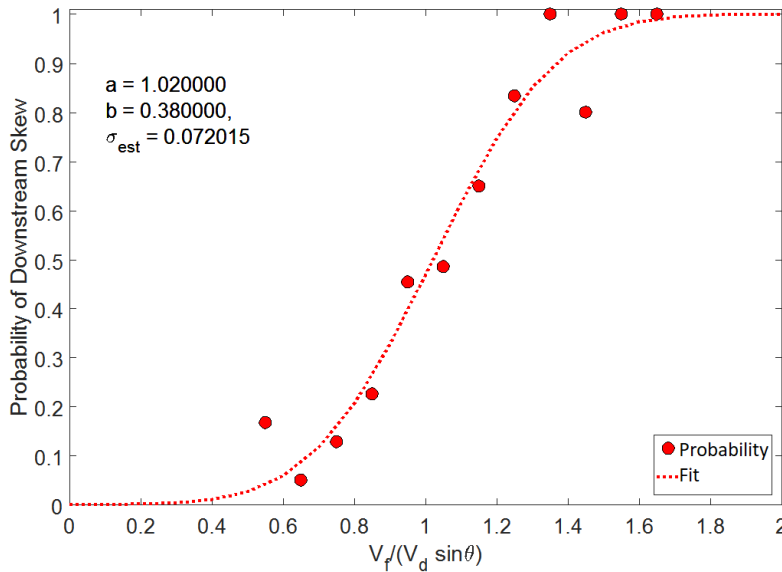


Figure 5.17: Probability of upstream and downstream splashing plotted against the ratio of droplet and film velocities

Maximum Crown Size

When making comparisons to static film studies, it is important to remember that the crowns observed in this study are largely asymmetrical. Whilst previ-

ous works have typically expressed the dimensionless crown radius as R_c^* , for this study, we will divide this into two components; the length from the centre of the cavity to the crown-rim in the direction of film flow will be identified as ξ_l , and in the direction transverse to the flow, the width, the distance from the centre of the cavity to the crown-rim will be denoted by ξ_w .

Figure. (5.18) shows the maximum crown radius against the droplet Reynolds number. From this a linear increase with Re_d is observed until $Re_d = 7500$ at this point the maximum width begins to deviate from this linear pattern and level off. This is made apparent by the line, fitted to all values below $Re_d = 7500$. This gives an expression for maximum crown width, shown in Eqn. (5.3).

$$\xi_{w(max)} = 3.63 \times 10^{-4} \cdot Re_d + 0.243 : \text{for } Re_d < 7500 \tag{5.3}$$

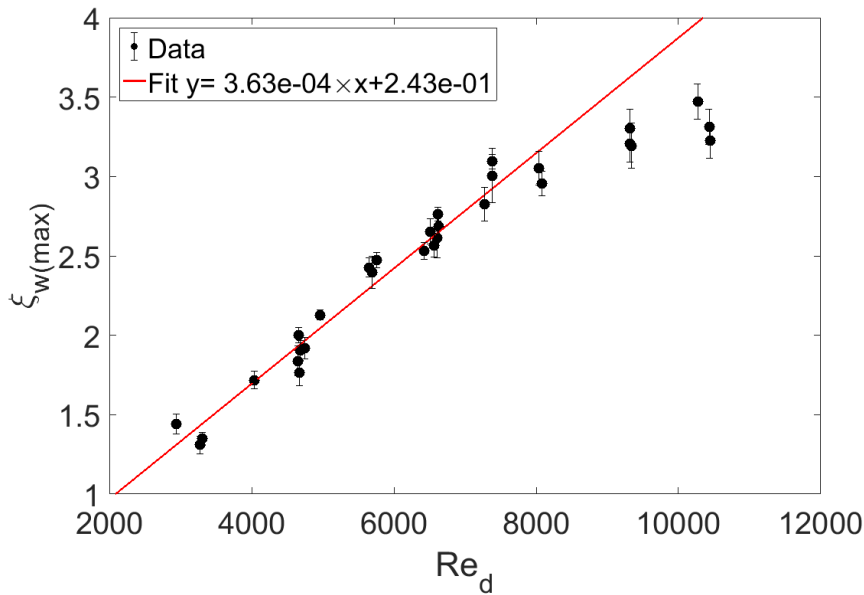


Figure 5.18: Maximum Crown width against Re_d

One suggestion to explain this behaviour is that above $Re_d = 7500$, is the crown height is increasing with Re_d rather than the width, and this height increase eventually results in the bubbling behaviours such as those observed by

Worthington [4]. An example of this is seen in Fig. (5.19). **a** shows a wide, low crown at $Re_d = 5998$, however **b** shows a crown with only a marginal increase in length, but a dramatic increase in height as Re_d increases over the 7500 value. However, more work is required to fully understand this phenomenon.

The observed correlation for crown width allows easy approximation of the affected area of film in CFD simulations by relating the maximum crown size to the impinging droplet characteristics.

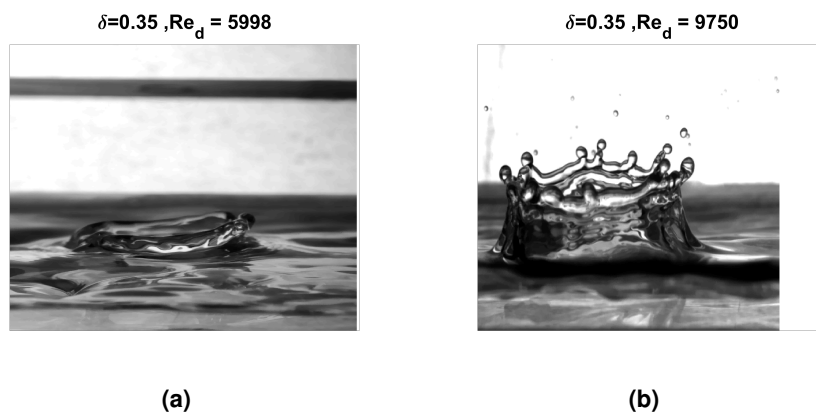


Figure 5.19: Comparison of crown heights at $Re_d = 5998$ and $Re_d = 9750$

5.3.2 Crown Modelling

The ability to accurately model the crown will allow simplification of complex CFD modelling, reducing computational expense and design turn-around times, leading to a faster design cycle. This is advantageous in a highly competitive and tightly legislated environment such as aero-engine production.

Whilst we have previously stated that the crown of a moving film cannot be considered as a radius, due to its asymmetrical nature, we can still compare the crown length and width to radius models from static film literature. This allows us to determine if current understanding can accurately represent moving film impingements across a range of experimental conditions. However, to achieve this, we must first define our terminology and assumptions. Firstly, measurements of the dimensionless crown distance have been taken from the centroid of the cavity, determined as the median coordinate of the thresholded image. A new coordinate system is shown in Fig. (5.20). We assume that, in the direction across the flow (the width) the crown is symmetrical, such that $Width = 2 \cdot \xi_w$. However, in the direction parallel to the flow (length), the asymmetry of the cavity must be considered, therefore the length is evaluated to be the sum of the upstream and downstream components, $Length = \xi_{l,u} + \xi_{l,d}$. When discussing correlations from literature, R_c^* will be used to denote correlations from static film literature, and ξ when discussing new modifications.

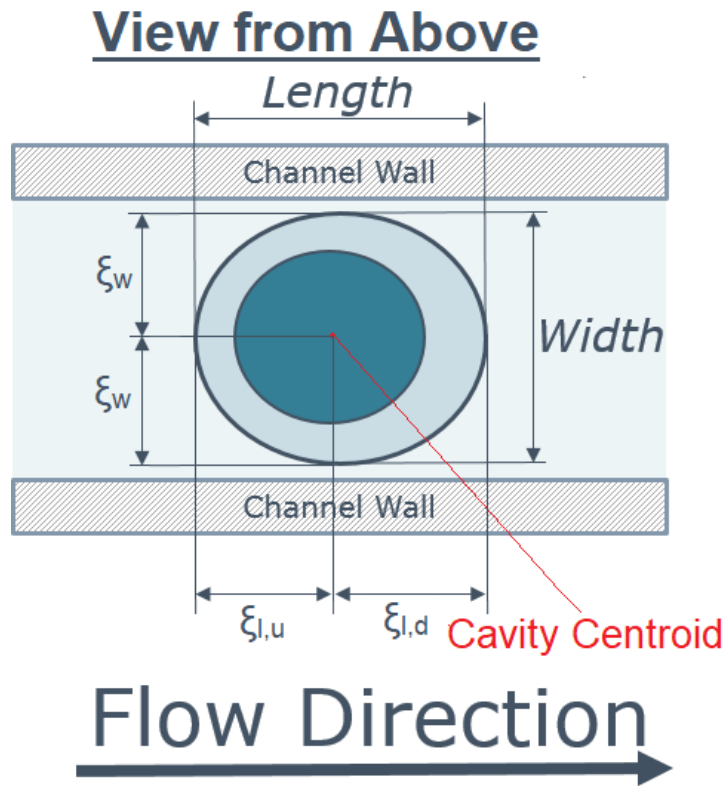


Figure 5.20: Crown Schematic

Modelling of Crown Width

For static films, Roisman et al. [41] suggest the crown diameter may be expressed as:

$$R_c^* = \left[\left(\frac{3\delta}{2} \right)^{-1/4} \times \sqrt{(\tau + \tau_0)} \right]$$

where: R_c^* is the dimensionless crown distance, τ is dimensionless time, δ is the dimensionless film thickness and τ_0 is a dimensionless constant based on the film height, and $\tau_0 = (1/\sqrt{24\delta}) - 1$.

Furthermore, for moving films, Gao et al. [45] proposed the form shown in Eqn. (2.16).

$$R_c^* = \beta_{gao} \sqrt{\tau} + \frac{1}{\sqrt{6\delta}} - \left(\frac{1}{3\delta} - \frac{1}{\sqrt{6\delta}} \right)^{1/2}$$

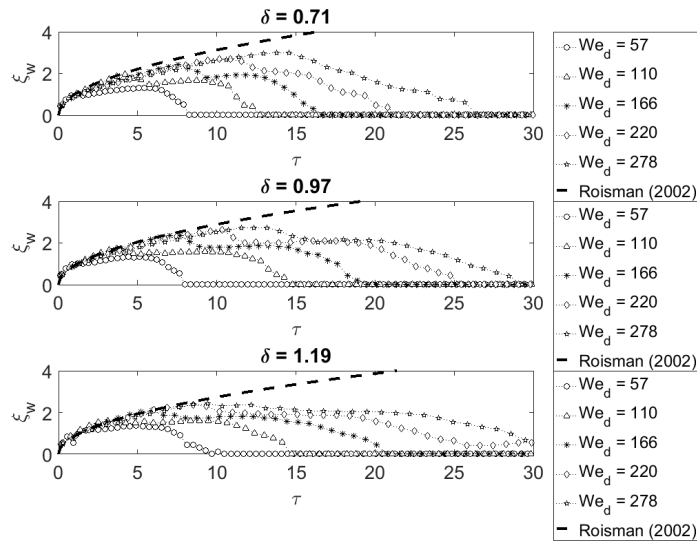
$$\beta_{gao} = \left(\frac{2\lambda^2}{3\delta} \right)^{1/4}$$

$$\lambda = \frac{0.53}{Re_d^{-0.02} \times We_d^{0.03} \times \bar{U}_f^{-0.26} \times \delta^{0.12}}$$

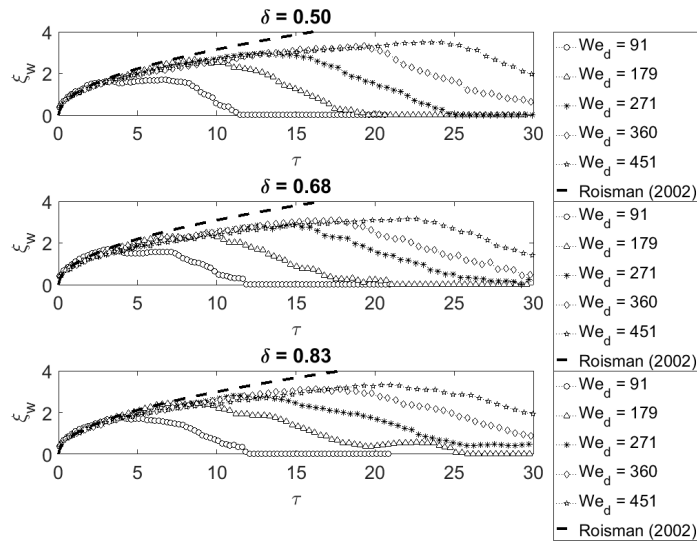
where:

- R_c^* is the dimensionless crown distance ($\bar{r}_c = r_c/D$)
- τ is the dimensionless time ($\tau = tU/D$)
- \bar{U}_f is the velocity ratio (Film Velocity/Droplet Velocity)
- δ is the dimensionless film thickness (h_f/D)

Figure. (5.21) Shows the development of the crown width against the analytical static film model from Roisman et al. [41]. It was found that for the width, the crown expanded identically in each direction, which one would expect, considering that this direction is perpendicular to the film's momentum. Initial examination shows a reasonable correlation against the experimental data in the early time period, for both impinging droplet diameters. However, as time goes on more deviation is noted, especially at higher values of We_d . From this it was suggested that the 3/2 constant in Eqn. (2.15) could be changed by fitting to the conditions to more accurately model the cavity width.



(a) 3 mm impinging droplets



(b) 3 mm impinging droplets

Figure 5.21: Crown propagation against the model from Roisman et al. [41]

To develop this model, the value of the $3/2$ term is set to a variable as shown in Eqn. (5.4), and fitted using the inbuilt curve fitting functions in MATLAB. From this it was found through analysis of the empirical data that the values could be expressed by a straight line when nondimensionalised in the form We_d/δ , shown in Fig. (5.22). A curve was then fit using native Matlab curve fitting, giving Eqn. (5.5). It should be noted that the lowest values of We_d have been omitted due to the lack of crown formation at these conditions.

$$\xi_w = (a \cdot \delta)^{-1/4} \cdot \sqrt{\tau + 1/\sqrt{24 \cdot \delta} - 1} \tag{5.4}$$

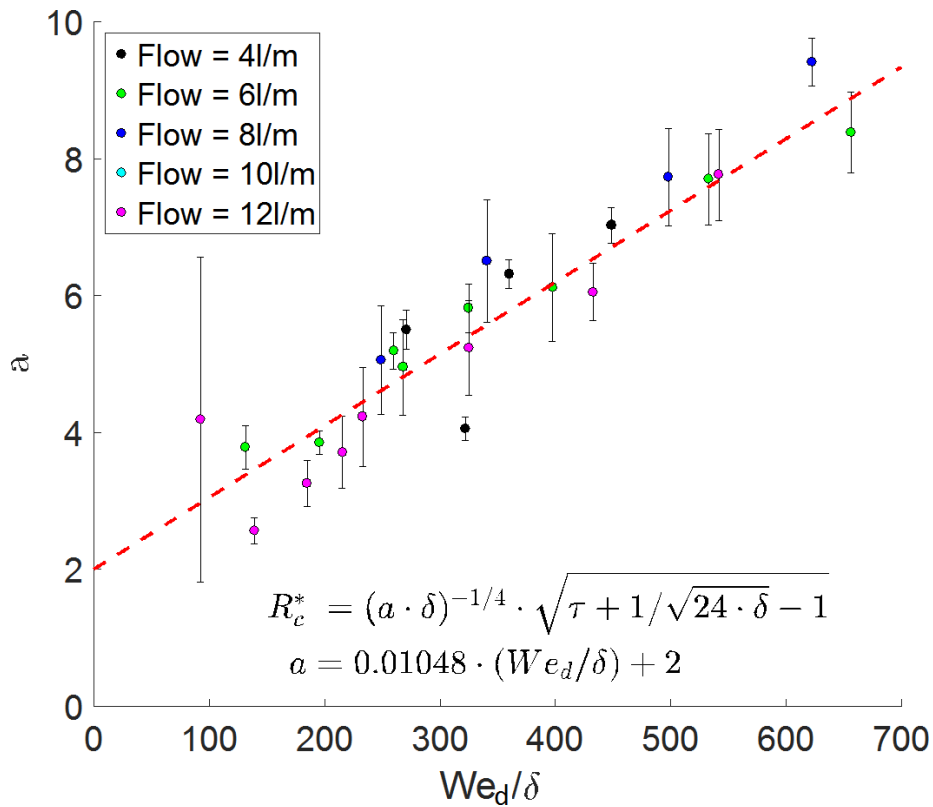


Figure 5.22: Fitting for the a term from Eqn. (5.4) against We_d/δ

$$a = 0.01048 \cdot (We_d/\delta) + 2 \tag{5.5}$$

This improved version of the model can now be compared to the experimen-

tal data, Figs. (5.23, 5.24) show the data for crown width against the original model from Roisman et al. [41], the model from Gao et al. [45], and the newly derived model expressed in Figs. (5.4, 5.5). Whilst this model was empirically derived, the relationship seems physically reasonable, as the impinging droplet properties (in We_d) are obviously related to the crown dynamics, and film thickness has already been shown to effect cavity development.

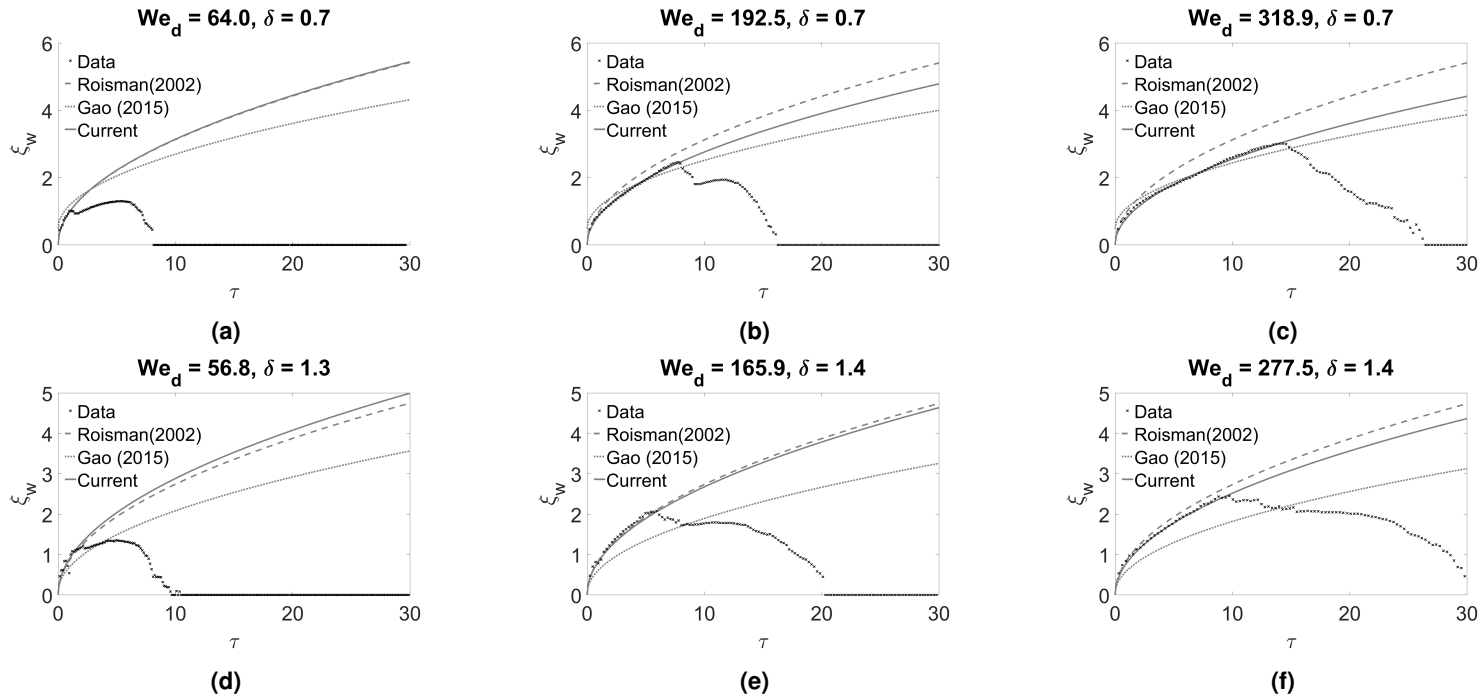


Figure 5.23: 2 mm Impinging droplets against crown model

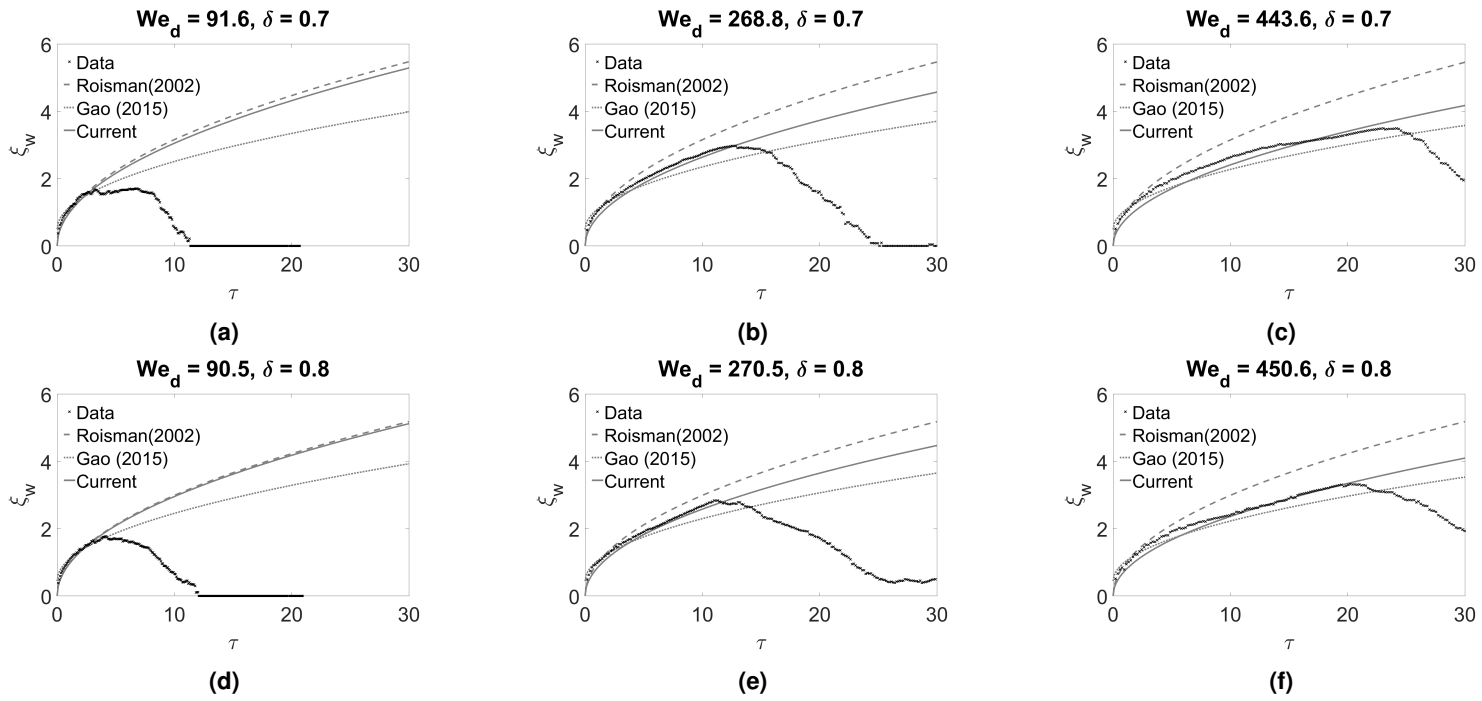


Figure 5.24: 3 mm Impinging droplets against crown model

Examining the data, it is evident that the Roisman model consistently over-predicts the cavity width, which may be due to the film motion inhibiting cavity development in this direction. Furthermore, whilst in some situations the model from Gao et al. [45] gives reasonable results, this generally deteriorates at longer timescales. This is not unforeseen, as the model was specifically derived for values of $\tau < 6$.

The newly derived model gives reasonable fits across the range of conditions, generally intersecting the maximum value. For $We_d < 400$ the model also provides an accurate description of the crown development with time, however at higher values of We_d the model appears to under predict for the earlier stages of crown propagation. Overall, the new model does appear to more-accurately predict the crown development than either of the existing models achieve.

Cavity development on the Upstream and Downstream sides

Alongside the development of cavity width, it is desirable to understand development of the cavity length, and specifically the differences in the upstream and downstream directions. Observation of Figs. (5.3, 5.4) show that the crown extends further in the downstream direction, whilst the upstream side of the crown extends less far, but is noticeably higher for impingements of 10° inclined films. When the crown length and width are considered, it is noted that the crown appears to be larger in the direction parallel to the flow, than when perpendicular to the flow. This is confirmed by measurements of the width and length, a sample of which are shown in Fig. (5.26).

As Figs. (5.3, 5.4) show that the crown propagation is different in the upstream and downstream directions, it was decided to investigate these two properties separately. The extent of the crown in each direction was measured from the cavity centre. Comparison of these distances showed that the crown propagated noticeably faster in the downstream direction than the predicted by the width model. Conversely, the upstream propagation was noticeably slower

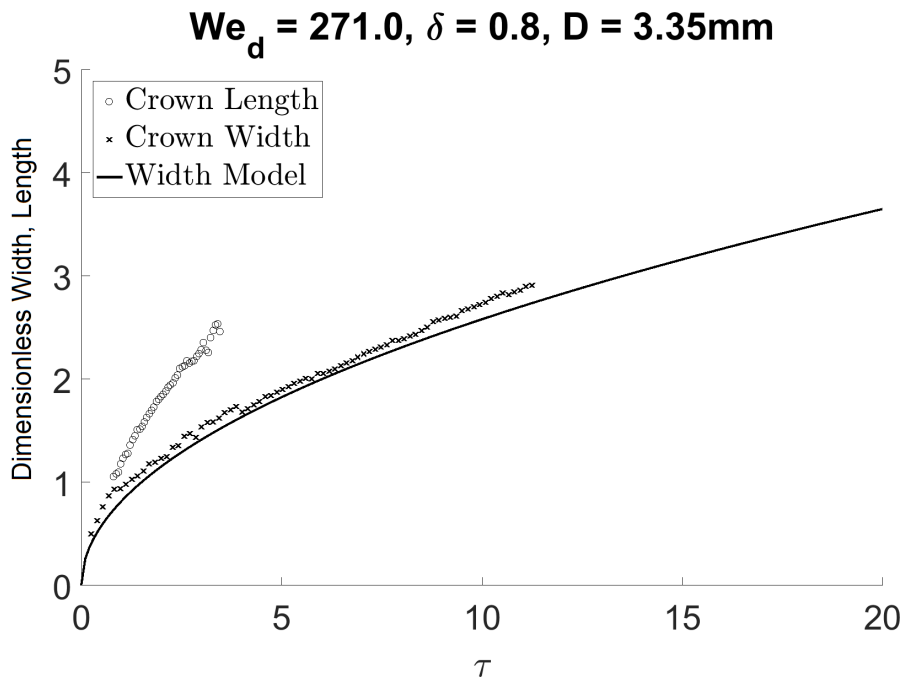


Figure 5.25

Figure 5.26: Development of crown in upstream and downstream directions, showing a typical result

than predicted by the width model.

It was found that by manipulating the velocity form in the dimensionless time-scale τ into the form $\tau_m = t \cdot (V_d - V_f) / D$ allowed a reasonable fit, with the data collapsing on to a single line for both upstream and downstream. Furthermore, across many of the conditions this line was reasonably described by the model previously developed for width, as shown in Figs. (5.27, 5.28).

It should be remarked that there is a deviation observed at lower values of We_d , however this is a result of difficulty detecting the crown from the LIF images due to its small size. At higher values of We_d , there is reasonable agreement with the width model for both 2 mm and 3 mm droplets across a range of film conditions. Furthermore, the experimental work used to derive this timescale is performed on a near-orthogonal set-up, where the channel inclination is 10 °. It is possible that for more severely inclined experiments, this τ_m form may not accurately predict the development of the upstream and

downstream sides of the crown, as for 10° impingement, the velocity component parallel to the film is very small. Hence, more work is required to validate for more steeply inclined conditions.

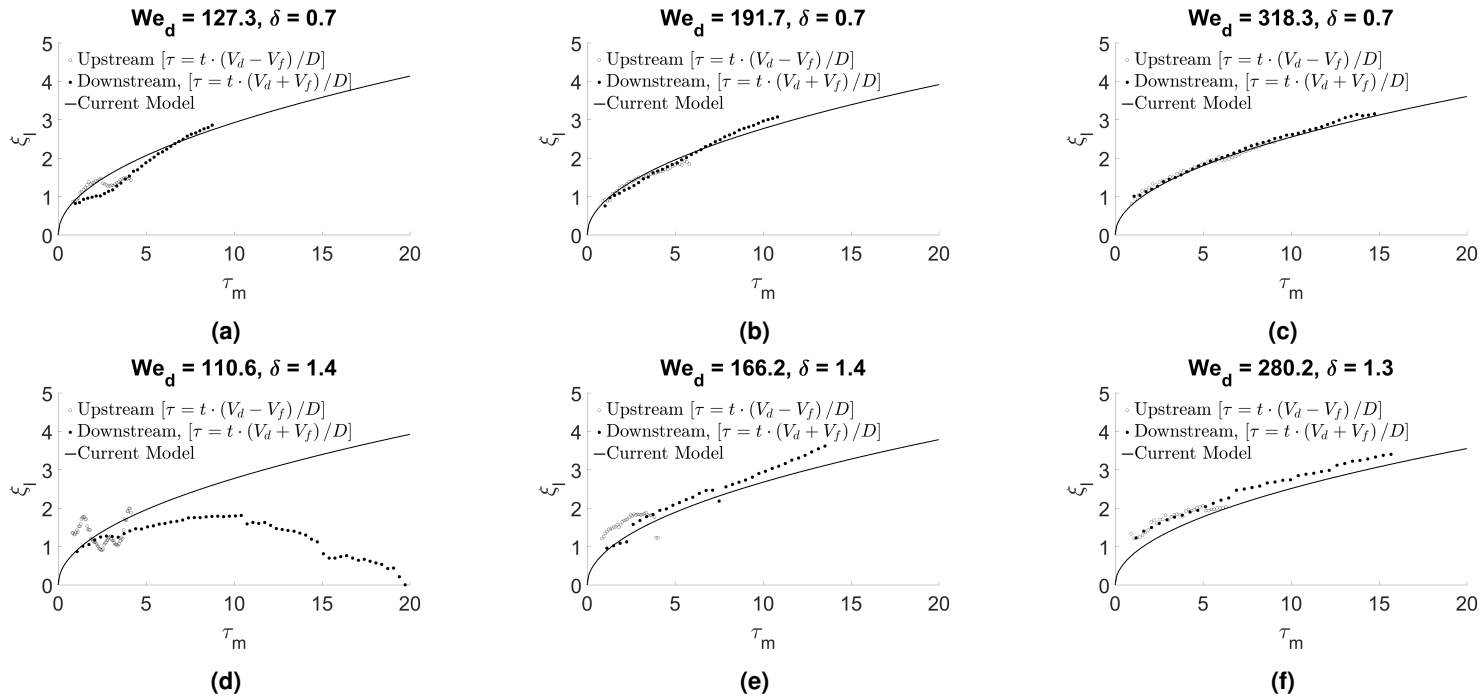


Figure 5.27: Upstream and downstream crown development against width model

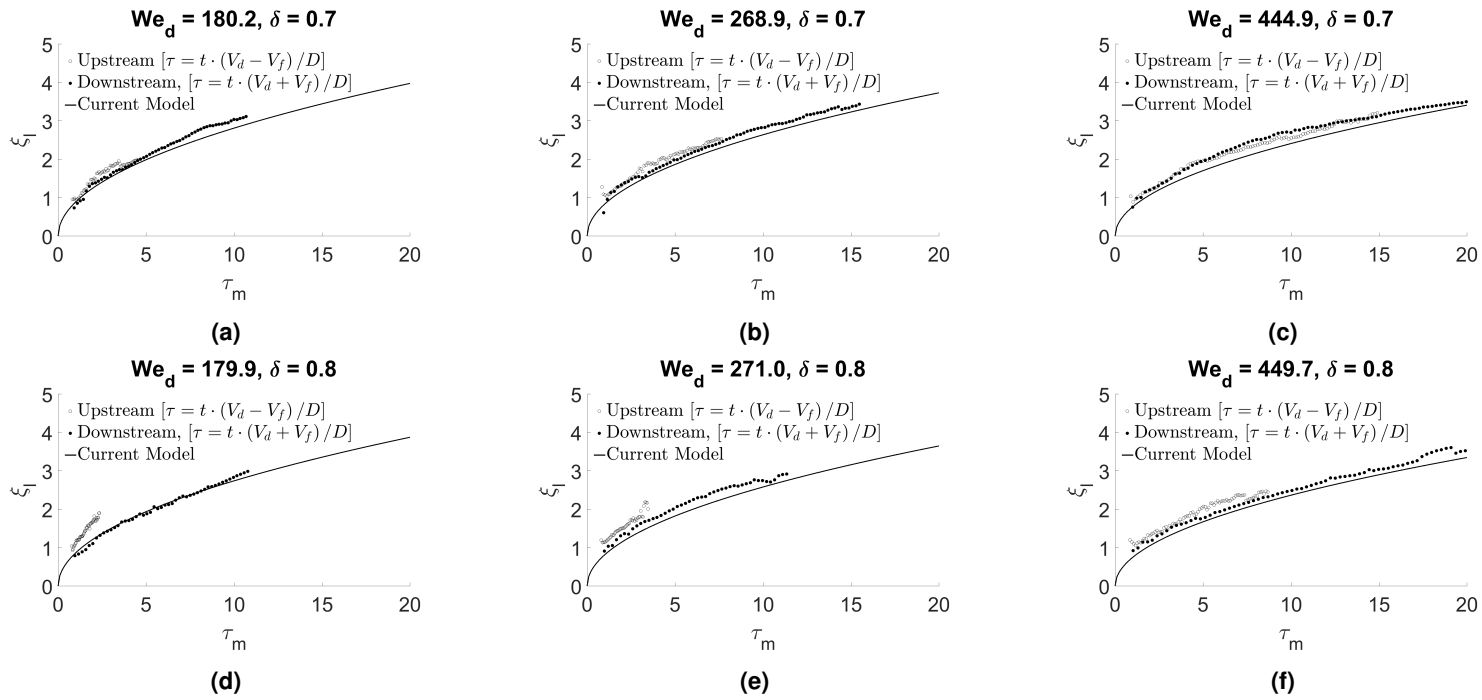


Figure 5.28: Upstream and downstream crown development against width model

5.3.3 Conclusions of crown and cavity development

Within this chapter, a first examination into crown and cavity dynamics has been undertaken using the BB-LIF technique. This work represents a significant contribution to knowledge and understanding of post impingement mass-transfer, with several correlations proposed to facilitate more efficient CFD modelling of bearing chambers.

The cavity width was matched to a model from static film experiments, and a modification proposed to more accurately represent the expansion phase for moving film impingements. Furthermore, spreading of the droplet within the cavity was found to follow spreading behaviours observed for solid-surface impingements at early timescales, and to be driven by cavity expansion at later stages. This has important implications for and mass transfer modelling within the bearing chamber, specifically regarding the size of the interface between the droplet and film.

The crown was found to tend either upstream or downstream, and this could be related to the ratio of film velocity, and the component of droplet velocity in the plane of film flow.

Crown expansion was compared to the analytically derived model from Roisman et al. [41], reasonable agreement was found with the model, however an improvement to it was made by including a dependence on We_d and δ . This significantly increased performance at higher values of We_d . The model from Gao et al. [45] performed better in the early stages of cavity propagation, but tended to severely underestimate the crown expansion at later times.

Alongside the width, the crown extent in the upstream and downstream directions was found to be related to the film speed. By modifying the dimensionless time-scale to include a dependence on film speed in the form $\tau_m = t \cdot (V_d \pm V_f)$, the improved width model could be used to accurately represent to expansion in the upstream and downstream directions. This is a unique factor, which to the authors' best knowledge has not previously been investigated either experimentally or computationally.

Chapter 6

Conclusions

Within this chapter the main conclusions of the work are collated, the contribution to knowledge is stated, and directions for possible future work is discussed.

6.1 Summary of Main Findings

The aim of this work was to create enhanced understanding and produce correlations to aid in the CFD modelling of droplet impingements upon moving films in still air, a steppingstone to allow modelling of full-scale bearing chambers. The primary motivation for this was to enhance design and modelling capability of aero engine bearing chambers, although clearly the work has far wider applicability. Whilst, a wide body of work has led to a sophisticated understanding of these phenomena in cases where the targets are either solid substrates or static films, less work has been undertaken to demonstrate the applicability of these models for moving films. This creates a need to understand how moving film impingements differ from static films, and the effect these differences may have upon the heat and mass transfer after the impingement.

Within the course of this work, the collision of droplets upon moving films has been investigated experimentally. A twofold data acquisition approach was undertaken, combining conventional high-speed imaging of secondary droplet

production, with Laser Induced Fluorescence visualisation of the crater and crown. This allowed comparison and insight into the production of droplets and post-impingement behaviours of the film, compared to existing physical understanding from static film literature.

6.1.1 Secondary Droplet Production

As droplet production has been identified as a key contributor to parasitic losses within the bearing chamber, the programme of work was designed to investigate key parameters of secondary droplet production. The first element of the work utilised high-speed imaging with conventional illumination to investigate the conditions under which secondary droplets are formed, the mechanism by which secondary droplets are created, and the number and characteristics of these droplets.

It was found that moving film impingements demonstrated a high level of comparability to pre-existing static film understanding. In section 4.1, the transition from coalescence to crown formation, and crown formation to crown splashing were considered. These were shown to occur within 3.6% and 2.3% of previously established boundaries of the splashing parameter from Cossali et al. [8]. This work finds the transition between coalescence and crown formation at $K_{C(Vd)} = 725$, compared to 700 for static films. Similarly, the boundary between crown formation and crown splashing was found at $K_{C(Vd)} = 2149$, compared to 2100 for static films. These transition values were determined statistically, using cumulative probability functions to determine the midpoint, an approach which is novel within the field. For oblique impingements on moving films there are several components of velocity which may be used in the calculation of K_C , these were investigated, and it was concluded that to determine the impingement outcome, use of the total droplet velocity gave the most consistent results, with the sharpest transitions within the investigated experimental range.

The effect of film inclination was investigated, and it was found that for im-

pingements within 30° of normal to the film, transition from crown formation to crown splashing remained constant at around $K_{C(Vd)} \approx 2100$. However, when the inclination of the impingement increased to 40° , this splashing threshold rose to $K_{C(Vd)} \approx 2400$. Observations for inclined impingements on static films [19] have noted similar increases in the transition value, but only for more highly inclined impingement angles.

In cases where secondary droplets were produced, the number of secondary droplets resulting from the impingement was compared to a static film correlation in section 4.3.1. It was found that good agreement with the existing works could be achieved based on a correlation from static film literature. This required that the splashing parameter K_C was calculated using the component of droplet velocity normal to the film, (giving $K_{C(Vn)}$) rather than the total droplet velocity ($K_{C(Vd)}$). Once in this form, two distinct regimes were observed. The first was for $K_{C(Vn)} > \approx 4000$ it was found that there was reasonable agreement with existing static film correlations [10], although a slight increase in the number of secondary droplets for given impingement was observed compared to the static film literature. A behaviour which was attributed to the turbulent flow within the film destabilising the crown and producing more droplets ($Re_f = 4100 - 13700$). For the second regime, for $K_{C(Vn)} < \approx 4000$, the static film model shows an over prediction compared to moving film experiments. This behaviour was attributed to droplet production only occurring on one side of the crown, which was investigated, and the $K_{C(Vn)} < \approx 4000$ verified statistically. For this region, a new correlation was created, in the form $N_{sd} \cdot \delta^{-0.3} = 3.47 \times 10^{-7} (K_{C(Vn)} - 1300)^{2.34}$

The secondary sizes and velocities were examined, and this is presented in section 4.3.2. Correlations were formed to relate these to the dimensionless timescale $\tau = tV_d/D$. It was found that as the time after droplet impact τ increased, droplet velocity decreased, and droplet diameter increased. It was found that secondary droplet diameter could be expressed in the form $D_{sd}/D = 7.84 \times 10^{-2} \cdot \tau^{-0.64}$ and that secondary droplet velocity was described

by $V_{sd}/V = (1.26) \cdot \tau^{(-0.5)}$, a form which was derived from models of crown rim velocity. These correlations allow the secondary droplet properties to be approximated based on the impinging droplet properties, and the formation time.

In the course of determining secondary droplet characteristics, it was noted that several distinct mechanisms of formation were routinely observed. These were investigated and quantified in section 4.2, and summarised below. This represents the first comprehensive attempt to categorise the means of droplet production from crown ligaments, combining several pre-existing theories and experimental observations.

- **Prompt:** Caused by Richmyer-Meshkov instability immediately after the droplet hits the film. Droplets produced are very small and fast.
- **Progressive:** Caused by short-wave breakup of the ligaments as the crown expands. Produced droplets with medium sizes and velocities.
- **Recessive:** Caused by the ligament beginning to withdraw, produces very large droplets, with low velocity.
- **Interstitial:** Similar to satellite droplet production for gravity driven jets, where a thin region of fluid separates at both ends, and forms a small droplet.

It is anticipated that with further validation, the ability to relate mechanisms to distinct secondary droplet sizes and velocities will have a variety of potential applications beyond the immediate context. For example, experimental studies into two phase transmissions elements, such as bearings and gearboxes, may be able to relate the observed droplet sizes from distinct formation mechanisms. Furthermore, an enhanced understanding of mist generation could be potentially very useful, as prompt splashing is clearly a significant element in this.

6.1.2 Film Behaviour

Surface roughness has previously been shown to be an important factor in droplet production. Alongside shearing airflows, other causes of film surface disturbances are the crowns and cavities produced by previous impingements within the bearing chamber. Furthermore, there is concern that the crown-like rim of fluid produced after some impingements may be vulnerable to breakup in the highly rotating airflows of a bearing chamber. Use of the BB-LIF technique in chapter 5 allowed crown and cavity development to be compared to existing static film models. Further analysis of high-speed camera data where conventional lighting was used provided insight into the morphology and skew of the crown.

Cavity propagation has been compared to existing static film understanding in section 5.2. This comprised primarily of comparison to the cavity development model from Roisman et al. [42]. This model relates cavity expansion to the dimensionless time as a function of an expansion term (β) and a contraction term (f). Within the literature there has been disagreement about which parameters define the expansion term, with multiple derivations being proposed [42, 43, 44]. Careful analysis of the various forms led the author to propose within the thesis, a new form of $\beta_{Mitchell} = We_d^{-0.132} \cdot \sqrt{\delta}$. This is shown to provide better performance across the range of experimental testing conditions than previous static film derivations, and represents the first usable correlation derived for moving film cavity dynamics.

In Section 5.2.3 droplet spreading within the cavity was investigated, and compared to existing models from static film literature [6]. From this work it was found that in the early timescales, the spreading of droplet material within the cavity showed agreement with the solid-substrate model. Understanding the spreading of droplet material within the early timescales has key implications on the thermal interface, between the droplet and film. Therefore, understanding this phenomenon provides a base for future studies to investigate heat transfer and oil degradation within the bearing chamber.

The asymmetry of the crown for impacts on inclined moving films was investigated, and it was found that the skew direction (whether the upstream or downstream side of the crown was larger) is related to the film velocity, droplet velocity, and the impingement angle. The form of this relationship was explored, and it was found that when $V_d \cdot \sin(\theta)$ was greater than V_f the crown was observed to be larger in the downstream direction. However, when $V_d \cdot \sin(\theta) < V_f$ the upstream side of the crown was enhanced. Prior literature has reported both upstream and downstream skew with regard to moving film impingements. The work undertaken in this thesis is the first investigation to identify which factors determine the skew direction, thereby creating a systematic and statistically derived predictive capability.

Development of the crown was also examined in more detail, firstly by determining the maximum crown size in section 5.3. It was found that for $Re_d < 7000$, the maximum dimensionless crown radius could be described as $\xi_{w(max)} = 3.63 \times 10^{-4} \cdot Re_d + 0.243$ across the range of experimental conditions. Above the critical value of $Re_d < 7000$, the maximum dimensionless crown diameter tends asymptotically towards a $R_{c_{rmax}}^* \rightarrow 3.5$.

The development of the crown with time (nondimensionalised in the form $\tau = tV_d/D$) was compared to an analytically derived model for static films [41], and an early-time model for moving-film impingements [45]. It was found that above a value of $\tau = 5$ the accuracy of the early-time model deteriorated across the majority of conditions. However modification of the static film model, by inclusion of a dependence on droplet Weber number (We_d) and dimensionless film height (δ) in the form $R_{c_w}^* = ([0.01048 \cdot (We_d/\delta) + 2] \cdot \delta)^{-1/4} \cdot \sqrt{\tau + 1/\sqrt{24 \cdot \delta} - 1}$ was found to provide a better approximation of the crown expansion in the direction perpendicular to the flow.

The investigation into crown behaviours was concluded by examining the uneven expansion in the crown upstream and downstream of the impingement site. It was found that by inclusion of the bulk film velocity into the dimensionless time-scale, in the form $\tau_m = [t \cdot (V_d \pm V_f)/D]$, the improved crown width

model could describe the upstream and downstream development with a reasonable level of accuracy. However, it was noted that as these experiments had only been performed for inclinations of 10° , this form has not yet been proven to be applicable for more severely inclined impingements.

6.2 Contributions to Knowledge

The work presented in this thesis makes a significant contribution to understanding of moving film impingements, and the applicability of static film correlations. The formation of new correlations enhances future CFD capability and gives the potential to model bearing chambers with a lower computational cost. It further gives more confidence in results than if only using correlations derived for static films. Examples of this include:

- Proof that some impingement outcome boundaries from static film investigations can be applied to moving films in our experimental range. Including a unique statistical determination of the boundaries and transition regimes.
- Comparison of the number of secondary droplets to existing models for static films; including the identification of a transition region where splashing only occurs on one side of the crown, and relating the secondary droplet velocities to the expansion of the crown's rim.
- Application and modification of models for the crown and cavity development from static film literature to moving film experiments.
- Showing that droplet spread is identical in the early stages to that observed for impingements on solid surfaces, and that mixing is observed between the droplet and film.

These elements allow much greater insight into the mass transfer within an aero-engine bearing chamber. Prior to this work there had been few experimental investigations into moving film impingements, with minimal consensus

on fundamental aspects of impingement dynamics. Not only does this work provide clarity in these areas, but several of the forms of analysis are novel in their application to this field.

This has resulted in several publications, including:

- A preliminary study into droplet impingement presented at the American Society of Mechanical Engineers Annual Engineering Congress and Exposition [50].
- A preliminary BB-LIF study into cavity dynamics at the American Society of Mechanical Engineers Turbomachinery Technical Conference & Exposition [51].
- Contributions to a paper considering static-film impingements in Experiments in Fluids [44].
- Preparation of a manuscript for the International Journal of Multiphase Flow.

6.3 Future Work

The rationale for this thesis was to aid in the complete understanding of droplet dynamics within a bearing chamber. While this thesis has accomplished its defined aim, there are still several aspects of work that require further investigation to fully understand the heat and mass transfer from droplet impingements.

It is evident from the findings in the current work that there are several avenues which require further investigation in order to facilitate full-scale bearing chamber modelling. These include investigation the effect of fluid properties on post-impingement dynamics, specifically relating to the oil within a bearing chamber. Furthermore, a variety of fluid temperatures and atmospheric conditions may be observed within a bearing chamber, as studies by Casterjon-Pita et al. [28] have indicated that current understanding and nondimensionalisations may not fully account for the effect fluid properties on splashing and jetting

behaviours. Further work will be required to fully understand the effect of fluid properties on post-impingement behaviours.

Furthermore, there is a need to understand how shearing airflows and surface waves on the target fluid effect droplet production, and whilst some studies [72, 82, 114] have begun to investigate droplet impingements in shearing airflows for linear testing rigs, few have considered rotational conditions that are more representative of a bearing chamber.

Finally, although the author was involved in a preliminary study [50] of droplet and film heat transfer, it was found that the currently available infra-red camera technology and its limited temporal resolutions were only just able to visualise and quantify the thermal interactions. Therefore, as technology advances there is significant scope for this topic to be revisited.

References

- [1] M. Klingsporn, “Advanced transmission and oil system concepts for modern aero-engines,” *ASME Turbo Expo 2004: Power for Land, Sea, and Air*, 2004. doi:10.1115/gt2004-53578.
- [2] A. Adeniyi, H. Morvan, K. A. Simmons, *et al.*, “A coupled euler-lagrange cfd modelling of droplets-to-film,” *The Aeronautical Journal*, 2017. doi:10.1017/aer.2017.107.
- [3] R. Rioboo, C. Tropea, and M. Marengo, “Outcomes from a drop impact on solid surfaces,” *Atomization and Sprays*, vol. 11, no. 2, 2001. doi:10.1615/atomizspr.v11.i2.40.
- [4] A. Worthington, “A study of splashes. 1908,” *Green, London*, 1908.
- [5] C. Stow and M. Hadfield, “An experimental investigation of fluid flow resulting from the impact of a water drop with an unyielding dry surface,” in *Proceedings of the Royal Society of London A: Mathematical, Physical and Engineering Sciences*, vol. 373, pp. 419–441, The Royal Society, 1981. doi:10.1098/rspa.1981.0002.
- [6] I. V. Roisman, E. Berberović, and C. Tropea, “Inertia dominated drop collisions. i. on the universal flow in the lamella,” *Physics of Fluids (1994-present)*, vol. 21, no. 5, p. 052103, 2009. doi:10.1063/1.3129282.
- [7] J. Fukai, Y. Shiiba, T. Yamamoto, O. Miyatake, D. Poulikakos, C. M. Megaridis, and Z. Zhao, “Wetting effects on the spreading of a liquid droplet colliding with a flat surface: experiment and modeling,” *Physics of fluids*, vol. 7, no. 2, pp. 236–247, 1995. doi:10.1063/1.868622.
- [8] G. E. Cossali, A. Coghe, and M. Marengo, “The impact of a single drop on a wetted solid surface,” *Experiments in Fluids*, vol. 22, no. 6, pp. 463–472, 1997. doi:10.1007/s003480050073.
- [9] R. Rioboo, C. Bauthier, J. Conti, M. Voue, and J. De Coninck, “Experimental investigation of splash and crown formation during single drop

- impact on wetted surfaces,” *Experiments in fluids*, vol. 35, no. 6, pp. 648–652, 2003. doi:10.1007/s00348-003-0719-5.
- [10] T. Okawa, T. Shiraishi, and T. Mori, “Production of secondary drops during the single water drop impact onto a plane water surface,” *Experiments in fluids*, vol. 41, no. 6, pp. 965–974, 2006. doi:10.1007/s00348-006-0214-x.
- [11] X.-S. Wang, X.-D. Zhao, Y. Zhang, X. Cai, R. Gu, and H.-L. Xu, “Experimental study on the interaction of a water drop impacting on hot liquid surfaces,” *Journal of fire sciences*, vol. 27, no. 6, pp. 545–559, 2009. doi:10.1177/0734904109339615.
- [12] E. Castillo Orozco, *Droplet impact on liquid pools: secondary droplets formation from Rayleigh jet break-up and crown splash*. PhD thesis, University of Central Florida Orlando, Florida, 2015.
- [13] O. Jayaratne and B. Mason, “The coalescence and bouncing of water drops at an air/water interface,” *Proceedings of the Royal Society of London. Series A. Mathematical and Physical Sciences*, vol. 280, no. 1383, pp. 545–565, 1964. doi:10.1098/rspa.1964.0161.
- [14] G. Leneweit, R. Koehler, K. Roesner, and G. Schäfer, “Regimes of drop morphology in oblique impact on deep fluids,” *Journal of Fluid Mechanics*, vol. 543, pp. 303–331, 2005. doi:10.1017/s0022112005006476.
- [15] C. Mundo, M. Sommerfeld, and C. Tropea, “Droplet-wall collisions: experimental studies of the deformation and breakup process,” *International journal of multiphase flow*, vol. 21, no. 2, pp. 151–173, 1995. doi:10.1016/0301-9322(94)00069-v.
- [16] J. C. Bird, S. S. Tsai, and H. A. Stone, “Inclined to splash: triggering and inhibiting a splash with tangential velocity,” *New Journal of Physics*, vol. 11, no. 6, p. 063017, 2009. doi:10.1088/1367-2630/11/6/063017.
- [17] S. K. Alghoul, C. N. Eastwick, and D. B. Hann, “Normal droplet impact on horizontal moving films: an investigation of impact behaviour and regimes,” *Experiments in Fluids*, vol. 50, no. 5, pp. 1305–1316, 2011.
- [18] J. R. Castrejón-Pita, B. N. Muñoz-Sánchez, I. M. Hutchings, and A. Castrejón-Pita, “Droplet impact onto moving liquids,” *Journal of Fluid Mechanics*, vol. 809, pp. 716–725, 2016. doi:10.1017/jfm.2016.672.
- [19] T. Okawa, T. Shiraishi, and T. Mori, “Effect of impingement angle on the outcome of single water drop impact onto a plane water surface,” *Experiments in Fluids*, vol. 44, no. 2, pp. 331–339, 2008.

- [20] G. Cossali, G. Brunello, A. Coghe, and M. Marengo, "Impact of a single drop on a liquid film: experimental analysis and comparison with empirical models," in *Italian Congress of Thermofluid Dynamics UIT, Ferrara*, vol. 30, pp. 1–12, 1999.
- [21] M. Trujillo and C. Lee, "Modeling crown formation due to the splashing of a droplet," *Physics of Fluids (1994-present)*, vol. 13, no. 9, pp. 2503–2516, 2001. doi:10.1063/1.1388541.
- [22] R. Krechetnikov and G. M. Homsy, "Crown-forming instability phenomena in the drop splash problem," *Journal of colloid and interface science*, vol. 331, no. 2, pp. 555–559, 2009. doi:10.1016/j.jcis.2008.11.079.
- [23] L. V. Zhang, P. Brunet, J. Eggers, and R. D. Deegan, "Wavelength selection in the crown splash," *Physics of Fluids*, vol. 22, no. 12, p. 122105, 2010. doi:10.1063/1.3526743.
- [24] A. Bisighini, G. E. Cossali, C. Tropea, and I. V. Roisman, "Crater evolution after the impact of a drop onto a semi-infinite liquid target," *Physical Review E*, vol. 82, no. 3, p. 036319, 2010. doi:10.1103/physreve.82.036319.
- [25] E. Berberović, N. P. van Hinsberg, S. Jakirlić, I. V. Roisman, and C. Tropea, "Drop impact onto a liquid layer of finite thickness: Dynamics of the cavity evolution," *Physical Review E*, vol. 79, no. 3, p. 036306, 2009. doi:10.1103/physreve.79.036306.
- [26] A. Mitchell, I. McCarthy, A. V. Cherdantsev, B. N. Hewakandamby, and K. Simmons, "Droplet impact on static films using the bblif technique," *Proc. 13th Triennial International Conference on Liquid Atomization and Spray Systems, Tainan*, 2015.
- [27] M.-J. Thoraval, K. Takehara, T. G. Etoh, S. Popinet, P. Ray, C. Josserand, S. Zaleski, and S. T. Thoroddsen, "von kármán vortex street within an impacting drop," *Physical review letters*, vol. 108, no. 26, p. 264506, 2012. doi:10.1103/physrevlett.108.264506.
- [28] A. Castrejón-Pita, J. Castrejón-Pita, and I. Hutchings, "Experimental observation of von kármán vortices during drop impact," *Physical Review E*, vol. 86, no. 4, p. 045301, 2012. doi:10.1103/physreve.86.045301.
- [29] G. Agbaglah, M.-J. Thoraval, S. T. Thoroddsen, L. V. Zhang, K. Fezzaa, and R. D. Deegan, "Drop impact into a deep pool: vortex shedding and jet formation," *Journal of fluid mechanics*, vol. 764, p. R1, 2015. doi:10.1017/jfm.2014.723.

- [30] L. Zhang, J. Toole, K. Fezzaa, and R. Deegan, "Evolution of the ejecta sheet from the impact of a drop with a deep pool," *Journal of Fluid Mechanics*, vol. 690, pp. 5–15, 2012.
- [31] A. Worthington, "On the forms assumed by drops of liquids falling vertically on a horizontal plate," *Proceedings of the royal society of London*, vol. 25, no. 171-178, pp. 261–272, 1876. doi:10.1098/rspl.1876.0048.
- [32] H. E. Edgerton, E. Jussim, and G. Kayafas, *Stopping time: the photographs of Harold Edgerton*. Abrams, 2000.
- [33] Z. Levin and P. V. Hobbs, "Splashing of water drops on solid and wetted surfaces - hydrodynamics and charge separation," *Philosophical Transactions of the Royal Society of London Series a-Mathematical and Physical Sciences*, vol. 269, no. 1200, p. 555, 1971. doi:10.1098/rsta.1971.0052.
- [34] A. Yarin and D. Weiss, "Impact of drops on solid surfaces: self-similar capillary waves, and splashing as a new type of kinematic discontinuity," *Journal of Fluid Mechanics*, vol. 283, no. 1, pp. 141–173, 1995. doi:10.1017/s0022112095002266.
- [35] S. Alekseenko, V. Antipin, A. Cherdantsev, S. Kharlamov, and D. Markovich, "Investigation of waves interaction in annular gas-liquid flow using high-speed fluorescent visualization technique," *Microgravity Science and Technology*, vol. 20, no. 3-4, pp. 271–275, 2008. doi:10.1007/s12217-008-9028-1.
- [36] A. V. Cherdantsev, D. B. Hann, and B. J. Azzopardi, "Study of gas-sheared liquid film in horizontal rectangular duct using high-speed lif technique: Three-dimensional wavy structure and its relation to liquid entrainment," *International Journal of Multiphase Flow*, vol. 67, pp. 52–64, 2014. doi:10.1016/j.ijmultiphaseflow.2014.08.003.
- [37] K. Vernon, *A photographic probe for wet steam*. PhD thesis, University of Nottingham, 2014.
- [38] Mathworks, "Correcting nonuniform illumination." <http://www.mathworks.co.uk/help/images/examples/correcting-nonuniform-illumination.html>, Sept. 2013.
- [39] Mathworks, "Find circles using circular hough transform," September 2012.
- [40] M. Minsky, "Microscopy apparatus," Dec. 1961. US Patent 3,013,467.

- [41] I. Roisman and C. Tropea, "Impact of a drop onto a wetted wall: description of crown formation and propagation," *Journal of Fluid Mechanics*, vol. 472, pp. 373–397, 2002. doi:10.1017/s0022112002002434.
- [42] I. V. Roisman, N. P. van Hinsberg, and C. Tropea, "Propagation of a kinematic instability in a liquid layer: Capillary and gravity effects," *Physical Review E*, vol. 77, no. 4, p. 046305, 2008. doi:10.1103/physreve.77.046305.
- [43] N. van Hinsberg, *Investigation of drop and spray impingement on a thin liquid layer accounting for the wall film topology*. PhD thesis, Technische Universität, 2010.
- [44] D. B. Hann, A. V. Cherdantsev, A. Mitchell, I. McCarthy, B. N. Hewakandamby, and K. Simmons, "A study of droplet impact on static films using the bb-lif technique," *Experiments in Fluids*, vol. 57, no. 4, pp. 1–12, 2016. doi:10.1007/s00348-016-2132-x.
- [45] X. Gao and R. Li, "Impact of a single drop on a flowing liquid film," *Physical Review E*, vol. 92, no. 5, p. 053005, 2015. doi:10.1103/physreve.92.053005.
- [46] Q. Huang and H. Zhang, "A study of different fluid droplets impacting on a liquid film," *Petroleum science*, vol. 5, no. 1, pp. 62–66, 2008. doi:10.1007/s12182-008-0010-8.
- [47] office of national statistics, "Uk perspectives 2016: How we travel." <http://visual.ons.gov.uk/uk-perspectives-2016-how-we-travel/>, May 2016.
- [48] J. L. Hee, R. Santhosh, K. Simmons, G. Johnson, D. Hann, and M. Walsh, "Oil film thickness measurements on surfaces close to an aero-engine ball bearing using optical techniques," in *ASME Turbo Expo 2017: Turbomachinery Technical Conference and Exposition*, pp. V07AT34A017–V07AT34A017, American Society of Mechanical Engineers, 2017. doi:10.1115/gt2017-63813.
- [49] D. Peduto, *Oil Droplet Impact Dynamics in Aero-Engine Bearing Chambers-Correlations derived from Direct Numerical Simulations*. Logos Verlag Berlin GmbH, 2015.
- [50] A. J. Mitchell, K. Simmons, and D. Hann, "Experimental investigation into droplet impingement upon moving films using high speed video and thermal imaging," in *ASME 2015 International Mechanical Engineering*

- Congress and Exposition*, pp. V001T01A038–V001T01A038, American Society of Mechanical Engineers, 2015. doi:10.1115/imece2015-51677.
- [51] A. J. Mitchell, D. Hann, and K. Simmons, “Experimental investigation into crater morphology for droplets impinging on a moving film,” in *ASME Turbo Expo 2017: Turbomachinery Technical Conference and Exposition*, pp. V02DT48A006–V02DT48A006, American Society of Mechanical Engineers, 2017. doi:10.1115/gt2017-63443.
- [52] W. Macklin and G. Payne, “A theoretical study of the ice accretion process,” *Quarterly Journal of the Royal Meteorological Society*, vol. 93, no. 396, pp. 195–213, 1967. doi:10.1002/qj.49709339606.
- [53] I. V. Roisman, K. Horvat, and C. Tropea, “Spray impact: rim transverse instability initiating fingering and splash, and description of a secondary spray,” *Physics of Fluids*, vol. 18, no. 10, p. 102104, 2006. doi:10.1063/1.2364187.
- [54] W. Macklin and G. Metaxas, “Splashing of drops on liquid layers,” *Journal of applied physics*, vol. 47, no. 9, pp. 3963–3970, 2008.
- [55] A. Frohn and N. Roth, *Dynamics of droplets*. Springer, 2000. doi:10.1007/978-3-662-04040-9.
- [56] S. Manzello and J. Yang, “An experimental study of a water droplet impinging on a liquid surface,” *Experiments in fluids*, vol. 32, no. 5, pp. 580–589, 2002. doi:10.1007/s00348-001-0401-8.
- [57] S. Alghoul, *Experimental investigation of single droplet impact onto moving films / Samah Alghoul*. PhD thesis, University of Nottingham, Mechanical, Materials Manufacturing Engineering., (2011).
- [58] M. Marengo and C. Tropea, “Aufprall von tropfen auf flüssigkeitsfilme,” *DFG, Berlin, Zwischenbericht zum Forschungsvorhaben*, vol. 194, pp. 10–18, 1999.
- [59] B. L. Scheller and D. W. Bousfield, “Newtonian drop impact with a solid surface,” *AIChE Journal*, vol. 41, no. 6, pp. 1357–1367, 1995. doi:10.1002/aic.690410602.
- [60] A. Coghe, G. Cossali, and M. Marengo, “A first study about single droplet impingement on thin liquid film in a low laplace number range,” *ICLASS-95, Nürnberg*, pp. 285–293, 1995.

- [61] R. Wal, G. Berger, and S. Mozes, "The splash/non-splash boundary upon a dry surface and thin fluid film," *Experiments in Fluids*, vol. 40, no. 1, pp. 53–59, 2006. doi:10.1007/s00348-005-0045-1.
- [62] C. Tropea and M. Marengo, "The impact of drops on walls and films," *Multiphase Science and Technology*, vol. 11, no. 1, 1999. doi:10.1615/multsciotechn.v11.i1.20.
- [63] W. Macklin and P. Hobbs, "Subsurface phenomena and the splashing of drops on shallow liquids," *Science*, vol. 166, no. 3901, pp. 107–108, 1969. doi:10.1126/science.166.3901.107.
- [64] R. L. Vander Wal, G. M. Berger, and S. D. Mozes, "Droplets splashing upon films of the same fluid of various depths," *Experiments in fluids*, vol. 40, no. 1, pp. 33–52, 2006.
- [65] A.-B. Wang, C.-H. Lin, and C.-C. Chen, "The critical temperature of dry impact for tiny droplet impinging on a heated surface," *Physics of Fluids*, vol. 12, no. 6, pp. 1622–1625, 2000. doi:10.1063/1.870413.
- [66] S. L. Manzello, J. C. Yang, and T. G. Cleary, "On the interaction of a liquid droplet with a pool of hot cooking oil," *Fire safety journal*, vol. 38, no. 7, pp. 651–659, 2003. doi:10.1016/s0379-7112(03)00048-1.
- [67] S. L. Manzello and J. C. Yang, "The influence of liquid pool temperature on the critical impact weber number for splashing," *Physics of Fluids (1994-present)*, vol. 15, no. 1, pp. 257–260, 2003. doi:10.1063/1.1526696.
- [68] S. L. Manzello and J. C. Yang, "An experimental investigation of water droplet impingement on a heated wax surface," *International journal of heat and mass transfer*, vol. 47, no. 8, pp. 1701–1709, 2004. doi:10.1016/j.ijheatmasstransfer.2003.10.020.
- [69] L. Fang and G. Chen, "The experimental and theoretical study of oil droplet spreading behaviors after oblique collision," in *Cybernetics, Robotics and Control (CRC), International Conference on*, pp. 42–47, IEEE, 2016. doi:10.1109/crc.2016.019.
- [70] J. Hao and S. I. Green, "Splash threshold of a droplet impacting a moving substrate," *Physics of Fluids*, vol. 29, no. 1, p. 012103, 2017. doi:10.1063/1.4972976.
- [71] W. Samenfink, A. Elsäßer, K. Dullenkopf, and S. Wittig, "Droplet interaction with shear-driven liquid films: analysis of deposition and secondary

- droplet characteristics,” *International Journal of Heat and Fluid Flow*, vol. 20, no. 5, pp. 462–469, 1999. doi:10.1016/s0142-727x(99)00035-1.
- [72] S. Alghoul, C. Eastwick, and D. Hann, “Droplet impact on shear-driven liquid films,” *Atomization and Sprays*, vol. 21, no. 10, pp. 833–846, 2011. doi:10.1615/atomizspr.2012004124.
- [73] G. Cossali, M. Marengo, A. Coghe, and S. Zhdanov, “The role of time in single drop splash on thin film,” *Experiments in Fluids*, vol. 36, no. 6, pp. 888–900, 2004. doi:10.1007/s00348-003-0772-0.
- [74] J. Zhang, X. Lu, W. Huang, and Y. Han, “Reversible superhydrophobicity to superhydrophilicity transition by extending and unloading an elastic polyamide film,” *Macromolecular rapid communications*, vol. 26, no. 6, pp. 477–480, 2005. doi:10.1002/marc.200400512.
- [75] D. Peduto, A. A. Hashmi, K. Dullenkopf, H.-J. Bauer, and H. Morvan, “Modelling of an aero-engine bearing chamber using enhanced cfd technique,” in *ASME 2011 Turbo Expo: Turbine Technical Conference and Exposition*, pp. 809–819, American Society of Mechanical Engineers, 2011. doi:10.1115/gt2011-45635.
- [76] A. Yarin and D. Weiss, “Impact of drops on solid surfaces: self-similar capillary waves, and splashing as a new type of kinematic discontinuity,” *Journal of Fluid Mechanics*, vol. 283, pp. 141–173, 1995. doi:10.1017/s0022112095002266.
- [77] D. A. Weiss and A. L. Yarin, “Single drop impact onto liquid films: neck distortion, jetting, tiny bubble entrainment, and crown formation,” *Journal of Fluid Mechanics*, vol. 385, pp. 229–254, 1999. doi:10.1017/s002211209800411x.
- [78] N. Bremond and E. Villermaux, “Atomization by jet impact,” *Journal of Fluid Mechanics*, vol. 549, pp. 273–306, 2006. doi:10.1017/s0022112005007962.
- [79] O. G. Engel, “Initial pressure, initial flow velocity, and the time dependence of crater depth in fluid impacts,” *Journal of applied physics*, vol. 38, no. 10, pp. 3935–3940, 1967. doi:10.1063/1.1709044.
- [80] D. Sivakumar and C. Tropea, “Splashing impact of a spray onto a liquid film,” *Physics of fluids*, vol. 14, no. 12, pp. L85–L88, 2002. doi:10.1063/1.1521418.

- [81] X. Yang, L. Dai, and S.-C. Kong, "Simulation of liquid drop impact on dry and wet surfaces using sph method," *Proceedings of the Combustion Institute*, 2016. doi:10.1016/j.proci.2016.07.031.
- [82] A. V. Cherdantsev, D. B. Hann, B. N. Hewakandamby, and B. J. Az-zopardi, "Study of the impacts of droplets deposited from the gas core onto a gas-sheared liquid film," *International Journal of Multiphase Flow*, vol. 88, pp. 69–86, 2017. doi:10.1016/j.ijmultiphaseflow.2016.09.015.
- [83] G. F. Hewitt and B. Nicholls, "Film thickness measurement in annular two-phase flow using a fluorescence spectrometer technique. part ii. studies of the shape of disturbance waves.," tech. rep., Atomic Energy Research Establishment, Harwell (England), 1969.
- [84] M. Hoffmann, M. Schlüter, and N. Rübiger, "Experimental investigation of liquid–liquid mixing in t-shaped micro-mixers using μ -lif and μ -piv," *Chemical Engineering Science*, vol. 61, no. 9, pp. 2968–2976, 2006.
- [85] S. Alekseenko, V. Antipin, A. Cherdantsev, S. Kharlamov, and D. Markovich, "Two-wave structure of liquid film and wave interrelation in annular gas-liquid flow with and without entrainment," *Physics of Fluids (1994-present)*, vol. 21, no. 6, p. 061701, 2009. doi:10.1063/1.3151999.
- [86] R. Field, "Internship report," 2014.
- [87] S. Herbert, S. Fischer, T. Gambaryan-Roisman, and P. Stephan, "Local heat transfer and phase change phenomena during single drop impingement on a hot surface," *International Journal of Heat and Mass Transfer*, vol. 61, pp. 605–614, 2013. doi:10.1016/j.ijheatmasstransfer.2013.01.081.
- [88] C. Pedersen, "An experimental study of the dynamic behavior and heat transfer characteristics of water droplets impinging upon a heated surface," *International Journal of Heat and Mass Transfer*, vol. 13, no. 2, pp. 369IN3373–372IN5381, 1970. doi:10.1016/0017-9310(70)90113-4.
- [89] J. Schneider and C. Hendricks, "Source of uniform sized liquid droplets," *Review of Scientific Instruments*, vol. 35, p. 1349, 1964. doi:10.1063/1.1718742.
- [90] H. P. Le, "Progress and trends in ink-jet printing technology," *Journal of Imaging Science and Technology*, vol. 42, no. 1, pp. 49–62, 1998.
- [91] Mathworks, "Detecting a cell using image segmentation." <http://www.mathworks.co.uk/help/images/examples/detecting-a-cell-using-image-segmentation.html>, Sept. 2013.

- [92] Mathworks, “Deblurring images using a wiener filter.” <http://www.mathworks.co.uk/help/images/examples/deblurring-images-using-a-wiener-filter.html>, Sept. 2013.
- [93] S. D. S. University, “Deblurring with a wiener filter.” <http://www-rohan.sdsu.edu/doc/matlab/toolbox/images/deblurr6.html>, June 2002.
- [94] H. Yuen, J. Princen, J. Illingworth, and J. Kittler, “Comparative study of hough transform methods for circle finding,” *Image and vision computing*, vol. 8, no. 1, pp. 71–77, 1990. doi:10.1016/0262-8856(90)90059-e.
- [95] D. Hess, C. Brücker, J. Kitzhofer, and T. Nonn, “Single-view volumetric piv using high-resolution scanning and least squares matching,” in *9th Int. Symp. Particle Image Velocimetry–PIV*, vol. 11, pp. 21–23, 2011.
- [96] R. C. Ltd, “Product details: Liquid flow indicator,” March 2018.
- [97] Keyence, “Transparent object thickness measurement,” Sept. 2017.
- [98] E. P. DeGarmo, J. T. Black, R. A. Kohser, and B. E. Klamecki, *Materials and process in manufacturing*. Prentice Hall, 1997.
- [99] S. Wittig, A. Glahn, and J. Himmelsbach, “Influence of high rotational speeds on heat transfer and oil film thickness in aero engine bearing chambers,” in *ASME 1993 International Gas Turbine and Aeroengine Congress and Exposition*, pp. V03AT15A060–V03AT15A060, American Society of Mechanical Engineers, 1993. doi:10.1115/93-gt-209.
- [100] S. a. Kline and F. McClintock, “Describing uncertainties in single-sample experiments,” *ASME Mech Eng*, vol. 75, pp. 3–8, 1953.
- [101] M. Dunn and A. Masri, “A comprehensive model for the quantification of linear and nonlinear regime laser-induced fluorescence of oh under $A2\Sigma^+ \leftarrow X2\Pi(1, 0)$ excitation,” *Applied Physics B*, vol. 101, no. 1-2, pp. 445–463, 2010. doi:10.1007/s00340-010-4129-0.
- [102] E. Brainerd, “X-ray reconstruction of moving morphology (xromm).” <https://wiki.brown.edu/confluence/pages/viewpage.action?pageId=71892786>, Oct. 2008.
- [103] I. Vision, “Idt camera sdk.” <https://idtvision.com/products/software/motion-studio/>, May 2017.
- [104] N. C. S. University, “Falling mass and euler methods.” <http://www4.ncsu.edu/eos/users/w/white/www/white/ma302/less208.pdf>, Sept. 2007 3.

- [105] B. Shoushtarian, “A practical approach to real-time dynamic background generation based on a temporal median filter,” *Journal of Sciences, Islamic Republic of Iran*, vol. 14, no. 4, pp. 351–362, 2003.
- [106] R. Cucchiara, C. Grana, M. Piccardi, and A. Prati, “Detecting moving objects, ghosts, and shadows in video streams,” *IEEE transactions on pattern analysis and machine intelligence*, vol. 25, no. 10, pp. 1337–1342, 2003. doi:10.1109/tpami.2003.1233909.
- [107] G. Lagubeau, M. A. Fontelos, C. Josserand, A. Maurel, V. Pagneux, and P. Petitjeans, “Spreading dynamics of drop impacts,” *Journal of Fluid Mechanics*, vol. 713, pp. 50–60, 2012. doi:10.1017/jfm.2012.431.
- [108] K. Haller, Y. Ventikos, D. Poulikakos, and P. Monkewitz, “Computational study of high-speed liquid droplet impact,” *Journal of Applied Physics*, vol. 92, no. 5, pp. 2821–2828, 2002. doi:10.1063/1.1495533.
- [109] R. D. Deegan, P. Brunet, and J. Eggers, “Rayleigh-plateau instability causes the crown splash,” *arXiv preprint arXiv:0806.3050*, 2008.
- [110] J. Shinjo and A. Umemura, “Simulation of liquid jet primary breakup: dynamics of ligament and droplet formation,” *International Journal of Multiphase Flow*, vol. 36, no. 7, pp. 513–532, 2010. doi:10.1016/j.ijmultiphaseflow.2010.03.008.
- [111] E. Castillo-Orozco, A. Davanlou, P. K. Choudhury, and R. Kumar, “Droplet impact on deep liquid pools: Rayleigh jet to formation of secondary droplets,” *Physical Review E*, vol. 92, no. 5, p. 053022, 2015. doi:10.1103/physreve.92.053022.
- [112] N. N. Mansour and T. S. Lundgren, “Satellite formation in capillary jet breakup,” *Physics of Fluids A: Fluid Dynamics (1989-1993)*, vol. 2, no. 7, pp. 1141–1144, 1990. doi:10.1063/1.857613.
- [113] W. Samenfink, A. Elsäßer, K. Dullenkopf, and S. Wittig, “Droplet interaction with shear-driven liquid films: analysis of deposition and secondary droplet characteristics,” *International journal of heat and fluid flow*, vol. 20, no. 5, pp. 462–469, 1999. doi:10.1016/s0142-727x(99)00035-1.
- [114] I. T. Adebayo and O. K. Matar, “Droplet impact on flowing liquid films with inlet forcing: the splashing regime,” *Soft Matter*, 2017. doi:10.1039/c7sm01468f.

- [115] Y. Hardalupas, A. Taylor, and J. H. Wilkins, "Experimental investigation of sub-millimetre droplet impingement onto spherical surfaces," *International Journal of Heat and Fluid Flow*, vol. 20, no. 5, pp. 477–485, 1999. doi:10.1016/s0142-727x(99)00045-4.
- [116] S. Chandra and C. Avedisian, "Observations of droplet impingement on a ceramic porous surface," *International journal of heat and mass transfer*, vol. 35, no. 10, pp. 2377–2388, 1992. doi:10.1016/0017-9310(92)90080-c.
- [117] R. L. Vander Wal, G. M. Berger, and S. D. Mozes, "The combined influence of a rough surface and thin fluid film upon the splashing threshold and splash dynamics of a droplet impacting onto them," *Experiments in fluids*, vol. 40, no. 1, pp. 23–32, 2006.
- [118] M. Farrall, K. Simmons, S. Hibberd, and P. Gorse, "A numerical model for oil film flow in an aeroengine bearing chamber and comparison to experimental data," *Journal of Engineering for Gas Turbines and Power*, vol. 128, no. 1, pp. 111–117, 2006. doi:10.1115/1.1924719.
- [119] Z. Che, A. Deygas, and O. K. Matar, "Impact of droplets on inclined flowing liquid films," *Physical Review E*, vol. 92, no. 2, pp. 023–032, 2015. doi:10.1103/physreve.92.023032.